Influence of extrusion parameters on microstructure development and mechanical properties in wrought magnesium alloys AZ80 and ZK60

Dissertation
zur Erlangung des Grades eines
Doktor-Ingenieurs

vorgelegt von
Muhammad Shahzad, M.Sc.
aus Lahore, Pakistan

genehmigt von
der Fakultät für Natur- und Materialwissenschaften
der Technischen Universität Clausthal

Tag der mündlichen Prüfung
30.04.2010

Vorsitzender der Promotionkommission	Prof. Dr. A. Wolter
Hauptberichterstatter	Prof. Dr. L. Wagner
Berichterstatter	Prof. Dr. M. Janecek

Eidesstattliche Erklärungen

Hiermit erkläre ich an Eides Statt, dass ich die bei der Fakultät für Material- und Naturwissenschaften der Technischen Universität Clausthal eingereichte Dissertation selbständig und ohne unerlaubte Hilfe verfasst und die benutzten Hilfsmittel vollständig angegeben habe.

Hiermit erkläre ich an Eides Statt, dass die eingereichte Dissertation weder in Teilen noch in Ihrer Gesamtheit einer anderen Hochschule zur Begutachtung vorliegt oder vorgelegen hat und dass ich bisher noch keinen Promotionsversuch unternommen habe.

Muhammad Shahzad

Zusammenfassung

Die DC-cast Magnesiumknetlegierungen AZ80 und ZK60 wurden durch direktes Strangpressen und Rundkneten mit unterschiedlichen Umformgraden in einem Temperaturbereich von 175-350 °C plastisch verformt. Die Mikrostrukturentwicklung wurde licht- wie elektronenmikroskopisch nachgewiesen. Die kristallografische Textur wurde durch Röntgendiffraktometrie untersucht. Dabei wurde festgestellt, dass die Mg-Legierung ZK60 einen höheren Grad an dynamischer Rekristallisation aufweist, wie AZ80. Die dynamische Rekristallisation von ZK60 zeigte sich durch eine relativ fein rekristallisierte Korngröße und einer abgeschwächten kristallografischen Textur. Dieses Verhalten wird auf die Zr-reichen Kerne in ZK60 zurückgeführt und zeigt ein geringes DRX- Signal nach der Umformung. Diese Kerne bilden sich bei der Zr-Zugabe aus, um so die Korngröße während des Gießprozess zu minimieren. Die vor der Umformung durchgeführte Homogenisierungsglühung verbessert das DRX- Verhalten und resultiert in einem höheren Grand an Rekristallisation. Die mechanischen Eigenschaften der umgeformten Legierungen wurden unter Zug- wie auch Druckbelastung bestimmt. Bei AZ80 werden keine Auswirkungen durch Anwendung verschiedener Umformgrade auf die Mikrostrukturentwicklung und dem Strength Differential Effekt (SDE) verzeichnet. Bei ZK60 zeigt sich allerdings sehr deutlich ein Effekt des Umformgrades auf die Mikrostrukturentwicklung. Eine relativ hohe Anzahl an großen Körnern bei geringem Umformgrad bedeutet einen wesentlich geringeren SDE. Obwohl eine Umformung vor der Homogenisierungsglühung bei 400 °C in beiden Legierungen AZ80 bzw. ZK60 den Rekristallisationsgrad erhöht und die kristallografische Textur abschwächt, zeigt sich, dass bei ZK60 nur die Dehngrenze leicht abnimmt. Grund hierfür ist die Tatsache, dass es hierbei (ZK60) zu einer vollständigen Auflösung der eutektischen Phase kommt. Der deutliche Kornfeinungseffekt nach dem Strangpressen erhöht deutlich die Festigkeit beider Legierungen bei Raumtemperatur; allerdings zeigt der Gusszustand eine höhere Festigkeit bei verschiedenen Temperaturen (T $>$ 200 °C). Der stranggepresste Zustand zeigt aufgrund seiner Feinkörnigkeit Superplastizität bei Temperaturen höher als 250 °C. Die ZK60 Legierung weist eine höhere Ermüdungsfestigkeit als AZ80 auf.

Abstract

The as-received wrought magnesium alloys AZ80 and ZK60 have been plastically deformed by direct extrusion and rotary swaging to various degrees of deformation in a temperature range 175-350 °C. The evolution of microstructure has been studied using optical and electron microscopy. The crystallographic texture has been studied using X-ray diffraction. In comparison to ZK60 alloy, AZ80 alloy shows a higher degree of dynamic recrystallization, a relatively finer recrystallized grain size and a weaker crystallographic texture. This behavior stems from the Zr-rich cores present in ZK60 alloys and show poor DRX response during deformation. These cores are formed when Zr addition is made to refine the grain size during the casting process. The pre-deformation homogenization treatment improves the DRX behavior and results in higher degree of recrystallization. The mechanical properties of the deformed alloys have been determined under tensile and compressive loadings. In AZ80 alloy, the variations in the degree of deformation in a range φ = 2-3 do not affect the microstructure evolution and the strength differential effect (SDE), which is the difference in tensile and compressive yield stress. On the other hand, the microstructure evolution in ZK60 alloys is significantly affected by the degree of deformation in the same range. A relatively higher proportion of coarse grain at lower degree of deformation results in a three times higher SDE ($\sim$100 MPa). Although, the pre-deformation homogenization treatment at 400 °C increases the degree of recrystallization and weakens the texture in both alloys, the yield stress is significantly lowered only in the case of ZK60 alloys, because of the total dissolution of eutectic compound compared to only a partial dissolution in AZ80 alloy. The significant grain refinement after extruding significantly increases the strength at room temperature; however as-cast alloys show higher strength at elevated temperatures (T $>$ 200 °C). The as-extruded alloys, because of their fine grain sizes exhibit superplasticity at temperature higher than 250°C. The ZK60 alloy, by virtue of its higher strength exhibits higher endurance limit than the one observed in AZ80 alloy. In addition, the rotating beam fatigue tests show that fatigue life is not affected by the compressive yield stress and increases linearly with an increase in tensile yield stress.

Acknowledgements

I am deeply grateful to my thesis supervisor, Prof. Dr. Lothar Wagner, who was abundantly helpful and offered immense support and guidance. I am also thankful to the co-referent Prof. Dr. Milos Janecek for his critical comments and suggestions covering many areas of my research work. Special thanks are due to Dr. Sangbong Yi for many sessions of fruitful discussions on experimental results, especially related to the crystallographic texture.

I would also like to thank all the group members for all their support and help in both curricular and co-curricular matters, and making my stay at IWW a memorable experience. I would specially like to thank my colleagues Emad Kamal, M.Sc., for his help in performing X-ray texture measurements and Khaung Zay, M.E., for his help in performing rotary swaging treatment and push-pull fatigue testing.

I am also thankful to all the technical staff at IWW for their support, particularly Mr. Uwe Hanke for performing the extrusion process, and Mr. Dieter Brinkmann for providing excellent working environment in the metallography laboratory.

I am particularly thankful to the Higher Education Commission, Government of Pakistan, for sponsoring my stay at IWW, TU Clausthal, and DAAD for sponsoring the German language course and providing excellent administrative services.

Last but not the least, I wish to express my deepest gratitude to my beloved parents and siblings for their consistent motivation and encouragement during my entire student life.

Contents

List of Figures

List of Tables

1 Introduction

Magnesium is one of the lightest structural metals; replacing aluminum and steel with magnesium in equal volumes would result in a weight saving of around 33% and 77%, respectively. The remarkable weight saving ability of magnesium and its alloys offers great potential for manufacturing portable and automotive components. Although, this potential was realized much earlier and the use of Mg alloys in manufacturing automobile components started as early as in 1930's; but, the production and applications of Mg alloys have not grown much. One of the main reasons for this is the limited use of wrought magnesium alloys. The potential of cast magnesium alloys has been realized to a significant extent. Because of their good casting properties, cast magnesium alloys have successfully replaced aluminum alloys and steels in many applications, such as engine blocks and gear box housings in automobiles. However due to their closed packed hexagonal lattice and therefore limited active slip systems, wrought alloys are lacking behind and have not been able to replace Al. In last few years, significant advances have been made in the field of wrought magnesium alloys, which have revived the interest in them. At elevated temperature, additional slip systems are activated and the formability of Mg alloys is improved. The wrought Mg alloys exhibit much higher strength coupled with high ductility than the as-cast alloys, because of much finer grain sizes after recrystallization.

Cast Mg alloys suffer from inhomogeneous coarse grain sizes. In case of high pressure die casting, the grain sizes are generally fine because of the significantly high cooling rates. But during other casting processes which are used for wrought alloys, such as sand casting, permanent mold casting and direct chill (DC) casting, the cooling rates are relatively low and a grain refining agent is required to get a uniform fine microstructure [1]. Al alloying is one of the most widely used methods of grain refinement in Mg alloys. In addition, Al contributes in strength by solid solution strengthening and precipitate hardening. The strength of Mg-Al alloys can be further increased by addition of third alloying element e.g. Zn and Mn. However, this technique can not be used when the alloy contains elements which form stable compounds with Al and thereby take Al out of solid solution. In such cases, other inoculants or alloying elements are added. Another important method of grain refinement in Mg alloys is the Zr addition. The refining action of Zr is attributed to the peritectic reaction between Zr and Mg, the solid solution that is formed around Zr particles has high Zr concentration than the neighborhood, and is usually referred to as Zr-rich cores [2]. After deformation, these cores exhibit poor DRX response and play an important role in the microstructure evolution. Mg-Zn binary alloys are mostly grain refined using Zr addition. For a given Zn concentration, Zr addition also lowers the amount of eutectic compound at the grain boundaries, so that more Zn goes in solid solution and contributes in sold solution strengthening [2]. Present study is based on two alloys AZ80 and ZK60, which belong to Al-bearing and Zr-bearing classes of Mg alloys. Because of their relatively higher solute concentrations, both alloys are high strength alloys and response well to the heat treatment.

Because of its closed packed hexagonal crystal lattice and an axial ratio (c/a ratio) of 1.624, the most active slip system in Mg alloys is the (0001) basal slip. At room temperature, the basal slip is the most active slip system, but because of the fewer number of slip systems in closed packed hexagonal lattice, basal slip does not offer five independent slip systems which are required for uniform deformation according to von-Mises criterion [3]. At room temperature, the deformation twinning requires the second lowest critical resolved shear stress after the basal slip and thus provides the additional independent deformation mode. Although the share of twinning strain is very small, but it is significant in the sense that large angle lattice rotations caused by twinning may make further slip on basal plane easier. At elevated temperatures, the critical resolved shear stresses for prismatic and pyramidal slip systems reduce considerably and the twinning contribution becomes less critical. Therefore, Mg alloys have to be deformed at elevated temperatures to activate the slip systems in addition to the basal slip. Various processes available for the deformation of Mg alloys can be grouped as conventional deformation methods, such as extrusion, rolling, forging, and severe plastic deformation methods e.g. equal channel angular pressing (ECAP), accumulative roll bonding (ARB) and high pressure torsion (HPT). Although the latter class is capable of inducing high degree of deformation and resultant ultra fine grain materials, the problems with up-scaling of the processes to industrial level and the stability of the ultra fine grain microstructure are the issues due to which these methods are still used at the laboratory scale. In contrast, the conventional methods are already in use at the industrial levels and can be readily applied to magnesium alloys. For this reason, extrusion process has been selected for the present study.

Mg alloys undergo dynamic recrystallization (DRX) upon extrusion. It is believed that even at low extrusion temperatures, the rise in internal energy is enough to cause the DRX. Deformation conditions affect the response to DRX and thus the microstructure evolution. The extrusion temperature influences the activation of various modes of plastic deformation and the nucleation sites. At lower temperatures, twinning is more active, new grains nucleate at the twin interfaces and a fine grain size is achieved. At higher temperatures, there is predominant bulging of original grain boundaries, new grains nucleate at the original grain boundaries and a relatively coarse grain size is achieved [4]. The extrusion ratio affects the degree of recrystallization and the die exit temperature. For the same value of ram velocity, a higher extrusion ratio corresponds to a higher extrusion velocity, this raises the die exit temperature and a relatively coarse grain size is achieved. A higher degree of deformation i.e. higher extrusion ratio, gives rise to a higher degree of post-extrusion secondary recrystallization and consequently weakens the texture.

The homogenization heat treatment is in general performed to remove the segregation of alloying elements that occurs due to non-equilibrium cooling during the casting process. In AZ class of Mg alloys, the homogenization treatment removes the micro-segregation of Al and Zn elements [5]. In addition, it leads to increases in hardness, UTS and elongation, without any loss of corrosion resistance [6]. Due to their closed packed hexagonal lattice and thus limited active slip systems, Mg alloys are difficult to deform. In general, the extrusion speeds in Mg alloys are 1/3 - 2/3 of the typical extrusion speeds in Al alloys. Depending upon the treatment temperature, the homogenization treatment progressively dissolves the eutectic and other intermetallic phases. This affects the deformation and recrystallization behavior of the alloy and allows higher extrusion speeds. An increase of 33% in the extrusion speed has been observed after prior-homogenization heat treatment in AZ31 alloy [7]. The second phase particles affect both nucleation and growth parts of the recrystallization, and their effectiveness depends on their sizes and interparticle distances. The coarse particles favor the particle stimulated nucleation; while, a lower interplarticle distance is more effective in pinning the boundaries during the grain growth. An effective control of the second phase particles can almost randomize the texture in wrought Mg alloys [8].

Extrusion generally leads to a partially recrystallized microstructure [9], which needs to be stabilized especially if the component is expected to perform at moderate temperatures. The static annealing after extrusion fully recrystallizes and stabilizes the microstructure. The extent and nature of grain growth and recrystallization during static annealing depend upon the degree of recrystallization during deformation [10] and temperature [11, 12] . The static annealing homogenizes [13] and weakens the texture [11], and reduces the anisotropy in mechanical properties.

Except for the deformation twinning and the pyramidal slip with <c+a> burgers vector, all other slip planes glide in this direction. Therefore, after a fairly uni-directional deformation such as extrusion, most of the grains have their basal plane normal at 90° to the extrusion direction. Such an orientation causes anisotropy in the mechanical properties, which vary not only in different directions but also depend on the sign of applied stress. In addition to elemental alloying which varies the c/a ratio of the alloy and thus determines the most favorable deformation mode, the texture in wrought alloys can be influenced by the deformation conditions such as degree of deformation, deformation temperature, prior homogenization treatment and post-deformation annealing. In essence, it depends on the relative ease of slip and twinning during deformation and the degree of dynamic recrystallization (DRX). The optimum working conditions are those which result in fine recrystallized grain size have only a weak texture, giving high strength with low degree of anisotropy.

2 Theoretical background

2.1 Wrought Mg alloys

The development of magnesium alloys started shortly after the first industrial production of this light metal. Magnesium alloys were used during the Second World War. However, there was no steady development as in the case of aluminum alloys. This is the reason for the fewer number of magnesium alloys compared to the huge number of aluminum alloys. Nevertheless, in the backdrop of rising fuel costs and environmental concerns, the low density and good damping behavior of magnesium alloys are attractive enough to shift the focus again on Mg alloys.

The principle alloying elements in magnesium alloys include aluminum, zinc, manganese, zirconium and rare earth metals. They mainly improve the strength both at room temperature and at higher temperatures. Mg cast alloys contain up to 10% aluminum, up to 6.5% zinc, up to 0.5% manganese, up to 1.5% silicon and traces of copper, nickel and iron. Special alloys have additions of rare earth elements up to 4%. Additions of silver (up to 3%) and zirconium (up to 1%) are also possible. Newly developed alloys can have contents of rare earth elements up to 10% and high levels of lithium. Wrought alloys have up to 10% aluminum, up to 2% manganese, up to 6% zinc, upto 1.5% silicon and traces of copper, nickel and iron. Though present in traces, the concentration of the heavy metals i.e copper, nickel and iron is very important for corrosion properties and for high corrosion resistance the concentration of these metals should be less than 0.05%.

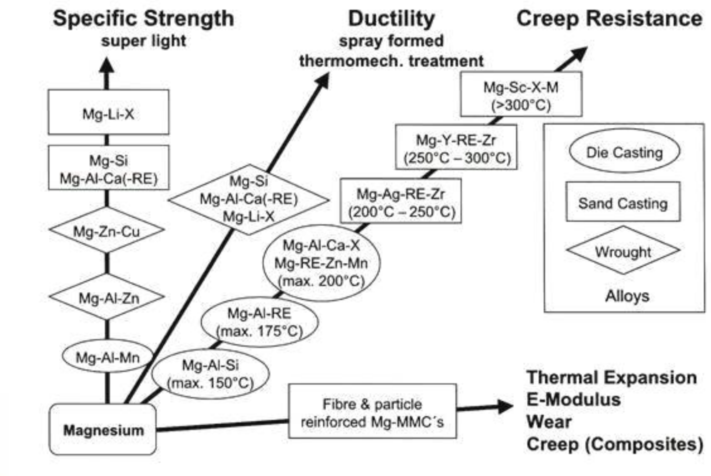

Figure 2.1: Commonly used magnesium alloys and their properties [14].

Specific Mg alloys can be classified based on their predominant properties, such as super lightness, high ductility, and good creep properties. Super lightness is achieved by adding the light metals e.g. Al, Li in to keep the specific weight low. Good creep properties in Mg alloys are achieved by introducing alloying elements such as Zr, Sc and rare earth metals, which form intermetallic compounds among themselves and thereby stabilize the microstructure at elevated temperatures. Fig. 2.1 details some of the important Mg alloys based on their significant properties [14]. Even a cursory look at the figure shows that, there are less wrought alloys than the cast alloys.

Like in other alloys, workability, *i.e.*, the capability for plastic deformation, is of paramount importance with wrought alloys, whereas cast alloys should be readily pourable and exhibit good mould-filling characteristics. Magnesium has excellent casting properties, but it is considered a hard to deform metal, especially at room temperature, due to its closed packed hexagonal lattice. Therefore, more casting alloys are available than wrought alloys in the market. On the other hand, wrought magnesium alloys have high strength which can be further enhanced by special thermomechanical treatments [15]. A comparison of the typical mechanical properties of Mg cast and wrought alloys is given in Fig. 2.2 [16]. The figure clearly shows that wrought alloys exhibit much better combination of strength and ductility than the cast alloys.

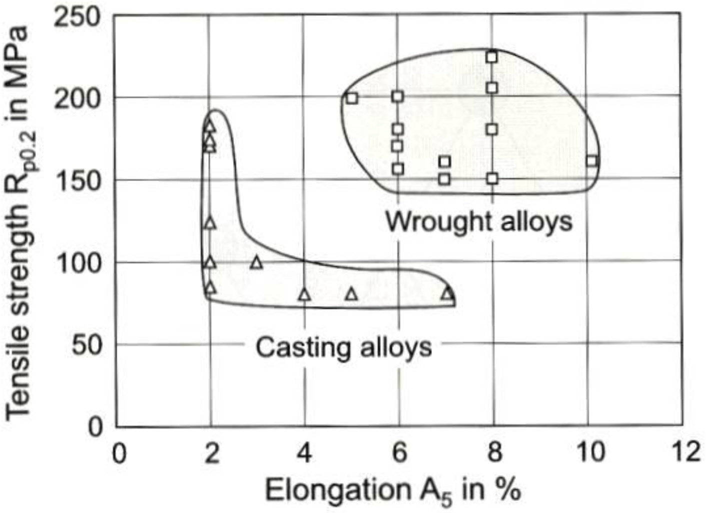

Figure 2.2: Typical mechanical properties of wrought and cast magnesium alloys [16].

Despite much higher strength and ductility, most of the Mg alloys are used in as-cast form due to their excellent casting properties. Magnesium and its alloys have a lower melting point 923 K and good fluidity. In contrast, magnesium alloys have poor ability to deform, particularly at room temperature, which is the main property required in wrought alloys. The closed packed hexagonal lattice of magnesium provide only fewer independent slip systems, which makes deformation difficult. The formability of wrought magnesium alloys improves at elevated temperatures, due to the activation of additional slip systems. Therefore, magnesium alloys are typically deformed at temperatures of 300 – 400 °C. The presence of intermetallic phases having low reaction temperatures put a limit to which the temperature can be raised. For example, in Mg–Al–Zn alloys, the eutectic phase $Mg_{17}Al_{12}$ has a melting point of $\sim$ 435 °C; similarly in Mg–Zn–Zr alloys, the eutectic phase Mg_7Zn_3 has a melting point of $\sim$ 350 °C. Therefore, in order to avoid the incipient melting of the eutectic phase during deformation, temperatures can not exceed these levels.

2.2 Deformation of Mg and its alloys

Two main deformation mechanisms slip and twinning compete against each other, when solid metals deform plastically under applied stresses and at a temperature where individual atoms are not mobile. Deformation by slip occurs on distinctive lattice planes called slip planes in certain slip direction which are characteristic for a certain crystal structure. Almost without exception the slip directions are the crystallographic directions with the shortest distance between like atoms or ions and the slip planes are usually densely packed planes. The magnitude of the shear displacement is an integral multiple of interatomic distances, so that the lattice is left unaltered after slip. In contrast, deformation twinning introduces distortions in the original lattice. The contribution of deformation twinning in total strain is much less than that of crystallographic slip. However, this little contribution is significant in the sense that significant changes in the lattice caused by twinning may orient the lattice to favor further slip.

2.2.1 Crystallographic slip

The crystallographic slip occurs when the stress acting on slip plane exceeds the critical resolved shear stress (SRSS), which in most cases is the same in tension and compression. A gradual crystal reorientation is induced by slip deformation which reverses its motion when stress is applied in the opposite direction. Fig. 2.3 shows the active slip planes and slip directions in magnesium and its alloys. It is clear from the figure that the slip systems can be categorized on the basis of slip direction as either $\langle a \rangle$ slip or $\langle c + a \rangle$ slip systems. The basal and prismatic slip planes belong to the $\langle a \rangle$ type slip systems ; whereas, the pyramidal slip planes can be either $\langle a \rangle$ or $\langle c + a \rangle$ types.

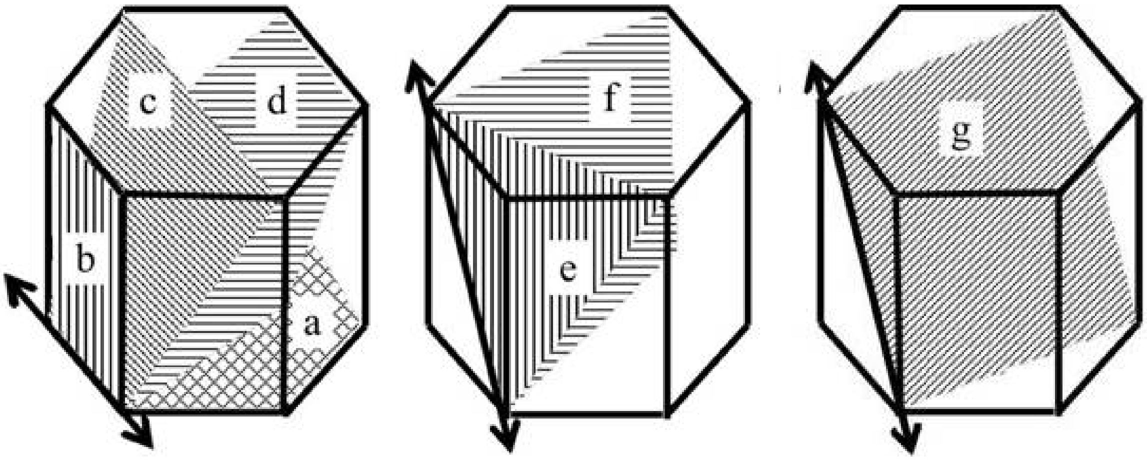

(a) $\langle a \rangle$ *slip* (b) $\langle c + a \rangle$ *slip* (c) $\langle c + a \rangle$ *slip*

Figure 2.3: Crystallographic slip systems in Mg alloys. where, a = $(0001)\,\langle 11\bar{2}0 \rangle$, b = $(1\bar{1}00)\,\langle 11\bar{2}0 \rangle$, c = $(1\bar{1}01)\,\langle 11\bar{2}0 \rangle$, d = $(1\bar{1}02)\,\langle 11\bar{2}0 \rangle$, e = $(1\bar{1}\bar{1}1)\,\langle 11\bar{2}\bar{3} \rangle$, f = $(10\bar{1}1)\,\langle 11\bar{2}\bar{3} \rangle$ and g = $(11\bar{2}2)\,\langle 11\bar{2}\bar{3} \rangle$.

For a polycrystalline material to have appreciable ductility, each of its grains must be able to undergo the same shape change as the entire body. That is, each grain in a polycrystal must deform with the same external strains as the whole polycrystal. For an individual grain this amounts to an imposed set of strains along the crystal axes. Five independent strains, namely ϵ_1, ϵ_2, γ_{23}, γ_{31}, γ_{12}, describe an arbitrary strain state or shape change, where the subscripts 1,2 and

3 correspond to the three directions in space. The third normal strain, ϵ_3, is not independent, because $\epsilon_3 = -\epsilon_1$ - ϵ_2. If a material has less than five independent slip systems, a polycrystal of that material will have very limited ductility unless another deformation mechanism supplies the necessary added freedom. Therefore, according to the Von Mises criterion, five independent slip systems must operate for polycrystals to avoid overlaps and void formations. A slip system is independent, if the shape change made by that system can not be achieved by a combination of other slip systems. The numbers and types of independent slip systems in Mg and its alloys are given in Table 2.1. The table shows that no single slip systems can provide five independent slip systems, due to the low symmetry of closed packed hexagonal lattice.

Table 2.1: Independent slip systems in Mg

Direction	*Plane*	*Slip system*	*Independent modes*
$\langle a\rangle$	Basal plane	$(0002)\,\langle 11\bar{2}0\rangle$	2
$\langle a\rangle$	Prismatic plane	$(1\bar{1}00)\,\langle 11\bar{2}0\rangle$	2
$\langle a\rangle$	Pyramidal plane	$(1\bar{1}0l)\,\langle 11\bar{2}0\rangle$	4
$\langle c+a\rangle$	Pyramidal plane	$(1\bar{1}0l)\,\langle 11\bar{2}\bar{3}\rangle$	5

$\langle a\rangle$ **slip**

The closed packed hexagonal lattice of magnesium has an axial ratio of 1.624. This implies that the $\langle 11\bar{2}\bar{3}\rangle$ crystallographic direction, which lies in the basal plane, is the shortest in Mg lattice. Therefore, most of the dislocations glide in this direction (Fig. 2.3). Out of various $\langle a\rangle$ type slip systems, the basal slip system is the most active slip system in Mg and its alloys. The reported critical resolved shear stress for basal slip is only 0.5 MPa [17], the other slip systems *i.e.* prismatic and pyramidal slip systems require 100 fold more shear stress [18]. However, due to the low symmetry of closed packed hexagonal lattice, basal slip system provides only two independent slip systems [19], which is far fewer than the five required for a homogeneous deformation. Therefore, in order to increase the formability of Mg alloys, the activity of non-basal slip systems must be increased. The activity of a non-basal slip system, i.e., the critical resolved shear stress (CRSS) for non-basal slip, depends on solute atoms, precipitates and deformation temperature [20].

At elevated temperatures, other slip systems in addition to the basal type are activated. The CRSS of the prismatic slip in Mg decreases with the increase in temperature. At room temperature it is about 100 times higher than that of the basal slip, whereas at 300 °C, it is only four times higher [14]. Activation of $(1\bar{1}00)\,\langle 11\bar{2}0\rangle$ prismatic slip system provides two additional independent slip systems. However, the basal slip and the prismatic slip systems when combined only provide a total of four independent slip systems, which is one less than the five required for homogeneous deformation (Von Mises criterion). In Mg alloys, both alloying elements and their concentrations affect the required critical resolved shear stress (CRSS) for the activation of the prismatic slip. A non-monotonic temperature dependence of the CRSS has been reported for the prismatic slip system in Mg-In and Mg-Li alloys [21, 22]. At room temperature the CRSS for prismatic slip in a Mg-In alloy increases practically linearly with the addition of In, whereas it is independent of the In concentration below room temperature [23]. The effect of concentration on CRSS of prismatic slip in Mg-Zn is complex, and is different at various temperatures [24]. The results for Mg-Al single crystals give the same trends in the temperature and concentration dependence of the CRSS for prismatic slip.

$\langle c+a \rangle$ slip

The $\langle c+a \rangle$ slip or the second order pyramidal slip is important not only due to its four independent slip systems, but also due to the fact, that except deformation twinning, it is the only slip system with imparts deformation along the c-axis of the lattice. The CRSS for the activation of $\langle c+a \rangle$ slip has not attracted as much attention as it deserves. Some old studies have been made in Mg–Li alloys, whose results show that the CRSS for second-order pyramidal slip system in Mg-Li alloys increases with increasing temperature in the range from 77-293 K. The CRSS for pyramidal slip in Mg-Li alloys is lower than that in pure Mg and decreases with the addition of lithium in a non-monotonic manner [41, 42]. The CRSS of Mg-7.5 at.% Li measured at room temperature is about a half of that of pure magnesium. The yield shear stress due to the second-order pyramidal slip system in cadmium, zinc, and magnesium crystals increases with increasing temperature. This result can be interpreted by two thermally activated processes as follows: the dissociation of a (c+a) edge dislocation with a Burgers vector of 1/3 $\langle \bar{1}\bar{1}23 \rangle$ into a c-sessile dislocation and an a-glissile basal dislocation, and the subsequent immobilization of the $\langle c+a \rangle$ edge dislocation; and consequently, the double-cross slip of $\langle c+a \rangle$ screw dislocations [25].

Various models for the evolution of the dislocation source for $\langle c+a \rangle$ slip have been suggested. One model by Yoo et al. [26] is shown in Fig. 2.4. The model suggests that the dislocation source is generated in three steps. In the first step, cross slip of a $\langle a \rangle$ dislocation occurs, the segment of this dislocation forms a $\langle c+a \rangle$ junction at the prismatic plane which cross-slips in the third stage. It is suggested that the attractive force between a $\langle c \rangle$ dislocation on the prismatic plane and the $\langle a \rangle$ dislocation on the basal plane may be sufficiently high to pull the $\langle a \rangle$ dislocation out of the basal slip [26]. In a polycrystalline material, grain boundaries are possible sites for initiation of pyramidal slip, particularly at triple grain junctions [26]. Within the grain interior, incoherent twin boundaries are also known to act as sites for generating <c+a> dislocations. When the Burgers vector of a total dislocation is large, such as that of a $\langle c+a \rangle$ dislocation in the CPH lattice, its stability with respect to possible decomposition and dissociation becomes an important factor in both dislocation source and mobility issues. For this reason, <c+a> dislocations are difficult to observe in the TEM. In deformed Ti, Mg,and Be samples, <c+a> dislocations were not observed even though they were responsible for the compressive deformation along the c-axis. When found, they were usually observed in conjunction with $\langle a \rangle$ and $\langle c \rangle$ dislocations [26].

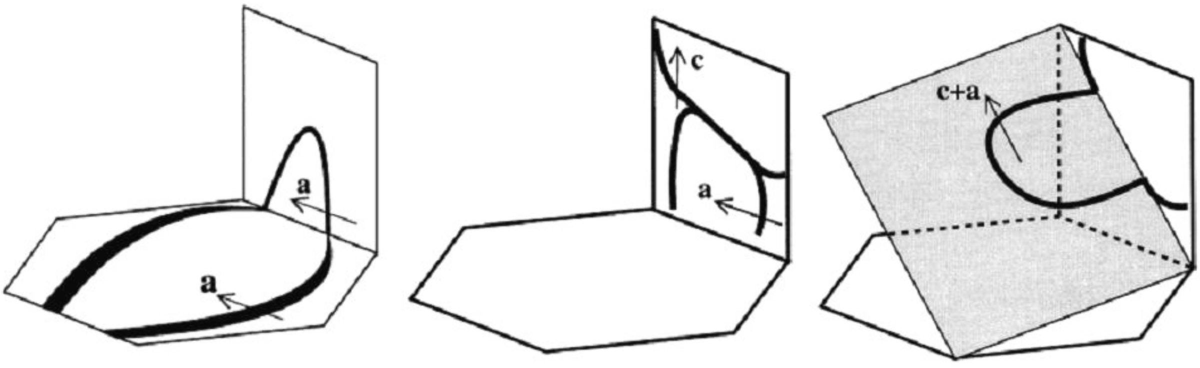

(a) Cross-slip of $\langle a \rangle$ dislocation (b) $\langle c+a \rangle$ junction formation (c) corss-slip of $\langle c+a \rangle$ dislocation

Figure 2.4: Dislocation source mechanism for $\langle c+a \rangle$ pyramidal slip [26].

2.2.2 Deformation twinning

A deformation twin is a region of a crystalline body which had undergone a homogeneous shape deformation in such a way that the resulting product structure is identical to that of the parent but oriented differently. In contrast to slip, deformation by twinning produces a homogeneous shear evenly distributed over a three-dimensional region. The total shear deformation from twinning is small and limited but can be significant in its effects. Twins at the initial stage of plastic deformation act as barriers for the basal slip in CPH metals and thus hinder the deformation and cause strain hardening [27]. Alternatively, twinning at later stages may reorient the basal planes and thereby make them favorable for slip.

The contribution of deformation twinning is particularly important at room and low temperatures. Because, at these conditions, only the basal slip is active and the prismatic or pyramidal slip require too high resolved shear stress for activation. Considerable tensile elongations in deformed Mg alloys having basal texture are also attributed to the deformation twinning [28]. As the temperature increases, additional slip systems are activated and the contribution of twinning in the deformation process becomes less critical. In addition to providing a degree of freedom in deformation process, twinning is also important in recrystallization process. In the absence of twinning, the new grains nucleate at the serrated original grain boundaries. Twin interfaces provide additional nucleation sites and thereby give fine grain size by increasing the rate of nucleation. Twinning has been observed on number of different planes in closed packed hexagonal metallic systems. Table 2.2 entails the twinning planes commonly observed in magnesium and its alloys [29].

Table 2.2: The commonly observed twin systems in Mg [29]

K_1	K_2	η_1	η_2	S	q
$\{10\bar{1}2\}$	$\{\bar{1}012\}$	$\langle 10\bar{1}\bar{1}\rangle$	$\langle \bar{1}01\bar{1}\rangle$	0.130	4
$\{10\bar{1}1\}$	$\{10\bar{1}\bar{3}\}$	$\langle 10\bar{1}\bar{2}\rangle$	$\langle 30\bar{3}2\rangle$	0.137	8
$\{11\bar{2}1\}$	(0001)	$\langle 11\bar{2}\bar{6}\rangle$	$\langle 11\bar{2}0\rangle$	0.616	2
$\{11\bar{2}2\}$	$\{11\bar{2}\bar{3}\}$	$\langle 11\bar{2}\bar{4}\rangle$	$\langle 22\bar{4}3\rangle$	0.260	6

A twinning mode is activated only under tension or compression (not both), depending upon the atomic structure, a phenomenon known as polarization. For this reason twins are generally classified as tensile or compressive twins if they cause elongation or compression along the c-axis of the lattice, respectively. The $\{10\bar{1}2\}$ twin is active in all metals having hexagonal lattice [29], and is the most frequently observed twin in Mg alloys [30, 31]. In HCP metals having c/a ratio lower than $(\sqrt{3})$ i.e. magnesium, titanium and zirconium, this is the only twin system activated during c-axis tension [32]. The directional activation of this twin system can be explained with the help of Fig. 2.5 [33]. The figure shows one of the three such possible twin systems along with the angular relationships between the undistorted $\{10\bar{1}2\}$ planes, the basal plane and the prismatic plane.

Using trigonometric rules, following relations are obtained from the figure.

$$tan\theta = \frac{C}{\sqrt{3}\,a} \quad and \quad 2\varphi + 2\theta = 180^\circ$$

The twinning strain (S) is related to the acute angle φ with the relation, $tan\,2\varphi = \frac{2}{S}$

$$\Rightarrow tan\,2\varphi = \frac{2}{S} = tan\,(180^\circ - 2\theta) \;\; or, S = \frac{tan^2\theta - 1}{tan\theta}$$

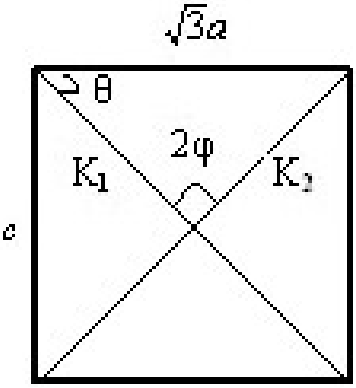

Figure 2.5: The effect of axial ratio on the sense of twin [33].

Combining the first and last equations

$$S = \left[(c/a)^2 - 3\right] \frac{\sqrt{3}\,a}{3c}$$

The equation shows that the strain caused by the $\{10\bar{1}2\}$ twins changes with the axial ratio (c/a ratio). For metals having axial ratio equal to $\sqrt{3}$ the strain is equal to zero, this implies that this twin system is not activated. The sense of $\{10\bar{1}2\}$ twinning strain changes when the axial ratio is less or higher than $\sqrt{3}$. For axial ratios less than $\sqrt{3}$, for example in Mg, Zr and Ti etc., the $\{10\bar{1}2\}$ twin causes extension in the c-axis and contraction in the a-axis. Therefore, in these metals and their alloys, this twinning system is activated when tensile stress is acting on the c-axis. Conversely, for axial ratios higher than $\sqrt{3}$ as is the case in Cd and Zn, the $\{10\bar{1}2\}$ twin causes contraction in the c-axis and extension in the a-axis [33]. Therefore, in these metals and their alloys, this twinning system is activated when compressive stress is acting on the c-axis. This very characteristic of sense in a twin causes its directional activation.

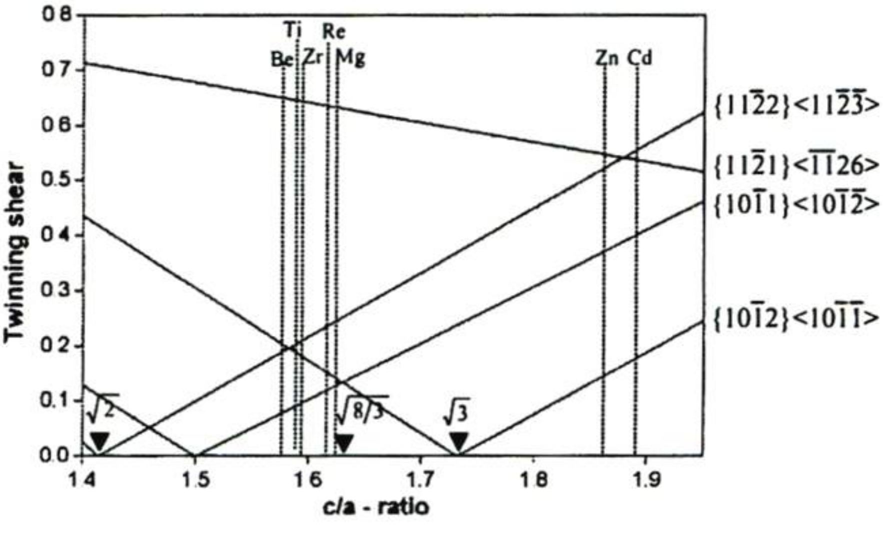

Figure 2.6: The effect of axial ratio on the sense of deformation twinning [29].

The variation of twinning sense and strain with the axial ratio is shown in Fig. 2.6 for twins commonly observed in hexagonal metals. The negative slope denotes the extension along the c-axis; while, the positive slope denotes the contraction along the c-axis. The figure shows that in magnesium metal, most of the twins are compression twins, i.e cause contraction in the c-axis. These twins frequently appear as complex doubly twinned structures that exhibit high local shear strains. A reluctance of Mg alloys to contraction twinning gives a higher value of uniform elongation [31].

2.3 Measurement and development of crystallographic texture

2.3.1 Crystallographic texture measurement

The orientation of hundreds of thousands of crystals can not be presented in a single numeric value like other physical and mechanical properties, rather it is presented graphically. There are two techniques for presenting the crystallographic texture, namely the pole figures and the orientation distribution function (ODF). The pole figure describe the 3-dimensional distribution in 2-dimension based on the stereographic projection. On the other hand, the Orientation Distribution Function (ODF) is based on the three Euler angles of rotation required to co-orientate a unit cell with a reference coordinate system. The pole figures are one of the most common method of representing crystallographic texture and sufficiently describe the global texture in most cases. Pole figures can be directly obtained by some diffraction techniques, e.g. laboratory X-ray, synchrotron X-ray and neutron diffraction techniques. Since pole figures represent the 3-dimensional crystalline orientation in 2-dimensions, they can be ambiguous if there is more than one orientation present, because each orientation is determined by several poles which cannot be associated to a specific orientation in a unique way. The orientation distribution function is usually calculated from the pole figure data. In orientation distribution function, each orientation is uniquely defined by a single point, however the 3-dimensional plots are not always easy to interpret. In closed packed hexagonal crystalline materials, the texture is most commonly determined by the pole figures and the ODF is not frequently used [34].

2.3.2 Pole figure measurement

A pole figure is a two dimensional graphical representation of the orientation of various crystallographic planes. There are two methods of this graphical presentation stereographic presentation and the equal area projection. In the stereographic presentation, a point on the surface of the reference sphere, representing the intersection of a normal of a particular crystal plane, is connected to the south pole, and the intersection of the connecting line to the plane tangent to the north pole (that is the projection plane) which defines the point on the projection plane (Fig. 2.7). In this projection method, the distances and areas between the points are not preserved, however the angles are preserved. For this reason, this is also called the equal angular projection method. In equal area projection, the circles of the same diameter on the reference hemisphere convert into ovals of the same area. Stereographic projection technique is usually used more often than the equal area projection technique and has been used in the present study. The measured pole figures are generally called incomplete pole figures, because they do not cover the whole range of the pole figure or, more precisely, they do not cover the whole asymmetric unit of the pole figure. The incomplete pole figures are completed using various calculation methods. Two commonly used methods are series expansion method introduced by Bunge [35], and Williams-Imhof-Matthies-Vinnel (WIMV) method. There are two most commonly used techniques for obtaining incomplete pole figures from diffraction data namely backscattered method and transmission method.

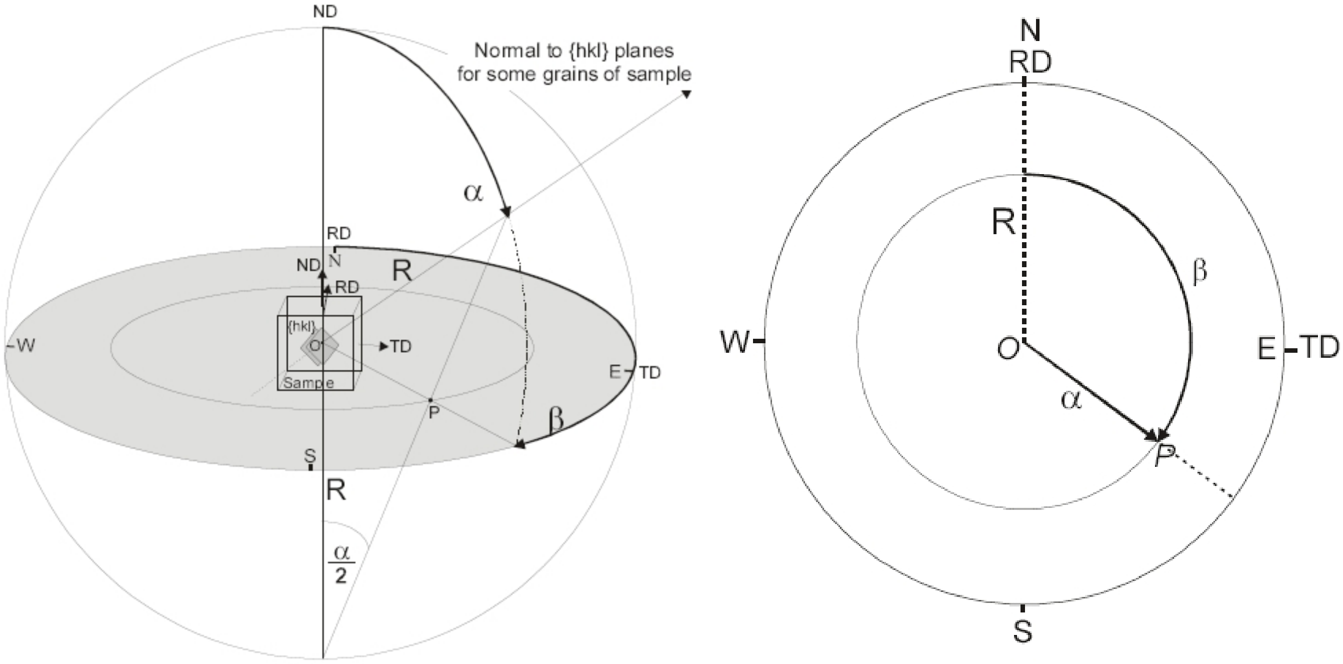

(a) Projection of a pole on a sphere (b) Projected pole on paper plane

Figure 2.7: Schematic of stereographic presentation of pole figure

The back reflection technique

As the name suggests, the back scattered technique proposed by Sculz [36] involves hitting the specimen surface with an incident beam and measuring the intensity of the reflected beam to have a point on the incomplete pole figure. The sample is rotated about the normal direction and through the angle about the intersection of the reflecting plane and the sample plane to get reflections from more grains. A schematic of the method is given in Fig. 2.8 [37].

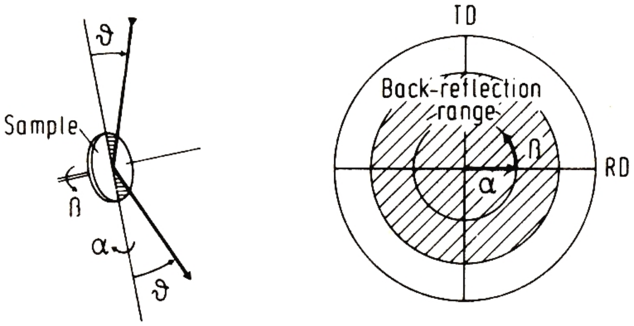

Figure 2.8: Principle of the back-reflected technique [37].

Since the incident beam hits the specimen surface in form of a cone of finite divergence, the tilting angle α becomes important due to its implications on effective cross-sectional area and broadening of the reflected beam. As the tilting angle α increases the otherwise nearly round irradiated area becomes more and more elliptical. Thus, at too high tilting angles, the effective irradiated area may become larger than the sample size (Fig. 2.9a). Therefore, the reflection method fails as the tilting angle approaches 90 ^{o}. The focusing conditions set up for the measurements are only true for the central line of the incidental cone and not for the border lines of the cone. The upper and lower parts of incident cone fall inside and outside the focusing sphere, which broadens the reflected beam. Thus, giving rise to a loss of intensity (Fig. 2.9b).

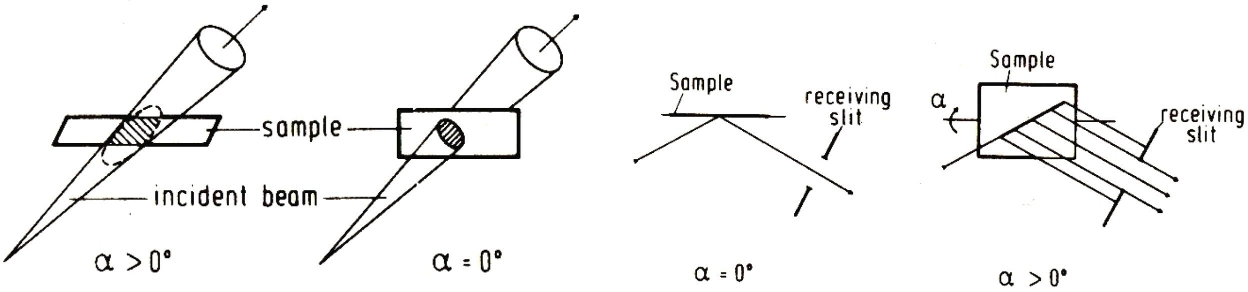

(a) Effect on irradiated area

(b) Effect on beam broadening

Figure 2.9: Effect of tilting angle on effective irradiated specimen area and broadening of the reflected beam [37].

The transmission technique

In the transmission technique proposed by Decker et. al. [38], the reflected beam leaves the sample on the opposite side of the incident beam as shown in Fig. 2.10. Similar to the back-reflection method, the sample is rotated through an angle α about an axis normal to the reflecting plane and through an angle β about an axis normal to the sample plane. Fig. 2.10 shows that in contrast to the back-reflection method, the incomplete part of the pole figure in reflection method is the central part of the pole figure *i.e.* α near to zero.

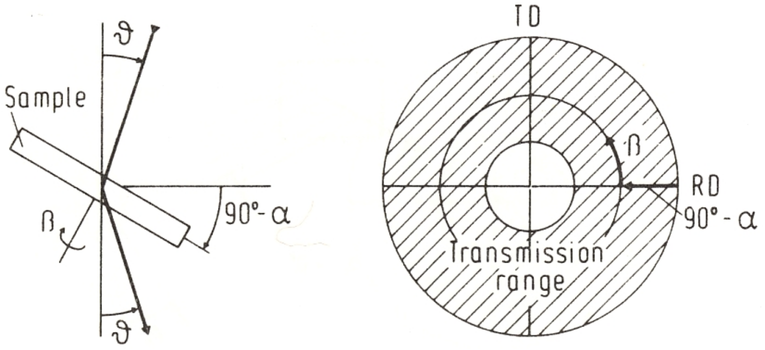

Figure 2.10: Principle of the transmission technique [37].

As in the back-reflection method, there are also geometrical and defocussing issues in transmission technique. These issues arise when the reflected or incident beam becomes nearly parallel to the sample surface. The reflectd beam gets defocussed, when the incident beam is nearly parallel to the specimen surface (Fig. 2.11a). The extent of defocussing in transmission technique is less than the one in the back-reflection method because of the absorption of irradiated beam. In the second case, when the reflected beam becomes parallel to the specimen surface, the collection to reflected beam is difficult and the method fails (Fig. 2.11a). Hence, the transmission method yields the outer parts of the pole figure provided that $\alpha > \theta$, where θ is the Bragg-angle.

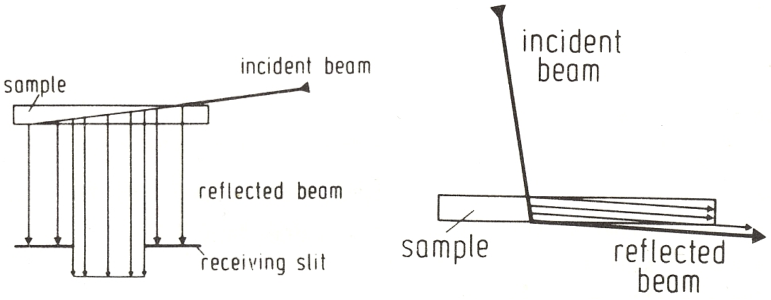

(a) Defocussing of reflected beam (b) Geometrical limitation of the method

Figure 2.11: Effect of tilting angle on effective irradiated specimen area and broadening of the reflected beam [37].

The choice of measuring technique depends mainly on the nature of incident radiation used. The back-reflection technique is commonly used in the case of X-ray diffraction. While, the transmission technique is used in the cases of neutron diffraction. In addition to the measuring technique, there are following quantitative differences between X-ray and neutron measurement.

1. The spectral distribution of thermal neutrons does not contain characteristic lines as the X-ray spectrum does. Hence, the spectral width of monochromatic beam of neutrons is correlated with its angular divergence.
2. Most of the neutron scattering takes place by interaction with the nuclei rather than the electrons. Therefore, the atomic form factor does not show the strong decrease with the Bragg-angle θ as it does in the case of x-rays. Thus, in neutron scattering, the high angle reflections are of the same order of magnitude as low angle reflections.
3. The atomic scattering factor of neutrons does not show a symmetric variation with the atomic number as in the case of X-rays.
4. The absorption of neutrons is lower than that of x-rays by a factor of the order of $10^{-3} - 10^{-4}$.
5. A part of scattering of neutrons takes place by the magnetic interaction between the spin of neutrons and electrons. Hence, the reflected beam intensity may depend on the magnetization of the sample.

Out of listed differences, the lower absorption factor is the one which is most significant with respect to texture studies and makes neutron diffraction by far superior to x-ray diffraction. For example, the penetration depths of X-ray ($\lambda = 1.54$ Å) in Al and Cu are 76 μm and 22 μm, respectively. While, the penetration depths of neutrons ($\lambda = 1.8$ Å) in same metals are 58 cm and 2.4 cm, respectively.

2.3.3 Texture development in Mg alloys

Because of the low symmetry in closed packed hexagonal lattice, the crystallographic texture is more important in these materials than in other materials having lattices of high symmetry *i.e.* cubic, BCC and FCC. The texture development in hexagonal metals strongly depends on the axial ratio (c/a ratio) of the lattice, because it determines the closed packed plane and direction along which the crystallographic slip takes place. When the c/a-ratios are above the ideal value of 1.633 such as in Cd and Zn, it tends to exhibit textures with basal poles tilted 15° to 25° away from the normal direction toward the rolling direction and the $\langle 10\bar{1}0\rangle$ prismatic poles show the maximum in the transverse direction, so called r-type texture (Fig. 2.12a) [39]. In case when the c/a ratio is approximately equal to the ideal value of 1.633, such as in Mg and Co, the textures are developed with tendency of basal fiber texture, the so called c-type texture(Fig. 2.12b. Metals and alloys with below-ideal c/a-ratios, such as Zr and Ti, tend to form textures with basal poles tilted 20° to 40° away from the normal direction towards the transverse direction, and $\langle 10\bar{1}0\rangle$ prismatic poles are aligned with the rolling direction as shown in Fig. 2.12c. The categorization by c/a-ratio is, however, a rather crude approach because many other factors influence the texture development, e.g. strain rate, temperature and chemical composition etc. All those factors have direct or indirect relation to the activity of a deformation mode, and the large variety of deformation textures in hexagonal metals are actually due to the fact that the different combinations of slip and/or twinning modes cause different textures. In Mg alloys, Philippe [40] has reported a splitting of basal poles toward the rolling direction due to the activation of $\{10\bar{1}2\}$ twinning.

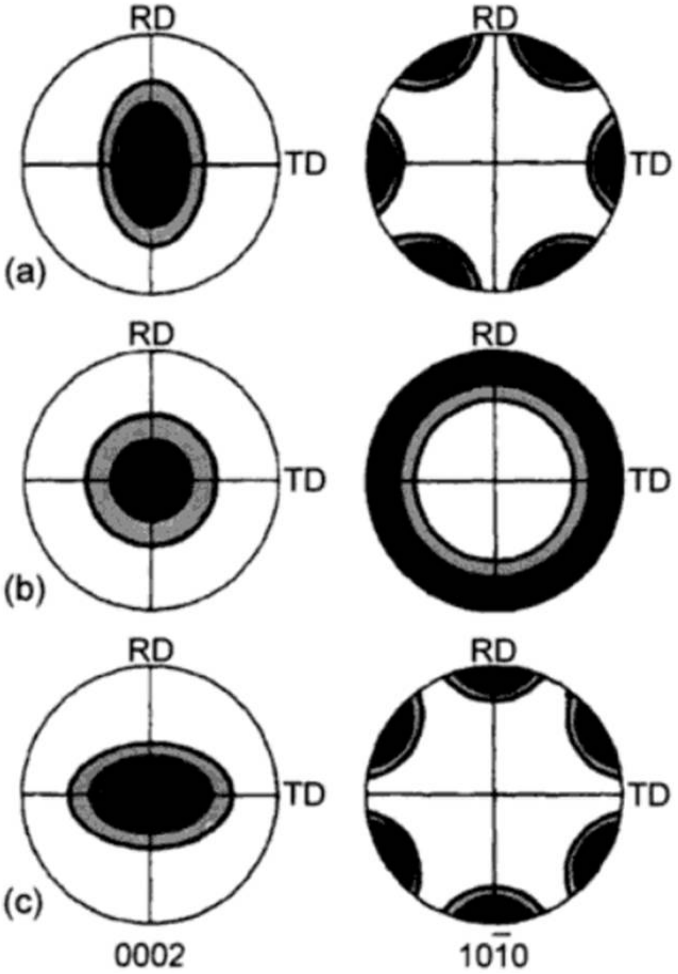

Figure 2.12: Rolling textures in various closed packed hexagonal metals [39].

During a uni-axial deformation such as round extrusion, a $\langle 10\bar{1}0\rangle$ fiber-texture, in which basal plane normals are perpendicular to the main deformation axis is most likely to be formed. This texture has been observed in extruded round rods of hexagonal metals *i.e.* Mg [41, 42], Ti [43], Zr [41] and Be [44]. The type of fiber-texture varied according to the deformation temperature and the alloying elements [43]. For example, pure Mg shows the ring type fiber-texture, in which all crystallographic directions in basal plane can be laid parallel to extrusion direction. On the other hand, $\langle 10\bar{1}0\rangle$ fiber-texture was observed in Mg alloy having Al, Mn and Zn after extrusion, while Mg alloy with 2 wt.% of Mn showed a double fiber-texture consisting of $\langle 10\bar{1}0\rangle$ and $\langle 11\bar{2}0\rangle$ fibers.

In Mg alloys all of three texture types have been observed depending on alloying elements, temperature and deformation methods. The development of c-type texture has been frequently observed in various Mg alloys, e.g. in Mg after hot rolling [45], in AZ31 alloy after hot and cold rolling [46, 47, 48], in AZ61 after hot rolling and annealing [49] and in AZ80 after hot extrusion [50]. Similar with Ti and Zr, the c-texture formation is caused mainly by basal $\langle a\rangle$ slip. The splitting of the basal pole towards the rolling direction in (0002) pole figure, r- type texture, has been reported by many authors after hot working of AZ31 [51] and AM60 [52] and after warm extrusion of rectangular bar [53]. Agnew et al. [54] simulated the evolution of r-type texture during plain strain compression of MgLi and Mg-Y alloys. They found that a good correlation with the experimentally observed r-type textures was obtained when an increasing activity of $\langle c+a\rangle$ slip is taken into account on top of basal $<$a$>$ slip and twinning. However, Courling and Wonsiewicz [55, 56] suggested that a double twinning mechanism takes place during rolling of Mg alloy. According to these authors, the increased formability can be achieved by occurrence of $\{10\bar{1}1\}$ twinning followed by $\{10\bar{1}2\}$ twinning, because contraction as well as tension along the c-axis can be accommodated by both modes. Dillamore [53] explained the splitting of the basal pole in the extruded bar by employing the double twinning mechanism. Recently, Barnett et al. [48] reported on an EBSD observation of $\{10\bar{1}1\}$-$\{10\bar{1}2\}$ double twinned structure in cold rolled Mg alloys, however, it occurs in a very small volume. In addition, they verified the existence of $\pm 20°$ tilted basal pole toward the rolling direction in shear band that was nucleated in the double twinned area.

2.4 Extrusion of Mg alloys

Extrusion, as one of the bulk-metal forming processes, is of significant importance for the production of semi-finished components. For magnesium and its alloys, the technology for processing is available today, but there is still a fundamental lack in understanding the factors that determine the development of microstructure and mechanical properties during the process [57]. As discussed earlier, due to its hexagonal crystallographic structure, deformation mechanisms observed in magnesium alloys are rather different from those in FCC metals such as aluminum and its alloys. However, processes such as extrusion involve deformation conditions which include large strain, high strain rates and moderate increase in temperature due to deformation. Magnesium alloys undergo dynamic recrystallization under these condition and the size of the recrystallized grains is much finer than the one in as-cast condition [58]. For this reason, wrought magnesium alloys have generally higher strength than the cast Mg alloys.

Grain boundary strengthening is one of the most widely used strengthening mechanisms in magnesium alloys. Since the lattice structure of adjacent grains differs in orientation, it requires more energy for a dislocation to change directions and move into the adjacent grain. The grain boundary is also much more disordered than the grain, which also prevents the dislocations from moving in a continuous slip plane. The finer the grain size, the larger is the area of grain boundaries that impedes dislocation motion. Such restrictions in dislocation movement hinder the onset of plasticity and hence increase the yield strength of the material. The behavior of yield stress as a function of grain size is usually expressed by a relation known as Hall-Petch relation,

$$\sigma_y = \sigma_o + \frac{K_y}{\sqrt{d}}$$

Where σ_y is the yield stress, K_y is the strengthening coefficient which is unique to each material, σ_o is a materials constant for the starting stress for dislocation movement, or the resistance of the lattice to dislocation motion, and d is the grain diameter. The as-cast alloys are grain refined using any of the several techniques such as, superheating, Al alloying, carbon inoculation, grain refinement using $FeCl_3$, and by Zr alloying [59], [60]. In wrought alloys, significant grain refinement is attained during plastic deformation.

The grain size is influenced by the deformation parameters such as the strain rate, the degree of deformation and the temperature. Because of their closed packed hexagonal lattice which has little symmetry and limited numbers of active slip systems, it is difficult to impart high degree of deformation in magnesium alloys without raising the deformation temperature. In general, these temperatures are higher than the recrystallization temperature of magnesium alloys, and a DRX occurs during deformation followed by the static or metadynamic recrystallization [61].

Grain refinement in Mg alloys by plastic deformation can be achieved through various techniques, which can be grouped as either conventional or large scale deformation techniques and severe plastic deformation. The conventional techniques such as rolling, forging and extrusion effectively reduce the grain size to below 10 μm and give excellent mechanical properties. With severe plastic deformation techniques, such as equal channel angular pressing [62, 63, 64, 65], accumulative roll bonding [66, 67], and high pressure torsion [68, 69] grain size can be further reduced to below 1 μm [70]. The main idea in severe plastic deformation techniques is to achieve plastic deformation without any change of size, so as to accommodate high strains. These techniques have been successful in achieving fine grain sizes; however, the mechanical properties at room temperature are comparable and at elevated temperatures are poor than the ones in conventionally deformed alloys, due to the texture and thermal stability issues. Another issue with the severe plastic deformation techniques is their limited scale nature. So far, only the small volume of the material can be severely deformed due to high load requirements. In comparison, the conventional processes are already working on industrial scale and can be readily used for magnesium alloys.

2.4.1 Effect of extrusion parameters

The extrudability of magnesium alloys can be measured by the extrusion speed. In general, magnesium alloys exhibit a lower extrusion speed than aluminum alloys and are extruded at a higher pressure level. Although higher extrusion speeds are sought for economical reasons there are limitations due to hot shortness tendencies and a reduction in mechanical properties. Hot shortness occurs when low melting phases in the billet are melted during extrusion. The alloy composition, billet microstructure and extrusion temperature are the main parameters which influence hot shortness. Both billet homogenization and a reduction in billet temperature have a beneficial effect on hot shortness and consequently allow a higher extrusion speed. Another defect usually observed after extrusion is blistering. Blistering is directly related to the surface quality of the billets. The presence of surface oxidation and solidification segregation are the main causes for the formation of blisters during extrusion of profiles. Blistering can be significantly reduced or even avoided by controlling the extrusion speed, and homogenizing the billets before extrusion.

The extrusion rate is decisively influenced by the alloying composition. Fig. 2.13a shows how significantly the required extrusion force increases with a slight increase in solute concentration [71]. Thus, in general the maximum allowed extrusion speed reduces with an increase in solute concentration. The nature of alloying elements also affects the extrudability of Mg alloys due to the thermal stability of their constituent phases. For example, the eutectic in Mg-Zn alloys has relatively lower reaction temperature (350 °C), therefore, extrusion temperature and thereby extrusion speeds can not be as high in this alloy system as they can be in other system e.g. Mg-Al, whose eutectic has much higher reaction temperature (473 °C). In addition to effects on extrudability, alloying elements and their concentration play an important role in the recrystallization process, and therefore, in the resultant mechanical properties. In general, AZ series of alloys show better response to dynamic recrystallization than the ZK series of alloys. Addition of rare earth metals, promote precipitation of various intermetallic compounds which increase the strength both at room and at elevated temperatures.

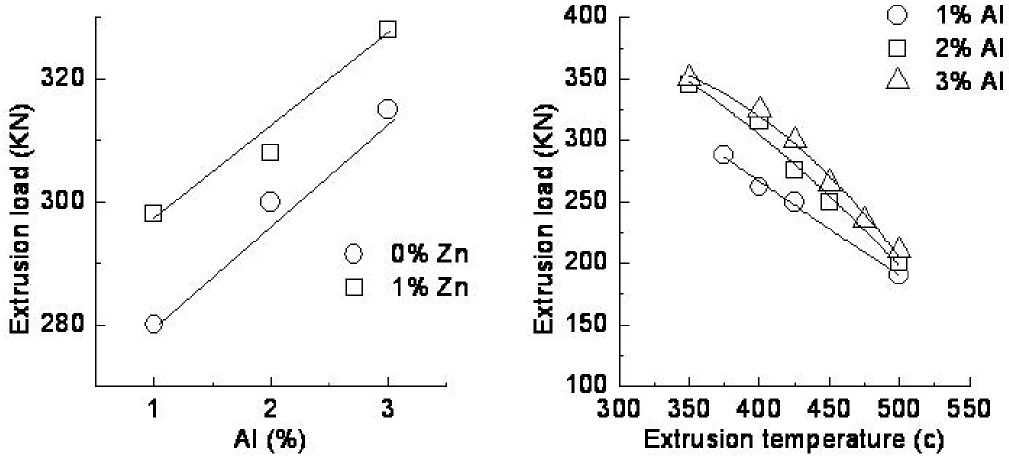

(a) Effect of solute concentration

(b) Effect of extrusion temperature

Figure 2.13: Effect of concentration of alloying elements on extrusion force [71].

In terms of force required for extrusion, extrusion temperature and ratio have opposite effects. An increase in former decreases the required extrusion force (Fig. 2.13b) due to lowering of the critical resolved shear stress of various slip systems and activation of additional slip systems which might not be active at lower temperature, while, an increase in extrusion ratio increases the strain energy required for the increased deformation. Together, these are the two most important parameters which effect the recrystallized grain size after deformation. The grain size after deformation is usually expressed in terms of a temperature compensated strain rate parameter called Zener–Hollomon parameter (Z) [4]. Z is defined as, $Z = \dot{\epsilon}e^{Q/RT}$, where $\dot{\epsilon}$ is strain rate, Q is activation energy similar to self diffusion, T is the temperature and R is the gas constant. The recrystallized grain size is inversely related to the parameter Z [72]. Thus, a lower temperature results in higher Z and finer grain size.

3 Problem definition and objectives

Magnesium alloys, due to their low density, offer a great potential for automotive and aerospace applications. However, despite their weight saving abilites, magnesium alloys could not compete with the Al alloys, in the past, due to difficulties in forming, low strength and low corrosion resistance. With the rising fuel costs and increasing environmental concerns, however, the future outlook for the magnesium alloys is very bright. Magnesium alloys have already replaced aluminum in many cast components. The application of wrought magnesium alloys, however, remains quite low. For this reason, there is a renewed interest in the field of wrought magnesium alloys [73, 74]. Compared to cast Mg alloys, fine grain sizes attained after deformation in wrought alloys give a good combination of high strength and ductility at room temperature, and superplasticity at elevated temperatures [1]. Out of currently available large scale manufacturing processes, extrusion is the best process to break a cast structure, because the material is subjected to compressive forces only [75]. Present study is aimed at investigating the effects of various extrusion variables such extrusion temperature, extrusion ratio, pre and post extrusion heat treatments on microstructure development and mechanical properties. The objectives of the study can be summarized as follows.

1. Effects of alloying elements on microstructure development and mechanical properties upon extrusion.
2. Effects of extrusion temperature and ratio on grain size and mechanical properties.
3. Effects of extrusion variables on anisotropy in mechanical properties.

Effects of alloying elements on microstructure development and mechanical properties upon extrusion

Magnesium alloys suffer from coarse grain sizes after casting and need to be grain refined using a suitable technique. In addition to enhancing strength, the alloying also helps in refining the grain size. Aluminum is one of the most common alloying element in Mg, it has a good solubility in Mg and contributes to strength by solid solution strengthening, Moreover, it forms an intermetallic eutectic phase with Mg ($Mg_{17}Al_{12}$) and causes precipitation hardening. In addition, it also helps in refining the grain size. However, Al can not be used when the alloy contains elements which form stable compounds with Al and thereby take Al out of solid solution. In such cases, other inoculants or alloying elements are added. Zn is another important alloying element in Mg alloys. It also has good solubility in Mg and forms intermetallic compounds with Mg (Mg_7Zn_3). Due to the extended solubility of solute atoms in Mg, Mg-Al and Mg-Zn alloys form a group of precipitation hardenable alloys. Binary Mg-Zn binary alloys can not be grain refined with Al addition, because they form stable intermetallic compounds. Therefore, Mg-Zn alloys are mostly grain refined using Zr addition. For a given Zn concentration, Zr addition also lowers the amount of eutectic compound at the grain boundaries, so that more Zn goes in solid solution and contributes is solid solution strengthening [2]. The refining action of Zr is attributed to the peritectic reaction between Zr and Mg, the solid solution that is formed around Zr particles has high Zr concentration than the neighborhood, and is usually referred to as Zr-rich cores. Although the total alloying elements are usually less than 10 wt%, the nature and concentration of alloying elements have a significant effect on the microstructure development upon deformation. In particular, the Zr-rich cores and intermetallic particles formed by Zr addition suppress the DRX response of the alloy [76].

One objective of the present study is to study the role of alloying elements on microstructure development upon extrusion. Two magnesium alloys, namely AZ80 (Mg–8% Al–0.5% Zn) and ZK60 (Mg–6% Zn–0.5% Zr), have been selected for this study. The alloys have been deformed under identical deformatin conditions and microstructure development and the resultant mechanical properties have been studied and compared. The influences of eutectic phases, i.e. Mg-Al and Mg-Zn in two alloys, Zn-Zr intermetallic compound and Zr-rich core in ZK60 alloy on microstructure development and their effects on mechanical properties have been determined.

Effects of extrusion temperature and ratio on grain size and mechanical properties

Grain refinement is one of the effective ways to increase the strength of Mg alloys. Several previous studies have reported the effects of extrusion parameters on recrystallized grain size. However, there are some contradicting reports. For example, Chen et al. [77] observed a gradual refinement of the grain size, from 25 μm to 4 μm in the alloy AZ31, when ER was increased from 7 to 100, while keeping the extrusion temperature and velocity constant at 250 °C and 20mm/min respectively. Ishihara et al. [78] reported an increase of the grain size, from 30 μm to 170 μm, in the same alloy AZ31 when ER was increased from 10 to 100, while keeping the extrusion temperature and velocity constant at 420 °C and 5 m/min respectively. Uematsu et al. [79] observed only slight variation in the grain size, from 5.9 μm to 4.3 μm, in the alloy AZ80 when the ER was increased from 39 to 133, while keeping the extrusion temperature and velocity constant at 330 °C and 1 m/min respectively. Swiostek et. al [80] observed that for AZ series of the extruded wrought alloys, the grain size increased with an increase in Al contents, furthermore no strength differential effect was observed for AZ61 and AZ80 alloys which were extruded at 100 °C and 110 °C, respectively.

It seems that these apparently contradicting results can be explained by considering the temperature rise caused by different extrusion velocities and will be discussed in present study.

Removing anisotropy in mechanical properties after extrusion

Extrusion, as one of the bulk-metal forming processes, is of significant importance for the production of semi-finished components. For magnesium and its alloys, the technology for processing is available today, but there is still a fundamental lack in understanding the factors that determine the development of microstructure and mechanical properties during the process [57]. As discussed earlier, due to its hexagonal crystallographic structure, deformation mechanisms observed in magnesium alloys are rather different from those in FCC metals such as aluminum alloys. In addition, the asymmetric hexagonal lattice structure leads to a strong basal texture after deformation, which causes anisotropy in mechanical properties particularly in the yield stress [58]. The YS in textured magnesium alloy varies not only in longitudinal and transverse directions but also under tensile and compressive loading, a phenomenon known as strength differential effect.

Another objective of the present study is to remove the anisotropy in mechanical properties, i.e. in YS by optimizing the extrusion parameters to weaken the crystallographic texture, to get a fine grain size, and thereby to lower the degree of anisotropy in mechanical properties.

4 Experimental methods and materials

4.1 Experimental strategy

The experimental strategy evolved in order to accomplish the aforementioned objectives (Chapter 3) is presented in Fig. 4.1. The flow diagram shows various experimental and analytical steps taken during the course of the study.

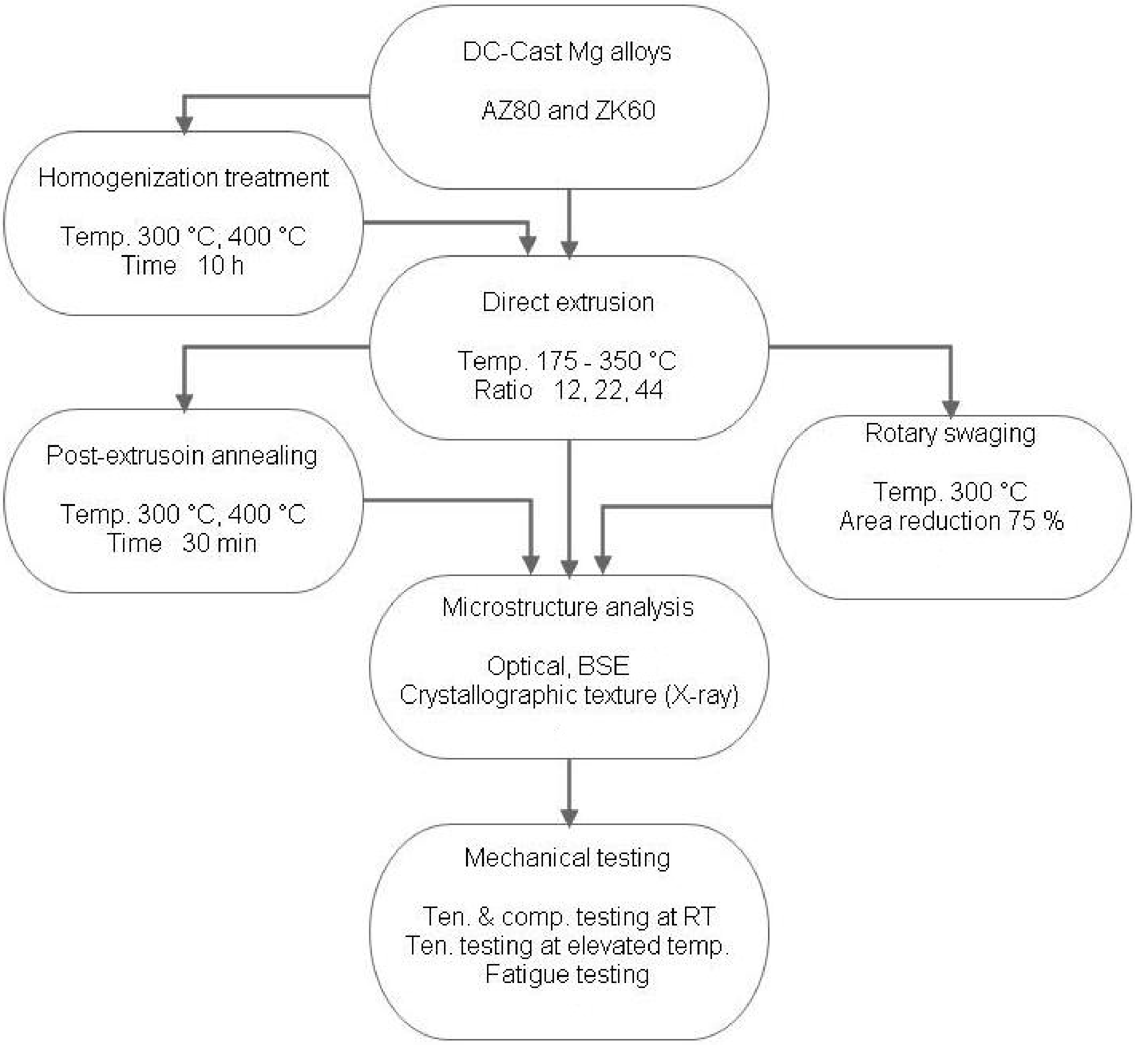

Figure 4.1: Experimental strategy.

The wrought magnesium alloys AZ80 and ZK60 were received in DC-cast condition. Before conducting direct extrusion, some of the billets were homogenized at 300 °C or 400 °C for 10 h each to study the effects of pre-extrusion homogenization treatment. Both homogenized and as-received DC-cast billets were extruded at a temperature range 175 °C $\leq$T$\leq$350 °C. Three extrusion dies with different exit diameters were used which correspond to the extrusion ratios 12, 22 and 44. Some of the as-extruded alloys were annealed at 300 °C and 400 °C for 30 min to study the effects of post-extrusion annealing heat treatment. Post-extrusion swaging was performed on some extrusions to study the effect of further deformation after extrusion. Microstructural studies were performed on as-received and various extruded profiles with the help of optical and backscattered electron (BSE) microscopy. The crystallographic texture was evaluated using X-ray diffraction. The mechanical properties at room temperature were determined by performing tensile and compression tests in as-received and various extruded conditions. Tensile tests were also performed at elevated temperatures on as-cast and extruded alloys. Fatigue behavior in as-cast and various extruded conditions was studied under rotating beam loading.

4.2 Deformation methods

4.2.1 Extrusion

Magnesium alloys are mainly extruded using the direct extrusion process. Indirect and hydrostatic extrusions are possible but are less frequently used [14]. Magnesium alloys flow more uniformly in direct extrusion than do aluminum alloys. The discards can be reduced in thickness because of the lower distortion in the region of the billet surface and the resultant flatter dead metal zone in the deformation zone of the container. The typical working temperature for extrusion varies in the range 250-450 °C depending on the alloy, and is higher than that used in hot rolling of the same magnesium alloy. Extrusion ratios similar to those for aluminum alloys can be achieved. Magnesium alloys belong to the category of difficult-to-extrude alloys mainly because of their hexagonal lattice, the extrusion speed is generally lower than the one in aluminum alloys. Both, The extrudability and the extrusion speed decrease with increasing aluminum contents. Fig. 4.2 shows the schematic of the extrusions performed in present study. Direct chill (DC) cast alloys were received in form of cylindrical billets with dimensions of 70mm × 200 mm. These billets were heated to the extrusion temperature for 1h and lubricated with MoS_2 prior to extrusion. The extrusion die was also heated to the same extrusion temperature. All extrusion were carried out a constant ram velocity of 60 mm/min.

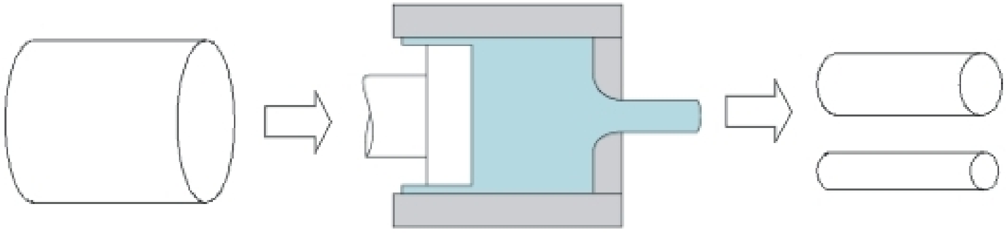

Figure 4.2: Direct extrusion process.

Three extrusion dies with different exit die diameters were used in the study. The consequent changes in the extrusion parameters are given in Table 3.1. Using a Ø20 mm die, both alloys were extruded successfully at 350 °C, 300 °C, 250 °C, 200 °C and 175 °C, whereas extrusion process failed at 150 °C. Using a Ø10 mm die, both alloys were extruded at 350 °C, 300 °C and 250 °C, while extrusions did not succeed at 200 °C. Therefore, for remaining two temperatures

(200 °C and 175 °C) a 15 mm die was used to study the effect of extrusion ratios on these temperatures.

Table 4.1: The changes in extrusion parameters with the changes in diameter of the die

Diameter mm	*Ex. ratio*	*Ex. strain*	*Ram velocity mm / min*	*Ex. velocity m / min*
10.5 mm	44	3.8	60	2.64
15.0 mm	22	3.1	60	1.32
20.0 mm	12	2.5	60	0.73

Hot shortness is one of the most commonly observed extrusion defect and is caused by localized melting at higher extrusion temperature and speeds. When the exit temperature is too high, surface melting of the individual microstructural regions such a grain boundaries occurs and results in transverse surface cracks. Similarly, extrusion at higher speeds increases the exit temperature of the extrusions leading to incipient melting at the surface and results in surface cracks. Fig. 4.3 shows the surface cracking caused in ZK60 alloy, when extrusion was conducted at a temperature higher than 350 °C. Similarly, when the extrusion speed was higher than 1 mm sec^{-1} surface cracking occurred in both alloys at lower extrusion temperatures. Therefore, 350 °C was selected as maximum extrusion temperature and extrusion speed of 1 mm sec^{-1} was kept constant for all extrusions.

Figure 4.3: Extrusion defects caused by hot shortness.

4.2.2 Rotary swaging

Rotary swaging is a hammer forming process for the reduction of cross-sections of solids, tubes and wires. The main application is the production of circular, concentric reductions. However, the process can also be used in producing other regular forms e.g. hexagonal, octagonal and square sections. Some of the advantages of rotary swaging include short cycle times, good surface finishes and tight size tolerances. A schematic sketch of a typical swaging unit is shown in Fig. 4.4 [81]. The main part of the unit consists of a 'spindle', with guiding slots which contain the dies (D) and hammer blocks (C). There is a cage containing rollers (B), which itself is contained within the machine retaining chamber (A). When the hammer blocks are between any of the rollers, there is an opening in the dies (Fig. 4.4a). As the hammer blocks strike the rollers, the dies close in and exert a blow onto the material. During rotation cycle of the spindle the dies close and open several times depending upon the the number of rollers in the roller cage (B) and the number of dies used (D), e.g. in case of Fig. 4.4, the dies close 12 times

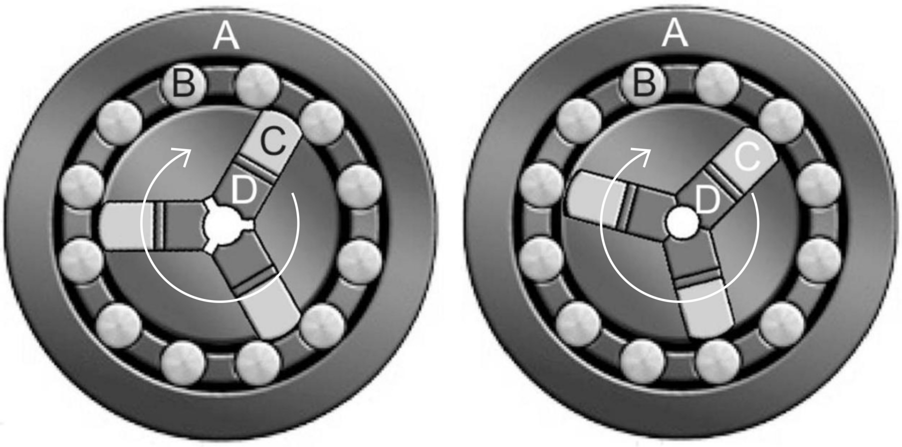

(a) Opening of dies (b) closure of dies

Figure 4.4: Schematic picture of a typical swaging unit [81].

in one cycle. The spindle rotates normally at 300-500 rpm, and during each cycle the hammer blocks repeatedly strikes the rollers (B). The frequent opening and closing of the dies allow the component to be fed into the swaging machine with little effort from the operator or automatic feeder.

In present study, the as-extruded diameter (20 mm) was progressively reduced to 10 mm in four steps (20→17→14→12→10) by post-extrusion swaging treatment. This corresponds to a total volume reduction of 75 %. The as-extruded alloys were heated to 300 °C in an oven for half an hour. The heated round profiles were swaged by the periodic hammering of dies which were at room temperature. Intermittent heating between the deformation steps was done for 10 min. After final deformation the swaged profiles were air cooled.

4.3 Heat treatments

4.3.1 Pre-extrusion homogenization treatment

The homogenization heat treatment is in general performed to remove the segregation of alloying elements that occurs due to non-equilibrium cooling during the casting process. In AZ class of Mg alloys, the homogenization treatment removes the micro-segregation of Al and Zn elements [5, 82]. In addition, it leads to increases in hardness, UTS and elongation values, without any loss of corrosion resistance [6]. Due to their closed packed hexagonal lattice and thus limited active slip systems, Mg alloys are difficult to deform. In general, the extrusion speeds in Mg alloys are 1/3 - 2/3 of the typical extrusion speeds in Al alloys. Depending upon the treatment temperature, the homogenization treatment progressively dissolves the eutectic and other intermetallic phases [83]. This affects the deformation and recrystallization behavior of the alloy and allows higher extrusion speeds. An increase of 33% in the extrusion speed has been observed after prior-homogenization heat treatment in AZ31 alloy [84]. The second phase particles affect both nucleation and growth parts of the recrystallization, and their effectiveness depends on their sizes and interparticle distances. The coarse particles (over 1 μm) favor the particle stimulated nucleation while a lower interplarticle distance is more effective in pinning the boundaries during the grain growth [85]. An effective control of the second phase particles can almost randomize the texture in wrought Mg alloys[8].

The homogenization heat treatments, in the present study were performed at 300 °C and 400 °C for 10 h each under protective environment of argon. In the case of AZ80 alloy, the eutectic phase gradually dissolves at 380-410 °C, whereas in ZK60 alloy such a dissolution occurs 300-330 °C. Therefore, a homogenization treatment at 400 °C leads to a complete dissolution of the β phase in ZK60, and a partial dissolution of β phase in AZ80 alloy. The homogenized billets were cooled in air afterwards.

4.3.2 Post-extrusion annealing treatment

Extrusion generally leads to a partially recrystallized microstructure [9], which needs to be stabilized especially if the component is expected to perform at moderate temperatures. The static annealing after extrusion fully recrystallizes and stabilizes the microstructure. The extent and the nature of grain growth and recrystallization during static annealing depend upon the degree of recrystallization during deformation [10] and the temperature [11, 12]. The static annealing homogenizes [13] and weakens the texture [11], and reduces the anisotropy in mechanical properties.

The post-extrusion annealing heat treatments, in present study, were carried out at 300 °C and 400°C for 30 min each. Since the holding time during post-extrusion annealing was short, no protective gas environment was required in this case. The post-extrusion annealing treatment was studied only in AZ80 alloy.

4.4 Analytical methods

4.4.1 Chemical analysis

The chemical composition of the alloys was measured by spectroscopic analysis using a spectrometer, which analyzes the spectrum of radiations emitted or absorbed by the sample on the basis of their wavelengths. The analytical results are shown in Table 4.2. The chemical composition in both alloys is in agreement with the nominal composition of AZ80 and ZK60 alloys. The table shows that the concentrations of heavy elements which significantly reduce the corrosion resistance in magnesium alloys, i.e. Fe, Cu and Ni are within the permissible range ($\leq$ 0.005 %).

Table 4.2: The chemical composition of the alloys in wt%.

	Al	*Zn*	*Zr*	*Mn*	*Cu*	*Fe*	*Ni*	*Mg*
AZ80								
i	8.23	0.67	0.01	0.02	0.001	0.003	0.0005	90.7
ii	8.85	0.62	0.01	0.03	0.002	0.002	0.0005	91.3
iii	8.75	0.74	0.01	0.02	0.002	0.003	0.0005	90.5
ZK60								
i	0.003	6.28	0.55	0.002	0.001	0.002	0.004	90.7
ii	0.005	6.62	0.64	0.004	0.005	0.004	0.008	91.3
iii	0.001	6.74	0.47	0.005	0.003	0.005	0.005	90.5

4.4.2 Microstructural analysis

The microstructural analysis of AZ80 and ZK60 was performed using optical and electron probe microanalysis. The former was mainly used to observe the grain size, while, the latter was used for characterization of phases and elemental line scans.

Optical microscopy

The standard metallography process of cutting, mounting, grinding and polishing was performed before etching the polished surfaces to reveal the microstructure under optical microscope. The specimens were mounted in the epoxz resin at room temperature and cured for $\sim$ 24 h. Grinding was done using water-proof sand papers containing fine SiC particles held on paper surface by a binding resin. The sand papers having grit sizes in the range 350 - 2400 were used in the study. The grit size notation is an ISO notation to denote the size of abrasive particles on sand papers. The SiC particle sizes in the cases 350 and 2400 grit sizes are $\sim 40\ \mu$m and $\sim 8\ \mu$m, respectively. The debris on sand paper produced during grinding operation were removed using water. However, an effort was made to minimize the contact time of ground surface with water and careful washing with ethanol was done during the grinding operation. After sand paper grinding down to 24oo grit paper, polishing was performed on polishing cloth using a suspension containing diamond particles. After polishing with a suspension containing 3 μm sized diamond particles, final polishing was done using a suspension having 1 μm sized diamond particles. The mirror like polished surfaces were etched using acetic-picral (10 ml Acetic acid + 4.2 g picric acid + 70 ml ethanol) and nitro-fluoric (2 ml hydrofluoric acid + 2 ml nitric acid + 96 ml distilled water) etchants for AZ80 and ZK60 alloys, respectively.

Electron probe microanalysis

Scanning electron microscopy (SEM) or electron probe microanalysis (EPMA) are generally considered micro-analytical techniques which are able to image or analyze materials that can not generally be observed with the resolution offered by light microscopic techniques. When electrons strike on the crystalline specimen surface, the following processes may occur.

1. Some of the electrons scatter in very distinct directions, which are function of the crystalline structure. This causes a so called diffraction contrast.
2. Some of the electrons may reflect back and are called reflected or backscattered electrons.
3. The striking electrons may cause the specimen to emit electrons, which are called secondary electrons.
4. The striking electrons may cause the specimen to emit characteristic X-rays, whose energy and wavelength are related to the specimen composition.
5. The striking electrons may pass through the specimen, if the specimen thickness is small. These electrons are called transmitted electrons.

In the case of SEM, the surface of the specimen is scanned by an electron beam generated by the electron source of the microscope and the secondary electrons detected by the secondary electrons detector are used for making a contrast image formed by the interaction of electrons with the specimen. The end result is therefore brightness variations associated with surface characteristics known as topographic contrast. The SEM is designed for ease of use and for a variety of specimens. In contrast, the back scattered electron (BSE) image is made of the intensity contrast of the electrons which come from the electron source of the microscope and are back reflected after interacting the specimen. The backscattered electrons posses much higher energy than the secondary electrons and the intensity of BSE depends upon the atomic number of the specimen. Thus, the contrast in BSE image depends on the chemical composition. The chemical composition of the various specimen constituents can be quantitatively analyzed by energy dispersive X-ray analysis (EDX) or wavelength dispersive X-ray analysis (WDX) of the characteristic X-rays that emit from the specimen. wave dispersive x-ray (WDX) analysis is much more sensitive to low elemental concentrations than are EDX. The concentrations in the range of 500-1000ppm can generally be measured using WDX, while, for some elements within some types of materials, the detection limit can be near 20ppm.

The standard specimen preparation procedure described in the earlier section for optical microscopy was adopted for electron probe microanalysis. However, the specimens were not etched. The surface of the mounting resin were made conducting by coating it with graphite.

4.4.3 Crystallographic texture analysis

Crystallographic texture in present study has been analyzed using the X-ray diffraction . The back reflection technique or Schultz method has been adopted for measuring the crystallographic texture. The process is illustrated in the Fig. 4.5a. After setting up the specimen and source for a certain planar peak, the specimen is rotated (β in Fig. 4.5a) and tilted (α in Fig. 4.5a) and the intensity of diffracted radiation is analyzed by the detector.

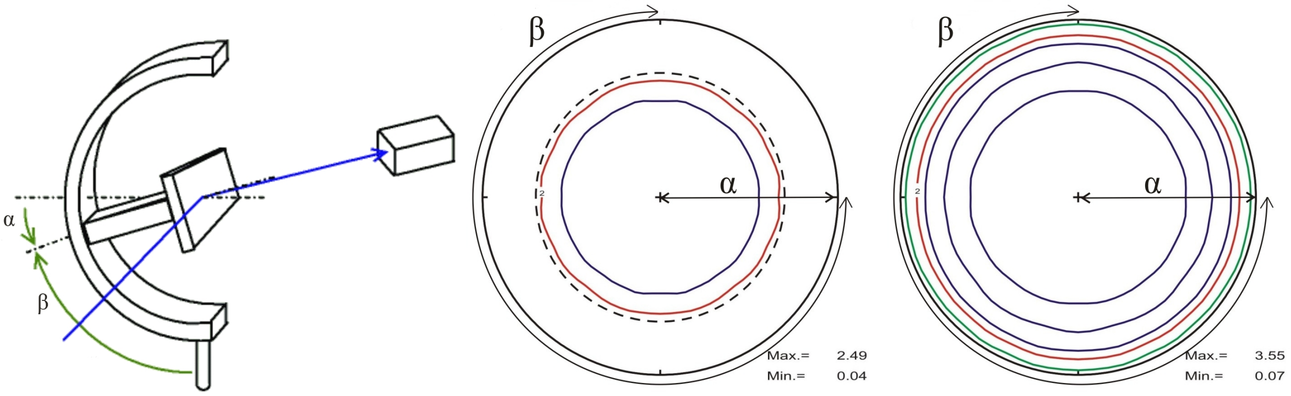

(a) Back reflection method (b) Experimental pole figure (c) Calculated pole figure

Figure 4.5: Scheme of back reflection X-ray technique for texture measurement.

The measured pole figure (Fig. 4.5b) shows the measured intensity on the Wulf net. Because of the operational restriction, the specimen have only been rotated to 350^o and tilted only to 70^o. Thus, the measured pole figure Fig. 4.5 shows only data up to 70^o in the α direction. For this reason, the measured pole figures are also called incomplete pole figures. The complete pole figure or calculated pole figure (Fig. 4.5c) is obtained from mathematical calculations. The series expansion method or harmonic method is the most commonly used method for calculating the full pole figures from measured data, and has been used in present study. The basic premise of the series method is the assumption that both the measured pole figures and the orientation distribution function (ODF) can be fitted by a series expansion with suitable functions. Appropriate functions to use in a spherical coordinate system are the spherical harmonic functions, and therefore this method is also called the harmonic method.

X-ray diffraction in present study has been performed using K_α radiation of cobalt (Co) source . The scan time for each degree of rotation and tilting was 3 sec. The samples for texture analysis were taken from the middle section in the length. A transverse surface was always analyzed for the X-ray diffraction. The reference extrusion direction on the pole figures is therefore, the ND or normal to the paper plane.

4.4.4 Mechanical testing

Tensile and compression testing at room temperature

The tensile and compression tests were performed on a Instron 5582 Series testing machine. The strain during tensile tests was measured using Instron proprietary extensometer up to 1% engineering strain, after which the extension data is calculated from the movement of travelling crosshead. The samples for a uniaxial tension test at room temperature were machined to a gauge length of 25 mm having a 5 mm diameter (Fig. 4.6a. For compression tests, two specimens geometries presented in Fig. 4.6 c,d were used. The results showed no buckling in the 1:2 ratio specimen i.e. 20 mm height, and were always within the statistical range to that of 1:1.2 specimen i.e. 12 mm height specimen. Specimens for compression tests were machined along the extrusion direction (longitudinal or 0° sample), perpendicular to the extrusion direction (transverse or 45° sample) and an intermediate angle between longitudinal and transverse directions (intermediate angle or 45° sample). Because of the size limitation, such a variation was not possible for tensile testing, therefore, tensile tests were only performed in longitudinal direction. All the tensile and compression tests were conducted at an initial strain rate of 10^{-3} s^{-1}. A minimum of two tests were performed in each condition.

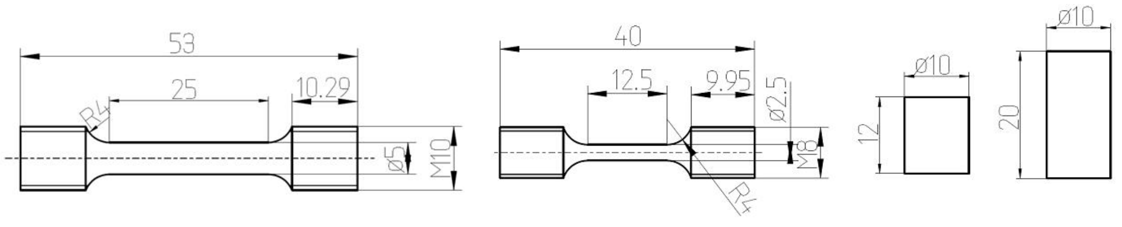

(a) T1 (b) T2 (c) C1 (d) C2

Figure 4.6: Technical drawings of the tensile specimens (T1 and T2) and compression specimens (C1 and C2) used in present study.

Tensile testing at elevated temperatures

Tensile tests at elevated temperatures 100≤ T ≤ 350 °C were conducted on the same Instron 5582 Series machine using a chamber attachment containing a 3-zone heating furnace. Before the start of tensile tests, the attached chamber was heated and held at the testing temperature for 30 min. The tensile specimens were then inserted and held at the testing temperature for 10 min. Most of the tensile tests were conducted at an initial strain rate of 10^{-3} s^{-1}, however, for some experiments, the strain rate was varied. The extension during tensile tests at elevated temperatures was taken from the machine data based on the movement of the cross head. Tensile specimens used for testing at elevated temperatures had the same dimensions and geometry as those used at room temperature. Due to the limiting size of the chamber, the maximum extension allowed was only ∼ 300%. The flow behaviors at various temperatures

(Figs. 5.31, 5.32 and 5.33) were measured using the long specimen (gauge length 25 mm). While, in order to determine the maximum tensile elongation at varous temperatuers (Fig. 5.34), specimens with shorter length (gauge length 12.5 mm) were used. However, the gauge length to gauge diameter ratio was kept the same.

Fatigue testing

Fatigue performance in present study has been studied under rotating beam loading, which involves constant rotation of the specimen while applying a load at one end of the specimen and keeping the other end fixed. Thus, the top and bottom surfaces of the specimen experience cyclic tension and compression stresses. The amount of the stress is constant under both modes and depends on the diameter of the specimen. The outer surface experiences the highest stress while the central part is under a state of no stress. As a result, fatigue strength is also affected by the specimen size. Thicker sections provide greater surface area for crack initiation and have higher probability of material inhomogeneity caused by casting defects in cast alloys or non-homogeneous deformation in wrought alloys. Therefore in general, fatigue strength reduces and notch sensitivity increases in case of larger specimen size. The dimensions of the hourglass shaped fatigue specimens used in present study are shown in Fig. 4.7. The specimen F1 was used in as-cast and as-extruded conditions, while, specimen F2 was used in post-extrusion swaged conditions because it was not possible to machine the specimen F1 out of swaged profile (8 mm diameter).

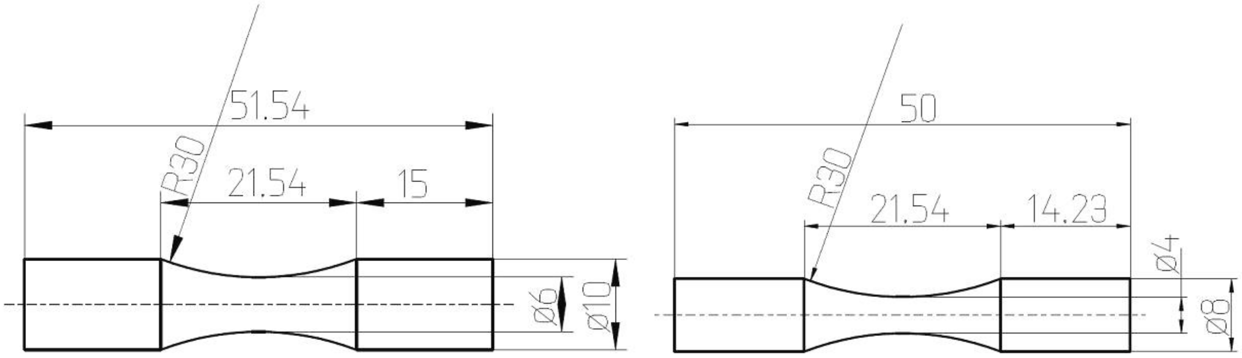

(a) Specimen F1

(b) Specimen F2

Figure 4.7: Technical drawings of the fatigue specimens used in the study.

High cycle fatigue strength is strongly affected by the surface condition. Sharp notches, small radii, fretting and corrosion are more likely to reduce fatigue life than the variations in chemical composition or heat treatment. The fatigue performance of the cast alloys is improved by removing the relatively rough as-cast surface by machining. The fatigue life of the cast and wrought samples can be further increased by cold working the surface which induces compressive residual stresses and decreases the rate of crack propagation. Compressive residual stress may also be induced during specimen fabrication in magnesium alloys. Therefore, fabricated samples were polished electrolytically to remove a surface layer of 100 μm. The electrolytic solution used in present study consisted of ethylene glycol monoethyl ether (90%) and hydorchloric acid (10%).

5 Experimental results

5.1 Effect of extrusion parameters on microstructure development

5.1.1 Microstructure in as-received condition

The optical micrograph of the DC-cast alloy AZ80 Fig.5.1a reveals an average grain size of about 100 μm and the divorced eutectic constituents, which can be better appreciated in the backscattered electron (BSE) image Fig. 5.1b. In addition the figure also shows fairly round shaped particles.

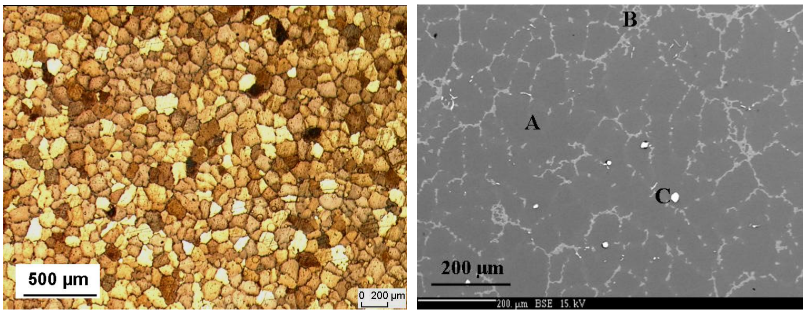

(a) OM image (b) BSEM image

Figure 5.1: Microstructure of as-cast AZ80 alloy.

The wave dispersive X-ray (WDX) analysis of the various features visible in Fig. 5.1b is given in Table 5.1, the letters A, B and C correspond to the features marked in Fig. 5.1b. The analysis shows that eutectic constituents are rich in Mg and Al and their relative proportion is close to that of $Mg_{17}Al_{12}$. In addition, there are particles rich in Al and Mn (marked by letter c in Fig. 5.1b) having a proportional relation close to that of Al_8Mn_5. These analytical results are in agreement with earlier reported studies [86] and [87]

Table 5.1: Wave dispersive X-ray analysis of various regions in as-cast AZ80.

	Mg(wt%)	*Al(wt%)*	*Zn(wt%)*	*Mn(wt%)*
Matrix (A)	88.36	6.14	0.37	0.016
Eutectic (B)	55.20	36.74	1.20	0.03
Particle (C)	5.80	40.25	0.08	46.55

The optical and backscattered electron micrographs of the as-received ZK60 alloy are shown in Fig. 5.2. The optical microgrpah of the alloy in the as-received condition (Fig. 5.2a) shows fairly equi-axed grains having an average size of 100 μm, and the eutectic constituents at the grain boundaries. These constituents can be better appreciated in the back scattered electron (BSE) image presented in Fig. 5.2b.

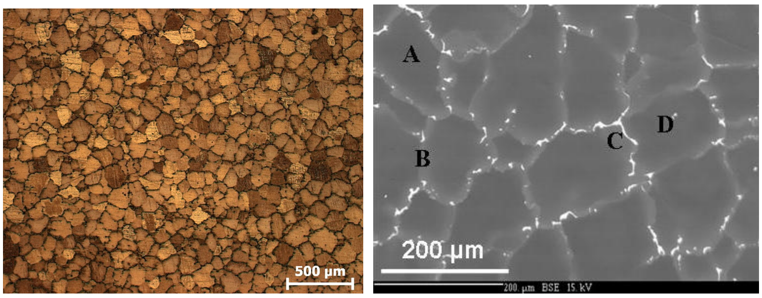

(a) OM image (b) BSE image

Figure 5.2: Microstructure of the as-received ZK60 alloy.

The wave dispersive X-ray (WDX) analysis, presented in Table 5.2, shows the chemical composition of the four representative regions marked with letters A-D in Fig.5.2b. The region (A is rich in Zr and lean in Zn compared to the region (B) which represents Zn-rich rings at the grain boundaries. The eutectic constituents at the grain boundaries (C) are Mg-Zn based and the relative proportion of Mg and Zn is close to that of the Mg_7Zn_3. Because of their fine sizes and therefore a significant influence of the neighborhood in WDX analysis, the Zn-Zr intermetallic particles show a large variation in the concentration (20-50 wt% Zr). Previous studies conducted in Mg-Zn-Zr alloys have characterized them as $ZnZr_2$ or Zn_2Zr_3 [4, 88].

Table 5.2: Wave length dispersive X-ray analysis of various regions in as-cast ZK60.

	Mg(wt%)	*Zn(wt%)*	*Zr(wt%)*
Matrix (A)	94 - 95	1.8 - 2.0	1.0 - 1.4
Zn-rich ring (B)	88 - 90	4 - 7	0.1 - 0.3
Eutectic (C)	63 - 66	25 - 30	0.02 - 0.04
Particle (D)	5 - 10	15 - 50	20 - 50

The WDX line scan presented in Fig.5.3 shows the variations in the concentrations of Zn and Zr across a grain. The results show that the concentration of Zr varies within the grain and shows a peak value at the core of the grain. These cores are formed during the casting process around Zr rich particles which are added to refine the microstructure by peritectic reaction with liquid Mg [2, 76]. In comparison, Zn concentration remains fairly consistent within the grain and has a maximum value at the grain boundary. Thus, the microstructure in as-cast condition is highly segregated in terms of solute concentrations. Out of 6 wt% Zn only 2 wt% is present in the bulk grains and the remainder Zn segregates to grain boundaries and forms eutectic compound. The concentration of Zn at grain boundaries is about 7 wt%, which is equal to the maximum solubility limit of Zn in Mg at eutectic temperature.

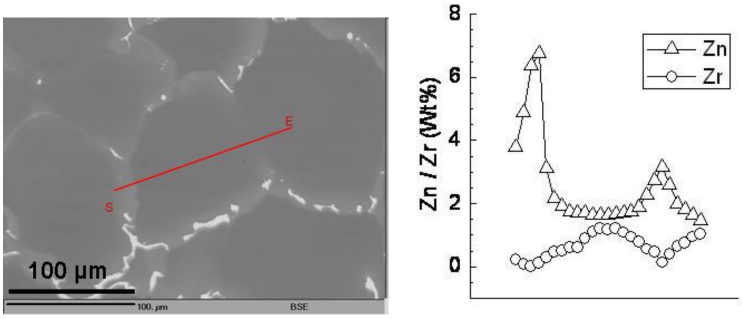

Figure 5.3: Wavelength dispersive X-ray analysis (WDX) line scan of as-cast ZK60 alloy.

5.1.2 Effect of homogenization treatment on microstructure development

The backscattered electron micrographs presented in Fig. 5.4 show the effect of homogenization treatment on the microstructure of AZ80 alloy. The homogenization treatment was carried out at 400 °C for 10 h under the protective environment of Ar. Since the selected temperature is lower than the eutectic temperature (473 °C), the homogenization treatment results in partial dissolution of eutectic β-phase. The Fig. 5.4 shows that homogenization heat treatment dissolves over 80% of the the divorced eutectic β-phase ($Mg_{17}Al_{12}$). However, the Al-Mn particles are not affected by the homogenization treatment because of their higher reaction temperature.

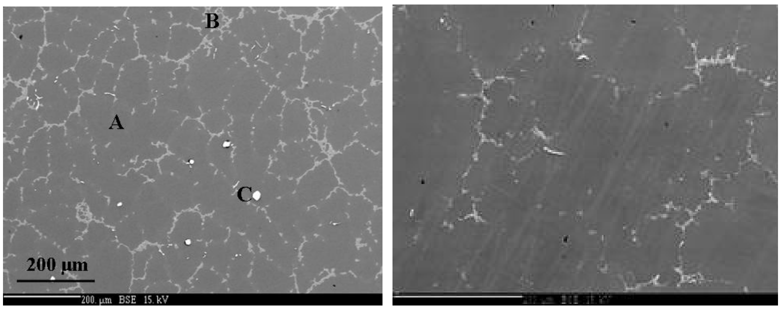

(a) Before homogenization (b) Homogenized at 400 °C

Figure 5.4: Effect of homogenization treatment on microstructure of as-cast AZ80 alloy.

The backscattered electron micrographs of ZK60 alloy before and after homogenization at 300 °C and 400 °C for 10 h each are shown in Fig. 5.5. The micrograph before homogenization shows Mg-Zn eutectic phase and Zn-rich ring at the grain boundary. After homogenization treatment at 300 °C, the microstructure shows partial dissolution of eutectic phase and the concentration of Zn in Zn-rich rings present at the grain boundaries decreases, as indicated by a less bright contrast in Fig. 5.5b. In contrast, the homogenization treatment at 400 °C for 10 h completely dissolves the eutectic phase and the Zn-rich rings disappear (Fig. 5.5c).

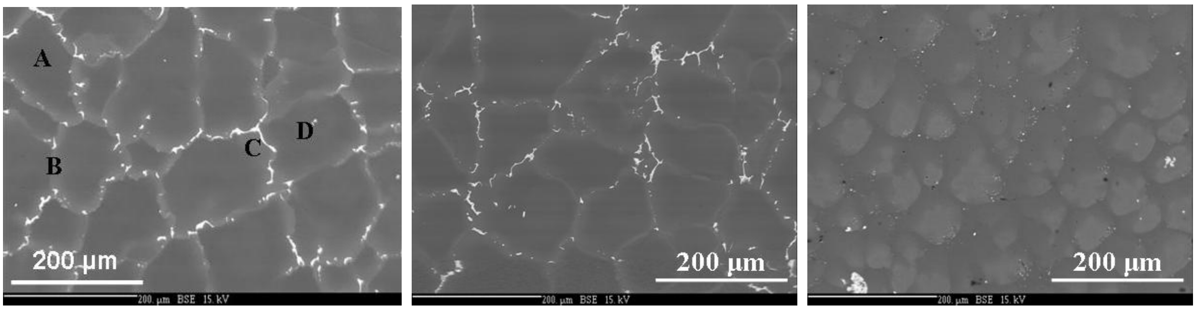

(a) Before homogenization (b) Homogenized at 300 °C (c) Homogenized at 400 °C

Figure 5.5: Microstructure of as-cast ZK60 alloy before and after homogenization treatment.

Although, the homogenization at 400 °C for 10 h has profound effects on eutectic phase and Zn-rich rings, the Zr-rich rings present in the as-cast condition (5.3) are not affected by the homogenization treatment. The WDX line scan presented in Fig. 5.6 indicates that Zr-rich cores are still present at fairly in the middle of a grain after the homogenization treatment. Furthermore, the results show that the concentration of Zn is maximum at these cores. In comparison, the concentration of Zn was maximum at the grain boundaries (5.3). A higher concentration of Zr increases the solubility of Zn in Mg and therefore causes an uphill diffusion of Zn to Zr-rich cores.

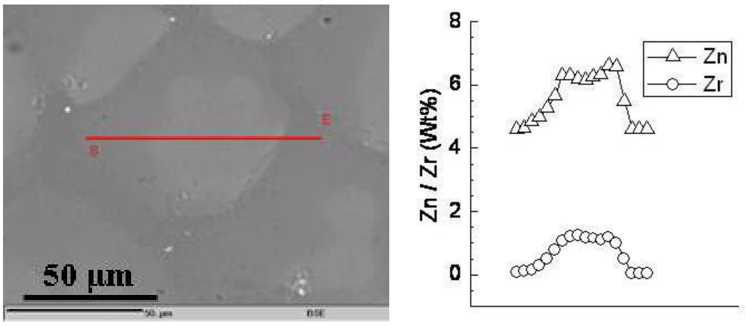

Figure 5.6: A line scan in as-cast ZK60 alloy based on Wave dispersive (WDX) X-ray analysis.

5.1.3 Microstructure development during extrusion

The backscattered electron and optical micrographs of the extruded AZ0 alloy are illustrated in Fig.5.7.The optical micrographs for extrusion ratio 12 (Fig.5.7a) and extrusion ratio 44 (Fig. 5.7c) show that in as-extruded condition, the microstructure consists of recrystallized equi-axed grains much finer than the one observed in the as-cast condition (Fig. 5.1a). the micrograhps in Fig.5.7 show bands of stringers parallel to extrusion direction at both extrusion ratios. The cross-section of these stringer is finer in the case of higher extrusion ratio.

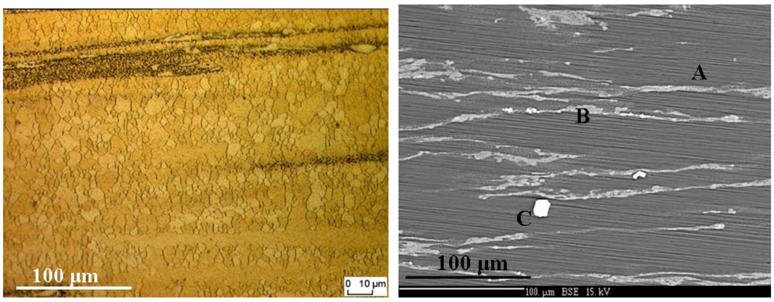

(a) OM, ER12 (b) BSE, ER12

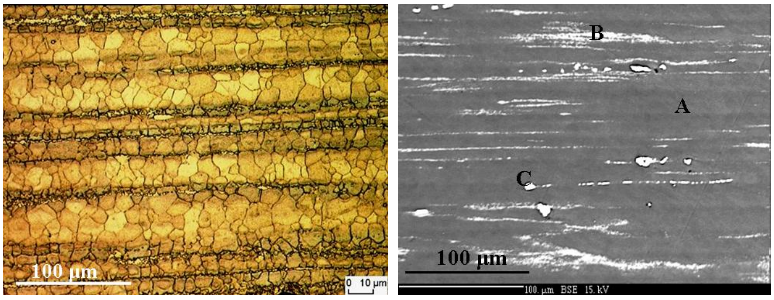

(c) OM, ER44 (d) BSE, ER44

Figure 5.7: Optical and backscattered electron micrographs of AZ80 alloy extruded at 300 °C.

The results of WDX analysis is presented in Table 5.3 for the regions marked with letters A-C in backscattered electron micrógaphs Fig.5.7b and Fig.5.7d for extrusion ratio 12 and 44, respectively. The analysis reveals that the stringer bands consist of β-phase ($Mg_{17}Al_{12}$). In comparison to extrusion ratio 12, these bands are finer in the case of ER44. In addition, Figs. 5.7b and 5.7d show the Al-Mn rich particles which were present in the as-cast condition (Fig. 5.1b). Their relative sizes indicate that they remained unaffected during the extrusion process.

Table 5.3: Wave length dispersive X-ray analysis of $as-extruded$ AZ80 alloy.

	Mg(wt%)	*Al(wt%)*	*Zn(wt%)*	*Mn(wt%)*
Matrix (A)	88.36	6.14	0.37	0.016
Eutectic (B)	55.20	36.74	1.20	0.03
Particle (C)	5.80	40.25	0.08	46.55

The optical and backscattered electron micrographs of the ZK60 alloy extruded at 300 °C are given in Fig. 5.8. In contrast to AZ80 alloy, the figure shows that extrusion ratio plays an important role in the microstructure development. The optical microstructure at both extrusion ratios show two populations of grain sizes. The coarse grains are of 10-20 μm size while fine grains are of 2-5 μm size. In addition to the recrystallized grains, the optical micrographs show elongated regions which have not recrystallized. These regions are wide and hence can be easily seen in the case of lower extrusion ratio.

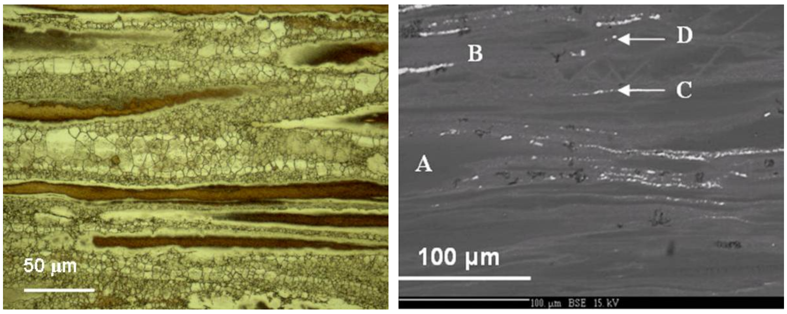

(a) Extrusion ratio = 12 (b) Extrusion ratio = 12

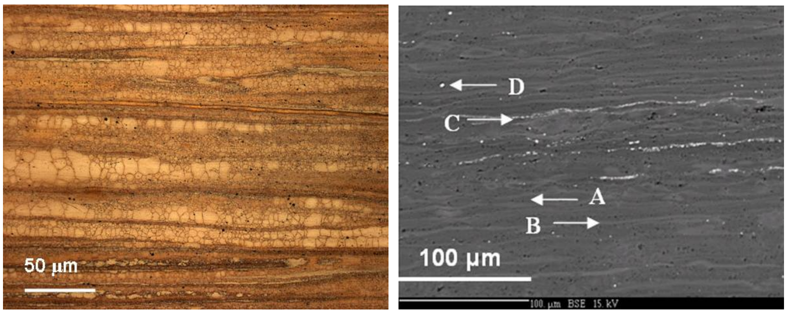

(c) Extrusion ratio = 44 (d) Extrusion ratio = 44

Figure 5.8: Optical and backscattered electron micrographs of ZK60 alloy extruded at 300 °C.

The WDX analysis is presented in Table 5.4 for the regions marked with letters A-D in backscattered electron micrographs Fig. 5.8b and Fig.5.8d for extrusion ratio 12 and 44, respectively. The electron probe microanalysis reveals that the elongated regions are Zr-rich and Zn-lean, similar to the cores of the grains prior to extrusion. Furthermore, it shows that upon extrusion, diffusion of Zn from Zn-rich rings takes place and the peak value of Zn concentration decreases from 7 wt% to 5.5 wt%. After unidirectional deformation during extrusion, the eutectic constituents form stringers in the extrusion direction (marked by C in Fig. 5.8) and some of the eutectic constituents decompose to a more Zn bearing compound (Table 5.4).

Table 5.4: The wave dispersive X-ray analysis of various regions in as-extruded ZK60.

	Mg(wt%)	*Zn(wt%)*	*Zr(wt%)*
(A)	94 - 95	2.0 - 2.5	1.0 - 1.4
(B)	88 - 90	4.5 - 5.5	0.1 - 0.3
(C)	63 - 66	25 - 30	0.02 - 0.04
	25 - 30	50 - 65	0.02 - 0.04
(D)	5 - 10	15 - 50	20 - 50

5.1.4 Effect of extrusion temperature and ratio on microstructure development

The optical micrographs of the AZ80 alloy extruded at selected temperatures are presented in Fig. 5.9. For each extrusion temperature, the figure shows microstructures corresponding to two extrusion ratios. At lower temperatures, i.e. 175 °C and 200 °C, the extrusion was not successful at ER44. Therefore, extrusions at ER22 were performed to have a comparison at these temperature (Fig. 5.9f). The microstructures in all cases consist of recrystallized equiaxed grains, parallel bands of β-phase stringers and Al-Mn particles (as characterized by the WDX analysis, Table 5.3).

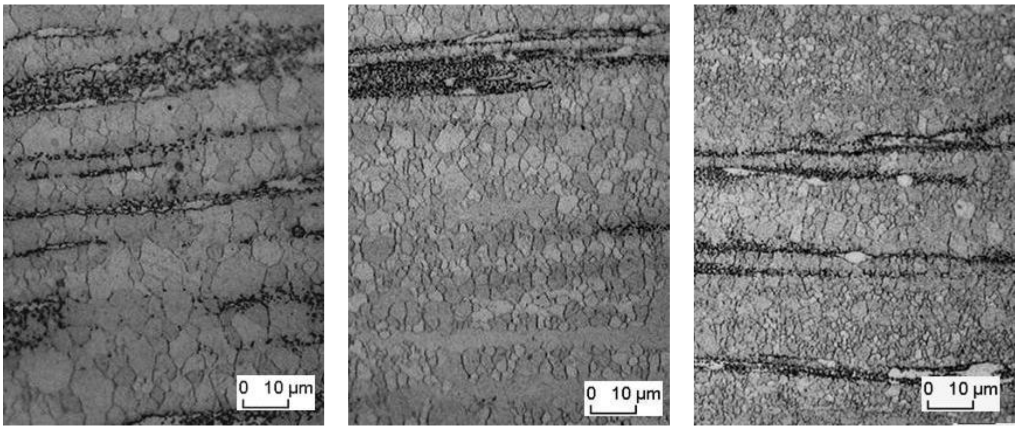

(a) ET 350 °C, ER 12 (b) ET 250 °C, ER 12 (c) ET 175 °C, ER 12

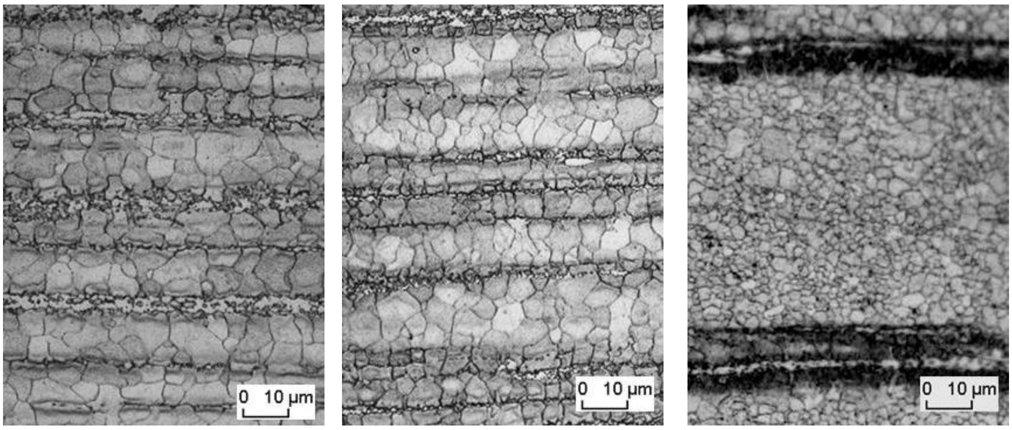

(d) ET 350 °C, ER 44 (e) ET 250 °C, ER 44 (f) ET 175 °C, ER 22

Figure 5.9: Optical microstructure of extruded alloys at various extrusion temperatures (ET) and extrusion ratios (ER).

The average grain sizes measured by the liner intercept method for all the extruded alloys are given in Table 5.5. The table shows a progressive refinement in the grain size from 8 μm to 4 μm with the lowering of extrusion temperature from 350 °C to 175 °C, while the grain sizes are slightly coarser at higher extrusion ratios. The lowering of extrusion temperature, and thus increased contribution of deformation twinning, provides additional nucleation sites at twin interfaces and also result in a lower degree of secondary recrystallization. Therefore, a finer grain size is observed with the lowering of extrusion temperature. The extrusion ratio has a direct bearing on strain rate and degree of deformation, which are important variables for the dynamical recrystallization and the subsequent static recrystallization, respectively. In general, a higher extrusion ratio enhances the degree of recrystallization and lowers the grain size. The results presented in Fig. 5.9 and Table 5.5 show that even the lower extrusion ratio is enough for the effective DRX in AZ80 alloy. The slightly coarser grain size at higher extrusion ratio could be due to a greater degree of heat generation during deformation and friction at higher extrusion ratio.

Table 5.5: The average grain sizes in AZ80 alloy extruded at various extrusion ratios and temperatures.

Temp. (°C)	*Average grain sizes, µm*		
	ER12	*ER22*	*ER44*
175	4 ± 2	4 ± 2	-
200	4 ± 2	4 ± 2	-
250	5 ± 2	-	6 ± 3
300	6 ± 3	-	7 ± 4
350	7 ± 3	-	8 ± 4

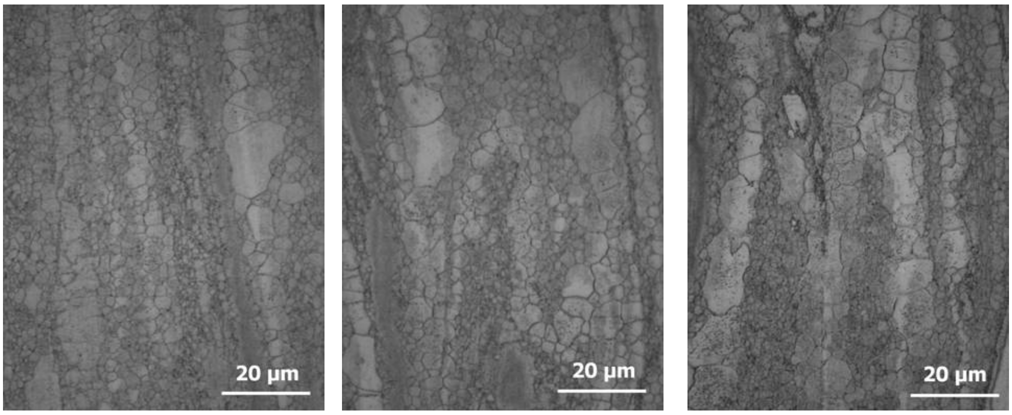

(a) ET 250 °C, ER 12 (b) ET 300 °C, ER 12 (c) ET 350 °C, ER 12

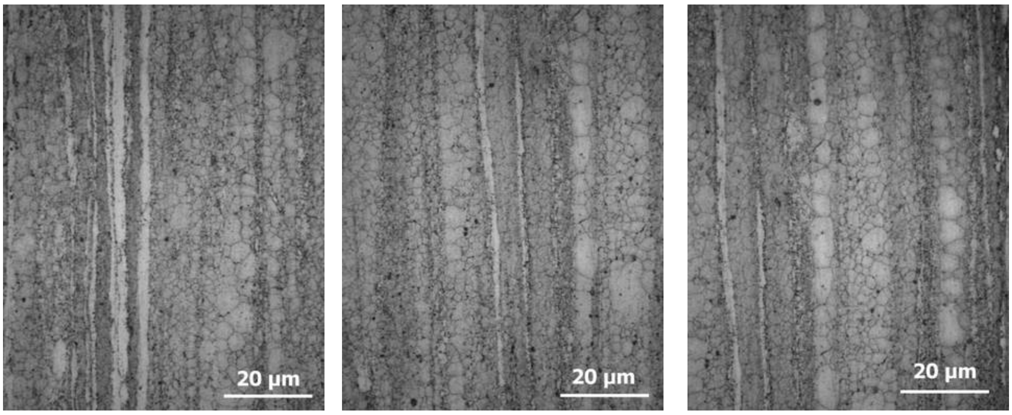

(d) ET 250 °C, ER 44 (e) ET 300 °C, ER 44 (f) ET 350 °C, ER 44

Figure 5.10: Optical microstructure of extruded alloys at various extrusion temperature (ET) and extrusion ratios (ER).

The optical micrographs after extrusion at various extrusion temperatures and both extrusion ratios are given in Fig. 5.10. The microstructures in all as-extruded conditions consist of recrystallized grains and elongated unrecrystallized regions. The recrystallized grains contain two populations of grain sizes. The size of coarse recrystallized grains is not much affected by the extrusion temperature, but their volume faction decrease with the lowering of extrusion temperature. However, the extrusion ratio significantly reduces the size of coarse grains from

10-20 μm at ER12 to 5-10 μm at ER44. The size of the fine recrystallized grains remains fairly constant (2-5 μm) at all the extrusion temperatures and ratios, but the volume fraction of fine grains increases at lower temperature and higher ratio.

5.1.5 Effect of pre-extrusion homogenization treatment

The optical and backscattered electron micrographs of AZ80 alloy extruded with and without prior homogenization heat treatment are presented in Fig. 5.11. Both extrusions were done at an extrusion temperature of 200 °C using a die having an exit diameter of 20 mm (i.e. ER12). The homogenization treatment dissolves some of β-phase constituents in AZ80 alloy (Fig. 5.4); therefore, a comparison of backscattered electron images shows fewer bands of β-phase stringers in the case of pre-extrusion homogenization (Fig. 5.11c). The optical micrographs show a fairly same recrystallized grain size, except for few regions where a localized grain growth occurs in the absence of β-phase.

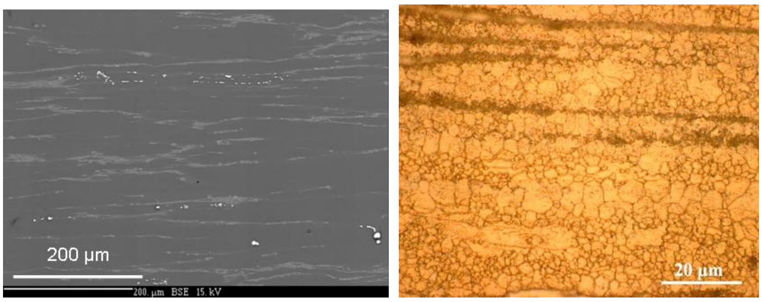

(a) no prior homogenization (b) no prior homogenization

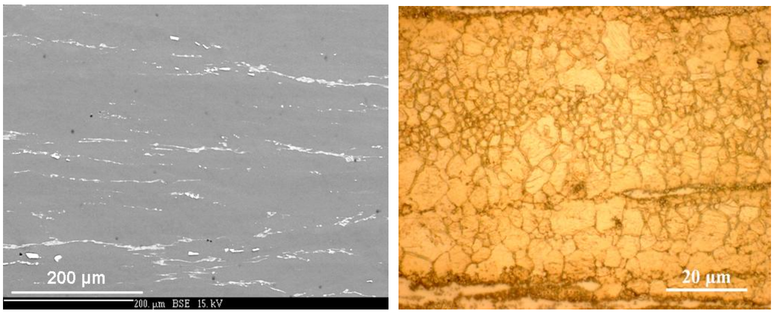

(c) with prior homogenization (d) with prior homogenization

Figure 5.11: Microstructures of ZK60 alloys extruded with and without prior homogenization treatment.

The optical and backscattered electron micrographs of ZK60 alloy extruded with and without prior homogenization heat treatment are presented in Fig. 5.12. Both extrusions were done at the extrusion temperature 250 °C using a die having an exit diameter of 20 mm (i.e. ER12). The homogenization treatment at 400 °C for 10 h completely dissolves all the Mg-Zn eutectic phase constituents in ZK60 alloy (Fig. 5.5c); consequently, a comparison of backscattered electron images shows absence of eutectic phase stringers in the case of pre-extrusion homogenization (Fig. 5.12c). The optical micrographs show that pre-extrusion homogenization treatment has a significant effect on the DRX response and grain size. A higher degree of DRX and subsequent secondary recrystallization profoundly reduces the fraction of unrecrystallized regions and results in recrystallized grains coarsening.

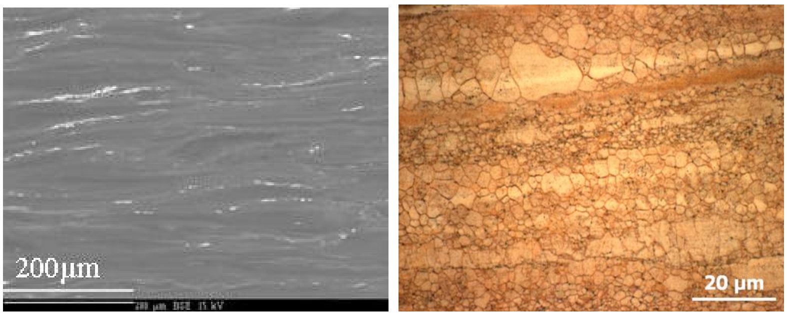

(a) no prior homogenization (b) no prior homogenization

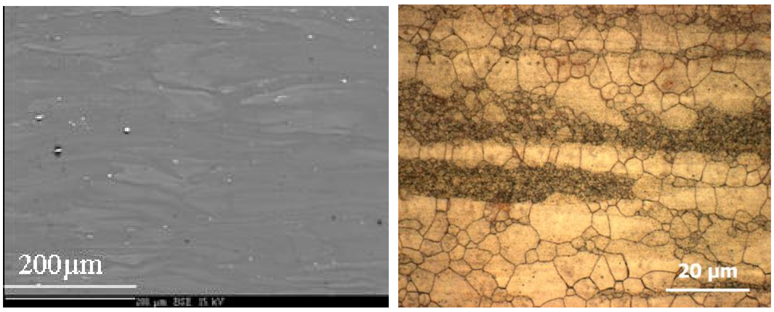

(c) with prior homogenization (d) with prior homogenization

Figure 5.12: Microstructures of ZK60 alloys extruded with and without prior homogenization treatment.

5.1.6 Effect of post-extrusion annealing

The optical microstructures before and after post-extrusion annealing heat treatments are shown in Fig. 5.13. The annealing treatments were performed at two temperatures 300 °C and 400 °C for a duration of 0.5 h each. The results show that as-extruded microstructure is quite stable at 300 °C; apart from localized grain growth at precipitate free regions, the microstructure is not much changed (Fig. 5.13b). In contrast, significant grain coarsening occurs during homogenization treatment at 400 °C and some of the β-phase stringers are dissolved (Fig. 5.13c).

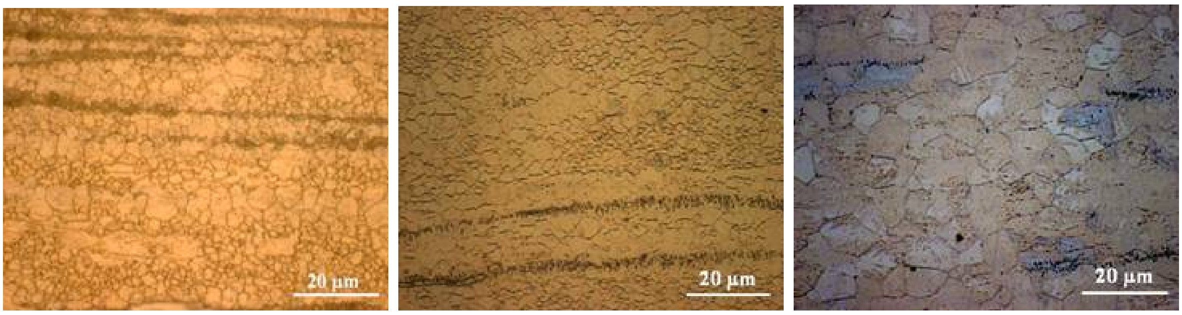

(a) As-extruded (b) PEA at 300 °C (c) PEA at 400 °C

Figure 5.13: Microstructural changes due to post-extrusion annealing (PEA) treatments for 0.5 h in AZ80 alloy

5.1.7 Effect of post-extrusion swaging

The optical microstructures in as-extruded and after post-extrusion swaging are presented in Fig. 5.14 for both AZ80 and ZK60 alloys. The swaging was performed at 300 °C. The as-extruded diameter of 20 mm was progressively reduced to 10 mm, in four passes having fairly equal degree of deformation per pass. The total degree of deformation corresponds to $\varphi = 1.4$. The microstructure in AZ80 alloy after post-extrusion swaging consists of recrystallized grains which are partly elongated in the extrusion direction, indicating some degree of strain hardening. In ZK60, the microstructure after post-extrusion swaging (Fig. 5.14d) is only partially recrystallized and the large unrecrystallized regions present in the as-extruded condition (Fig. 5.8a) are not visible. This indicates that although the temperature was high enough for DRX but the strain rate was lower than the critical value required for recrystallization. On the other hand, the same strain rate was above the critical value for AZ80 alloy.

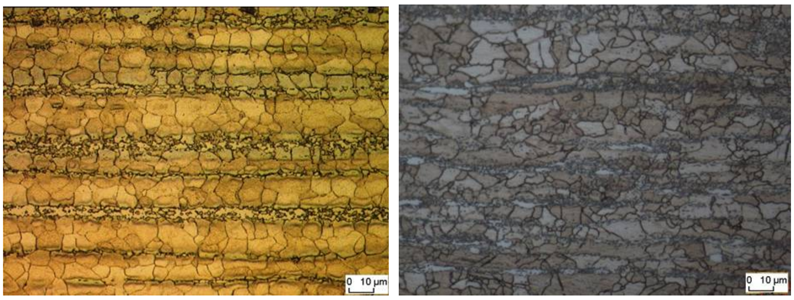

(a) AZ80 as-extruded (b) AZ80 as-swaged

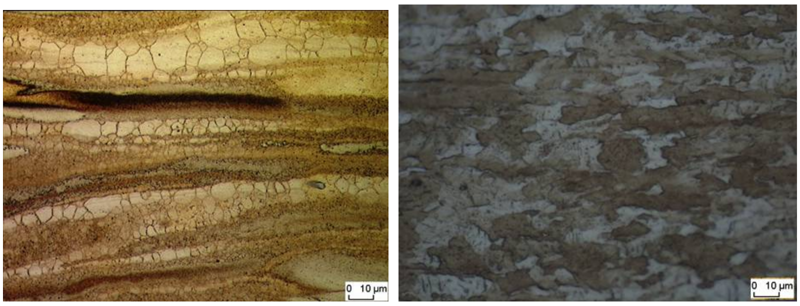

(c) ZK60 as-extruded (d) ZK60 as-swaged

Figure 5.14: Microstructures of AZ80 and ZK60 alloys before and after swaging treatment

5.2 Effects of extrusion parameters on texture development

5.2.1 Texture in as-cast condition

The crystallographic textures of as-cast AZ80 and ZK60 alloys are shown in Fig. 5.15 in form of (0002) pole figures. As seen in the Fig. 5.1, the grain size in as-cast condition is rather coarse ($\sim 100\ \mu$m) for texture determination by X-ray. The as-measured pole figures were determined in oscillating mode (an oscillation of 1 mm) for both alloys. The pole figures show random textures in both alloys, which is as to expect in as-cast condition.

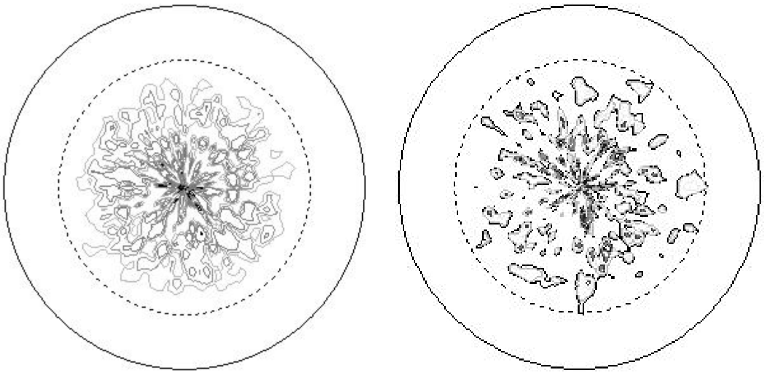
(a) AZ80 (b) ZK60

Figure 5.15: Experimental (0002) pole figures of the as-cast Mg alloys

5.2.2 Texture development during extrusion

The crystallographic texture of AZ80 and ZK60 alloys extruded at 300 °C is presented in form of calculated X-ray pole figures of three important planes in Fig. 5.16 and Fig. 5.17, respectively. The reference extrusion direction lies in the paper plane i.e (ND). Both alloys show fibrous texture in the extrusion direction. The results show that the basal plane has maximum pole intensity at 90° to the extrusion direction in both extruded alloys (Fig. 5.16a and Fig. 5.17a), while the $\{10\bar{1}0\}$ and $\{11\bar{2}0\}$ prismatic planes show maximum pole intensity in the extrusion direction, *i.e.* at 0° on the pole figures (Fig. 5.16b,c and Fig. 5.17b,c).

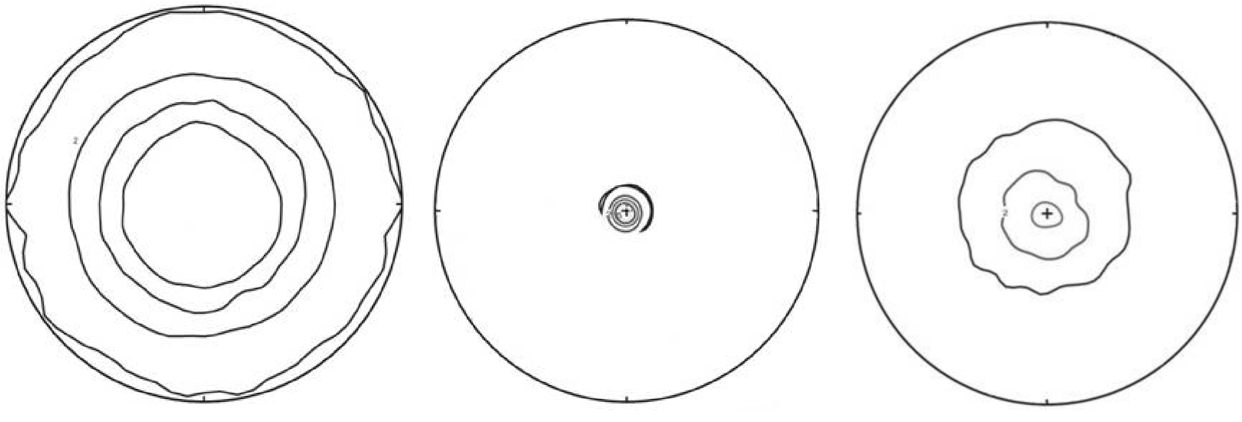

(a) (0002) pole intensity (b) $\{10\bar{1}0\}$ pole intensity (c) $\{11\bar{2}0\}$ pole intensity

Figure 5.16: XRD pole intensities of AZ80 alloy extruded at various temperatures and ratios.

Extrusion of magnesium alloys involves deformation and dynamic recrystallization of the original grains. The crystallographic texture after extrusion contains components from both these processes. Because of the closed packed hexagonal (CPH) lattice having an axial ratio of 1.624, the inter-atomic distance is shortest in $\langle a \rangle$ direction of the CPH lattice. Therefore, except for the deformation twinning and the slip with $\langle c + a \rangle$ burgers vector, all other deformation modes impart deformation along $\langle a \rangle$ direction of the CPH lattice in Mg alloys. This fairly uni-directional deformation in Mg alloys results in a fibrous type deformation texture in the extrusion direction, in which the basal plane containing the $\langle a \rangle$ direction is aligned in the extrusion direction, i.e basal plane normal is perpendicular to the extrusion direction. The recrystallization texture in Mg alloys is not much different from the deformation texture, some of the grains rotate around c-axis by 30° during recrystallization however, the angle of c-axis with respect to deformation direction does not change [89]. Thus, recrystallization does not effect the orientation of the basal planes but weakens the intensity of $\{10\bar{1}0\}$ plane in the extrusion direction.

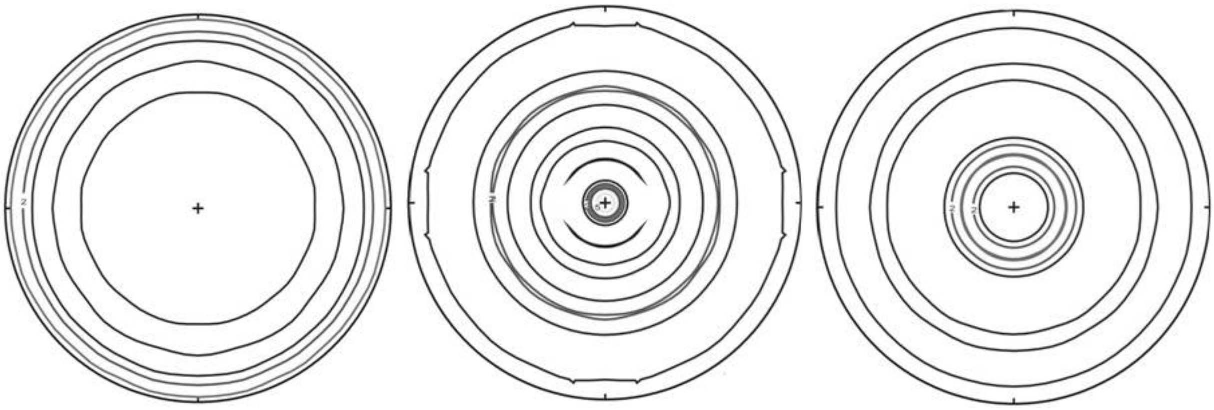

(a) (0002) pole figure (b) $\{10\bar{1}0\}$ pole figure (c) $\{11\bar{2}0\}$ pole figure

Figure 5.17: Pole figures of the as-extruded ZK60 alloy

A comparison of the pole figure of extruded AZ80 (Fig. 5.16) and ZK60 (Fig. 5.17) alloys shows that texture intensity of $\{10\bar{1}0\}$ plane is higher in ZK60 alloy than in AZ80 alloy, while the pole intensities of (0001) and $\{11\bar{2}0\}$ planes are only slightly different. As discussed earlier, intensity of the $\{10\bar{1}0\}$ plane indicates the degree of dynamic recrystallization during deformation. Thus, a higher $\{10\bar{1}0\}$ pole intensity in the case of extruded ZK60 alloy indicates a lower degree of DRX, which has also been confirmed in the microstructure analysis (Fig. 5.8).

5.2.3 Effect of extrusion temperature and ratio on texture development

As discussed in the earlier section 5.2.2, extrusion leads to a fibrous type texture in which the basal plane is aligned in the extrusion direction, *i.e.* basal plane normal is perpendicular to the extrusion direction. Extrusion temperature and ratio effect the relative contribution of $\langle c + a \rangle$ slip and deformation twinning, and thereby the crystallographic texture. The effect of extrusion temperature on X-ray pole intensities of various planes in AZ80 and ZK60 alloys is presented in Figs. 5.18 and 5.19. In general, the results show that extrusion temperature does not have any significant effect on the pole intensities, and a higher extrusion ratio gives a weaker $\{10\bar{1}0\}$ pole intensity in the extrusion direction, while the pole intensities of (0001) and $\{11\bar{2}0\}$ planes are not much affected.

Extrusion temperature affects the relative contribution of various slip systems to the total strain. As the extrusion temperature rises, other slip systems in addition to the basal slip and deformation twinning, which are the dominant deformation modes at low temperatures, are activated. However, except for the $\langle c + a \rangle$ pyramidal slip, all other slip systems result in the similar deformation texture, i.e basal plane normal is oriented perpendicular to the extrusion direction.

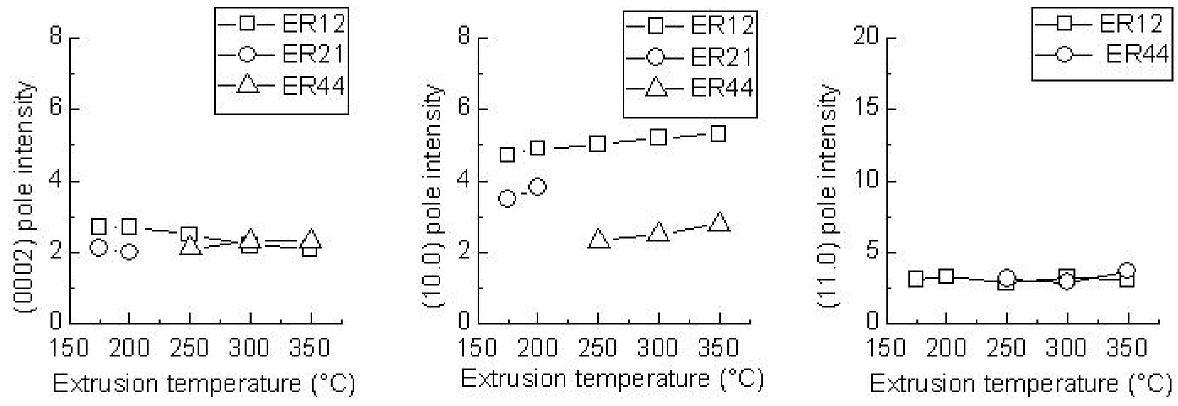

(a) (0002) pole intensity (b) $\{10\bar{1}0\}$ pole intensity (c) $\{11\bar{2}0\}$ pole intensity

Figure 5.18: XRD pole intensities of AZ80 alloy extruded at various temperatures and ratios.

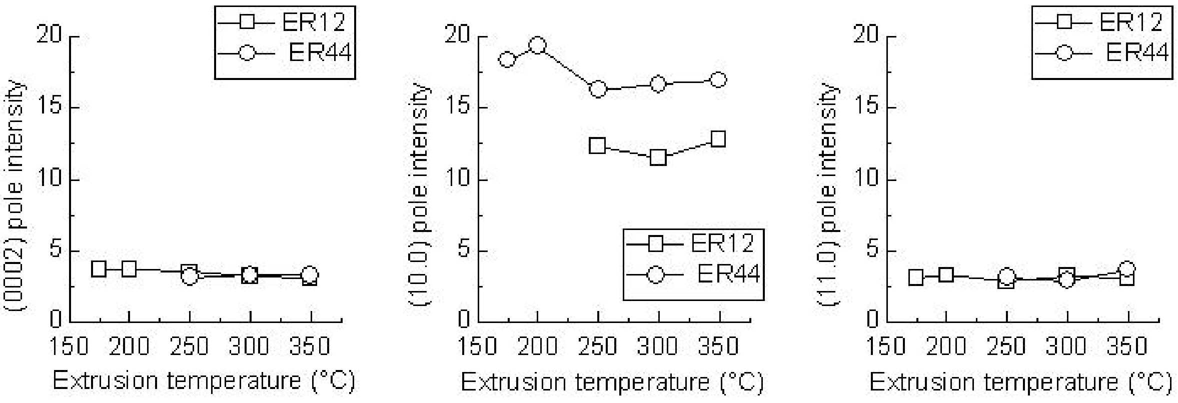

(a) (0002) pole intensity, Max. = 5 at 0 (b) $\{10\bar{1}0\}$ pole intensity (c) $\{11\bar{2}0\}$ pole intensity

Figure 5.19: XRD pole intensities of ZK60 alloy extruded at various temperatures and ratios.

5.2.4 Effect of pre-extrusion homogenization

The crystallographic textures of AZ80 and ZK60 alloys extruded with and without prior homogenization treatment are illustrated in Fig. 5.20 in the form of pole intensities of (0002) basal plane, $\{10\bar{1}0\}$ prismatic plane and $\{11\bar{2}0\}$ prismatic plane. The results show that the pre-extrusion homogenization treatment lowers the maximum pole intensity of $\{10\bar{1}0\}$ prismatic plane, whereas the pole intensity of other planes is not much affected. On average, the pole intensities of $\{10\bar{1}0\}$ prismatic plane are reduced by 50% in both alloys. As discussed in section 5.2.2, this lowering indicates a higher degree of recrystallization similar to what is observed at higher extrusion ratio (Fig. 5.18) and after post-extrusion annealing (Fig. 5.21).

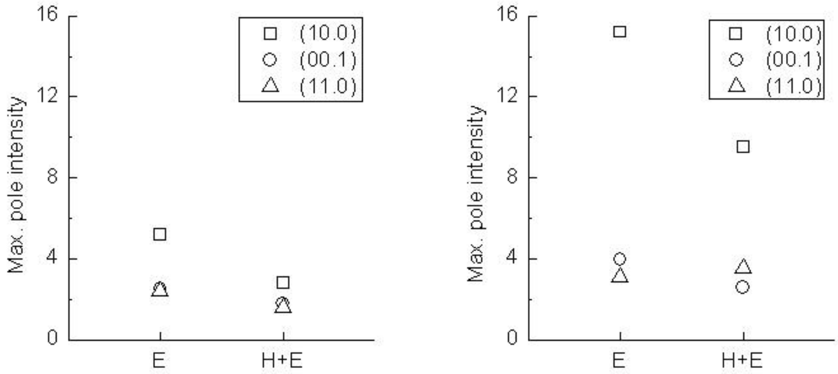

(a) AZ80 (b) ZK60

Figure 5.20: Maximum XRD pole intensities of various planes in Mg alloys extruded with (H+E) and without (E) prior homogenization treatment.

5.2.5 Effect of post-extrusion annealing

The X-ray pole intensities of basal plane (0001), prismatic plane $\{10\bar{1}0\}$ and prismatic plane $\{11\bar{2}0\}$ in conditions as-extruded and after post-extrusion are shown in Fig. 5.21. The results show that post extrusion annealing treatments lower the intensity of $\{10\bar{1}0\}$ pole in the extrusion direction, whereas the pole intensities of (0001) and $\{11\bar{2}0\}$ planes are not much affected. Fig. 5.21 shows that post-extrusion annealing at 300 °C only slightly lowers the intensity of $\{10\bar{1}0\}$ plane; while, the texture is almost randomized after the post-extrusion annealing at 400 °C. This result complements the microstructural results (Fig. 5.13) which show that the as-extruded microstructure is stable at 300 °C, but undergoes significant secondary recrystallization during post-extrusion annealing at 400 °C.

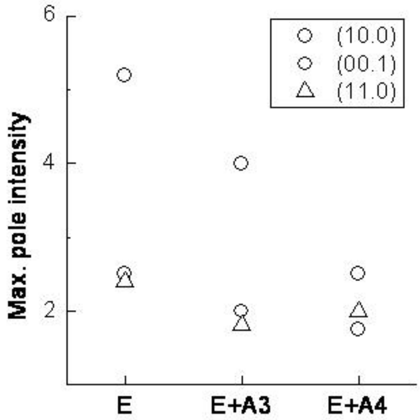

Figure 5.21: Maximum XRD pole intensities at as-extruded and post-extrusion annealed conditions in AZ80 alloy. E+A3 and E+A4 denote that post extrusion annealing was done at 300 °C and 400 °C, respectively.

5.2.6 Effect of post-extrusion swaging

Like extrusion with round profile discussed in section 5.2.2, rotary swaging is also a unidirectional deformation process. Therefore, the fiber texture attained after extrusion is only quantitatively affected by the swaging treatment, in which the maximum pole intensity of $(10\bar{1}0)$ plane increases. A comparison of three important pole intensities before and after the swaging treatment is given in Fig. 5.22. The figure shows that in both alloys, the post-extrusion swaging increases the texture intensity of prismatic plane $\{1\bar{1}0\}$, while the texture intensities of basal plane (0001) and prismatic plane $\{11\bar{2}0\}$ do not change. This result is in accord with earlier observation that the extrusion ratio and the temperature only change the texture intensity of prismatic plane $\{1\bar{1}0\}$, and only the texture intensities of basal plane (0001) and prismatic plane $\{11\bar{2}0\}$ are changed.

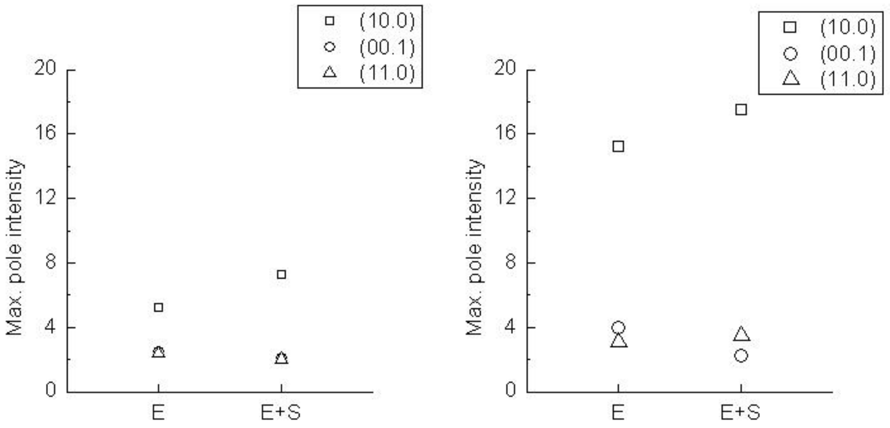

(a) AZ80 (b) ZK60

Figure 5.22: Maximum XRD pole intensities of various planes in Mg alloys in as extruded (E) and extruded plus swagend (E+S) conditions.

5.3 Effect of extrusion parameters on tensile and compressive properties

5.3.1 Tensile and compressive properties in as-cast condition

The tensile and compressive properties of as-cast AZ80 and ZK60 alloys are shown in Fig. 5.23 in two perpendicular directions (L) and (D). In comparison to AZ80 alloy, the ZK60 alloy shows higher yield stress, tensile strength and ductility. The higher strength in ZK60 alloy is attributed to the a higher degree of solid solution strengthening [90] and precipitation hardening caused by Zn-Zr intermetallic particles (Fig. 5.1b). Both alloys show a compressive yield stress lower than the tensile yield stress, however the effect is more pronounced in ZK60 alloy. It is generally believed that in Mg alloys, deformation under compression starts with $(10\bar{1}\bar{2})$ twinning. By justifying and applying the CRSS criterion, a value of 65-75 MPa has been suggested for the activation of $(10\bar{1}\bar{2})$ tensile twins in an extruded Mg–7.7 at% Al alloy. In cast alloys having random texure, these twins are expected to be activated at about 100 MPa. Fig. 5.23 shows that inspite of a higher tensile yield stress (TYS), the compressive yield stress (CYS) in ZK60 alloy is fairly similar to that of AZ80 alloy. Thus, a larger difference in TYS and CYS is observed in ZK60 alloy.

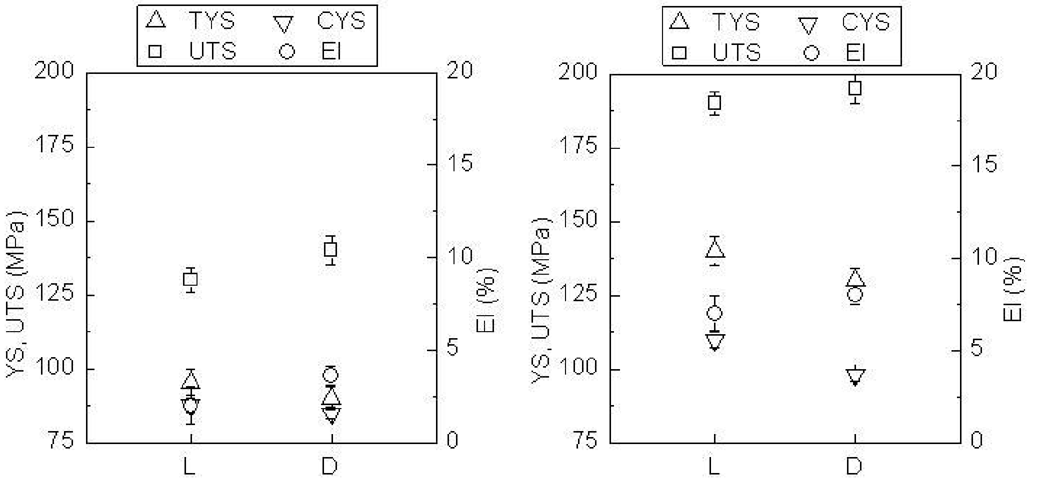

(a) AZ80 alloy (b) ZK60 alloy

Figure 5.23: Tensile and compressive properties of as-cast Mg alloys. Symbols L and D denote that specimens were prepared along length and diameter of the cylindrical cast billets, respectively.

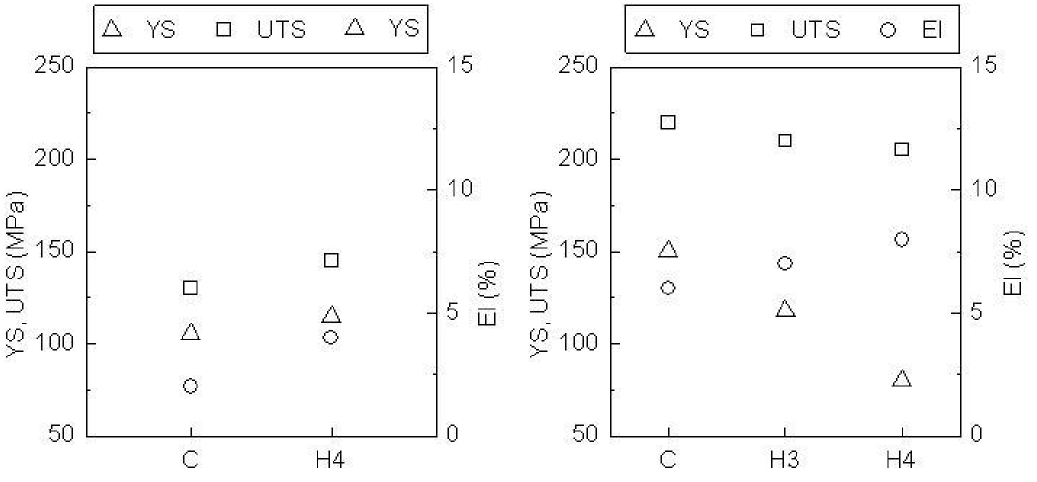

(a) AZ80 alloy (b) ZK60 alloy

Figure 5.24: Tensile and compressive properties of as-cast Mg alloys before and after homogenization treatment. The symbols C, H3 and H4 stand for as-cast, homogenized at 300 °C and homogenized at 400 °C, respectively.

5.3.2 Effect of homogenization treatment

The results of tensile and compression tests in as-cast and after homogenization treatment are presented in Fig. 5.24. Both AZ80 and ZK60 alloys were homogenized at 400 C for 10 h. The presented results show that the homogenization treatment at 400 °C leads to slight improvement in strength and ductility in AZ80 alloy; whereas, the same treatment leads to a lowering of strength in ZK60 alloy. In comparison, a homogenization treatment at 300 °C causes only little changes in strength.

A partial dissolution of eutectic constituents in AZ80 (c.f. Fig. 5.4) , and therefore the solid solution strengthening in adjacent regions increases the strength in AZ80 alloy after homogenization at 400 °C. In contrast, a complete dissolution of eutectic constituents in ZK60 alloy occurs at this temperature (c.f. Fig. 5.5b) causing a significant loss of strength. However, a partial dissolution of eutectic constituents during homogenization treatment at 300 °C in ZK60 alloy (Fig. 5.5b on page 33) does not lead to strength gains observed in AZ80 alloy. The contribution of precipitation hardening towards overall strength is therefore higher in ZK60 alloy than in AZ80 alloy.

5.3.3 Effect of extrusion temperature and ratio

The results of uni-axial tensile and compression tests in as-extruded conditions have been presented in Fig. 5.25. The results show a pronounced improvement in mechanical properties after extrusion, and the effects of extrusion ratio and temperature on quasi-static mechanical properties. As also observed earlier in the case of grain size (c.f. Table 5.5), extrusion ratio (ER) has only little effect on the yield stress in AZ80 alloy. The tensile elongation, however, is slightly improved with an increase of ER. At higher extrusion temperatures, ER 44 shows slightly higher ultimate tensile strength in comparison to ER12, but the difference decreases with the lowering of extrusion temperature. At lower temperatures of 200 °C and 175°C, almost similar values of the YS and UTS have been observed at both extrusion ratios i.e. ER12 and ER22. In general, the yield stress increases with the lowering of extrusion temperature. The UTS value also increases with the lowering of extrusion temperature in the case of ER12 and becomes equal to that of ER44 at temperatures 175-200 °C. The anisotropy of YS in tension and compression (strength differential effect) is also reduced with the lowering of extrusion temperature.

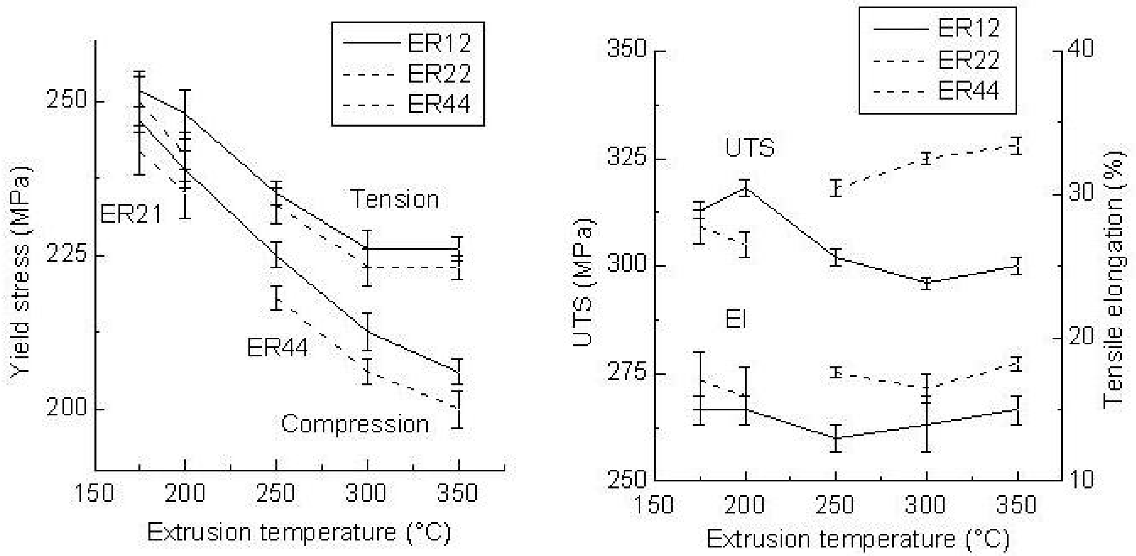

(a) TYS and CYS

(b) UTS and El

Figure 5.25: Mechanical properties of as-extruded AZ80 alloy at various extrusion temperatures and ratios

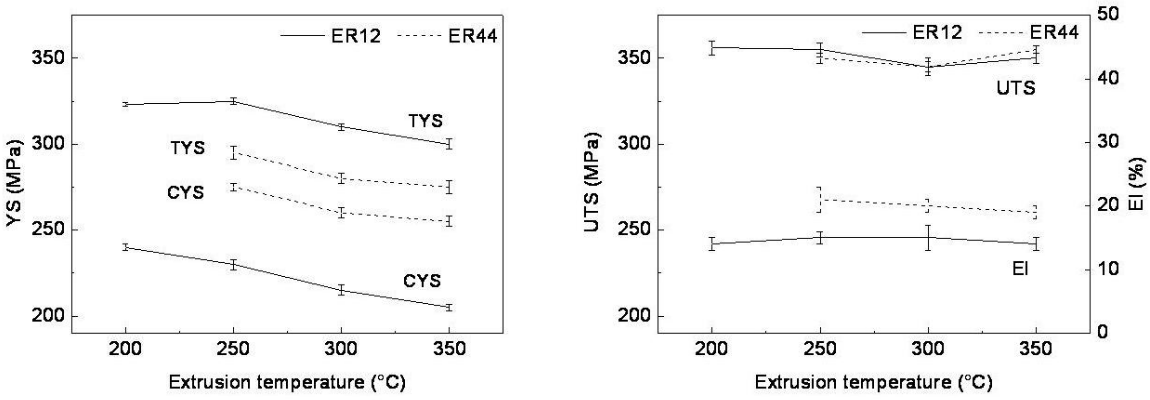

(a) TYS and CYS

(b) UTS and El

Figure 5.26: Mechanical properties of as-extruded ZK60 alloy at various extrusion temperatures and ratios

Fig. 5.26 shows the tensile and compressive properties of ZK60 alloy extruded at various temperature and two ratios. The results show no variation of YS with the changing extrusion temperature at both ratios, and a significantly higher (4 times higher) strength differential effect at lower extrusion ratio (ER12). Although, the microstructure at both extrusion ratios is inhomogeneous (Fig. 5.8 on page 35), there are fewer β-phase stringers and fewer coarse grains at higher extrusion ratio due to a higher degree of recrystallization. A higher strength differential is caused by a higher TYS and a lower CYS at ER12. In the case of lower extrusion ratio (ER12), the strain hardened β-phase stringers lead to an increase in TYS (about 25 MPa); while, the coarse grains make the twinning nucleation easier (the stress required for twin nucleation decreases in coarse grains, because of the lowering of surface to volume ratio) and thus a lower CYS (about 50 MPa) is observed. As observed in AZ80 alloy, the higher extrusion ratio (ER44) results in a higher tensile elongation.

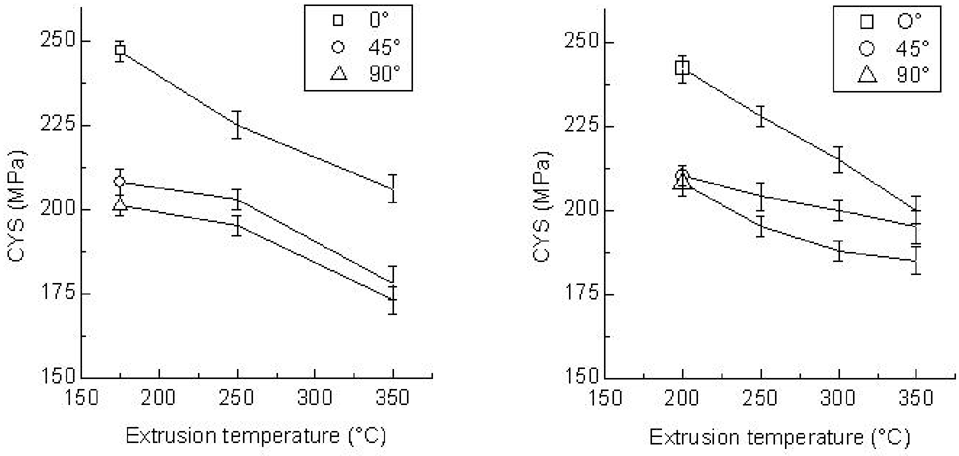

(a) Directional variation of CYS

(b) Directional variation of CYS

Figure 5.27: Mechanical properties of as-extruded AZ80 alloy at various extrusion temperatures and ratios

Fig. 5.27 shows the directional anisotropy in compressive yield stress in extruded AZ80 and ZK60 alloys. Due to the basal crystallographic texture, the deformation starts with basal slip in longitudinal tension and with deformation twinning in longitudinal compression, this results in strength differential effect. In other directions i.e. 45° and 90° to the extrusion direction, a higher Schmidt factor favors the basal slip and thus a lower CYS is observed. The results in Fig. 5.27b show, that directional activation of the tensile twins causes a difference of $\sim$ 25 MPa in the observed CYS. This is equal to the difference between the longitudinal TYS and CYS caused by the crystallographic texture at an higher extrusion ratio. This result further reinforces the notion that four times larger difference between longitudinal TYS and longitudinal CYS observed in the case of lower extrusion ratio can not be due to the texture and thus is likely to be caused by the large unrecrystallized grains.

5.3.4 Effect of pre-extrusion homogenization treatment

The tensile and compressive properties of AZ80 and ZK60 alloys extruded with and without homogenization treatment are presented in Fig. 5.28. The homogenization treatment was carried out at 400 °C for both alloys. The results indicated that pre-extrusion homogenization leads to increases in YS, UTS and El. in AZ80 alloy. However, the same treatment lowers the YS and UTS in ZK60 alloy with accompanying increse in El. The presented results also show that the pre-extrusion homogenization removes the strength differential effect in AZ80 alloy and reduces its impact in ZK60 alloy. A comparison of the microstructures (Fig. 5.11) shows that the microstructure of extruded AZ80 alloy is not much affected by prior homogenization treatment. A slight increase in YS and UTS is attributed to the partial dissolution of eutectic phase $Mg_{17}Al_{12}$ and therefore, the solid solution strengthening caused by the liberated Al. In comparison, the grain size in the pre-extrusion homogenized ZK60 alloy is significantly coarser than the one extruded without homogenization (Fig. 5.12), which leads to the lowering of the strength. The weakening of crystallographic texture with pre-extrusion homogenization in both alloys (Fig. 5.20 on page 44) reduces the anisotropy in YS under tensile and compressive loading.

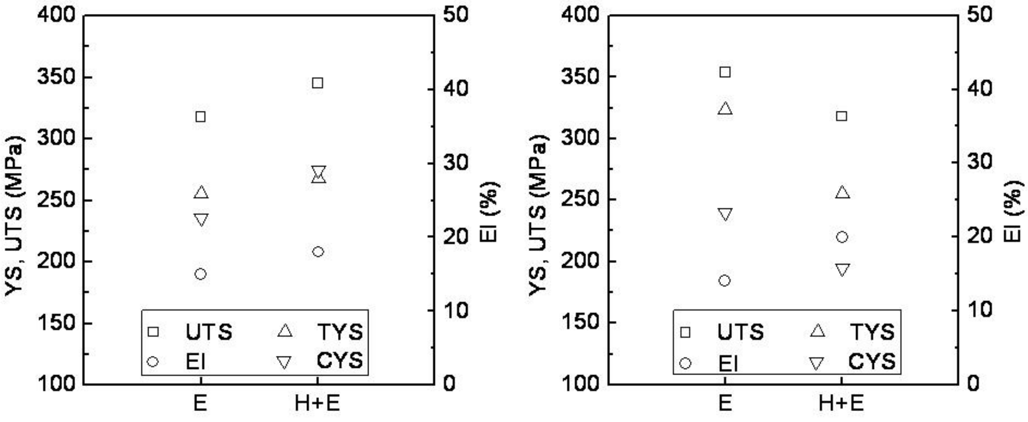

(a) AZ80 alloy (b) ZK60 alloy

Figure 5.28: Tensile and compressive properties of Mg alloys extruded with and without prior homogenization treatment.

5.3.5 Effect of post-extrusion annealing

The tensile and compressive properties of the AZ80 alloy before and after the post-extrusion annealing treatment (PEAT) are in Fig. 5.29a. The results show that the choice of post-extrusion annealing temperature has significant effect on mechanical properties. In case of PEAT at 300 °C, the mechanical properties are only slightly affected. However, PEAT at 400 °C significantly lowers the yield stress ($\sim$ 75 MPa) with an accompanying increase in tensile elongation ($\sim$ 66 %). This shows that as-extruded microstructure is stable at 300 °C and retains high strength achieved after extrusion. However, PEAT at 400 °C leads to dissolution of β-phase and significant grain coarsening (Fig. 5.13c) resulting in loss of the yield stress. Fig. 5.29b shows the effect of post-extrusion annealing treatment on compressive yield stress in longitudinal and transverse directions. In addition, the TYS values in longitudinal direction have also been plotted to show the strength differential effect. The results show that PEAT at 400 °C alomost eliminates the anisotropy in the yield stress, whereas, the PEAT at 300 °C has no significant effect. These results can be explained of crystallographic texture results (c.f. Fig. 5.21). A fairly random texture after PEAT at 400 °C eliminates the anisotropy in the YS. In comparison, the basal texture observed after extrusion is only partially weakened after PEAT at 300 °C. As a result, the degree of anisotropy in YS is also only partially reduced.

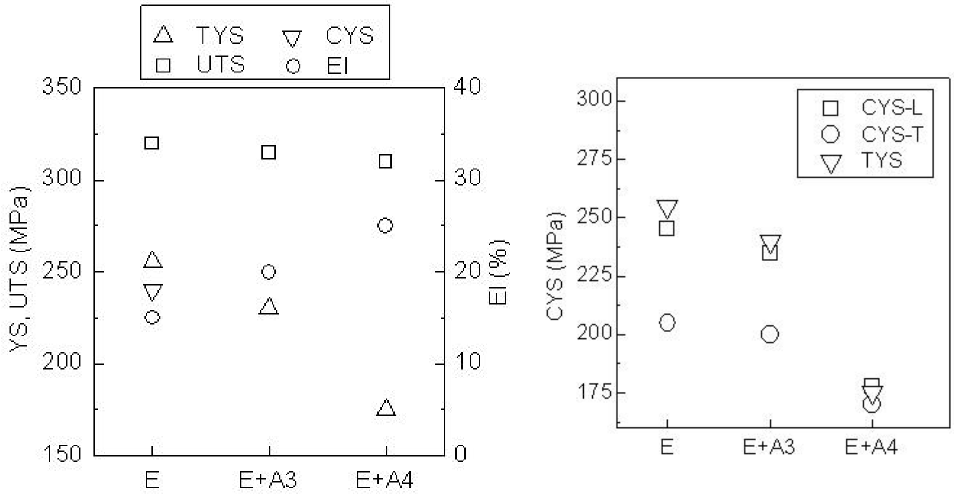

(a) Tensile and compressive properties

(b) Anisotrpy in YS

Figure 5.29: Tensile and compressive properties of AZ80 alloy before and after post extrusion annealing treatment

5.3.6 Effect of post-extrusion swaging

The tensile and compressive properties of alloys AZ80 and ZK60 before and after the swaging treatment are shown in Fig. 5.30. The figure shows that swaging increases the YS and UTS in both alloys and lowers the tensile ductility. The micro-structural studies in as-extruded and post-extrusion swaged alloys (Fig. 5.14, 40) show similar recrystallized microstructure in AZ80 alloy, with some grains elongated in the swaging direction indicating some degree of work hardening. The little difference between the TYS and UTS values after swaging (25 MPa) compared to the same in as-extruded condition (75 MPa) corroborates this observation. Therefore, strain hardening in addition to the so called texture strengthening caused by the stronger basal texture (Fig. 5.22, 45) are responsible for the increase in strength after swaging.

In ZK60 alloy, the microstructure after swaging indicates poor DRX during swaging (Fig. 5.14, 40). This implies that the deformation conditions (strain rate and temperature) which resulted in an effective DRX response in AZ80 alloy were below the critical conditions required in ZK60 alloy. This result is consistent with the as-extruded results, which also indicate the poor DRX in ZK60 alloy after the same deformation conditions (c.f. Figs. 5.7 and 5.8). Therefore, significant increase in YS and UTS in ZK60 alloy after swaging treatment can be attributed to the strain hardened unrecrystallized grains and strong basal texture (Fig. 5.22).

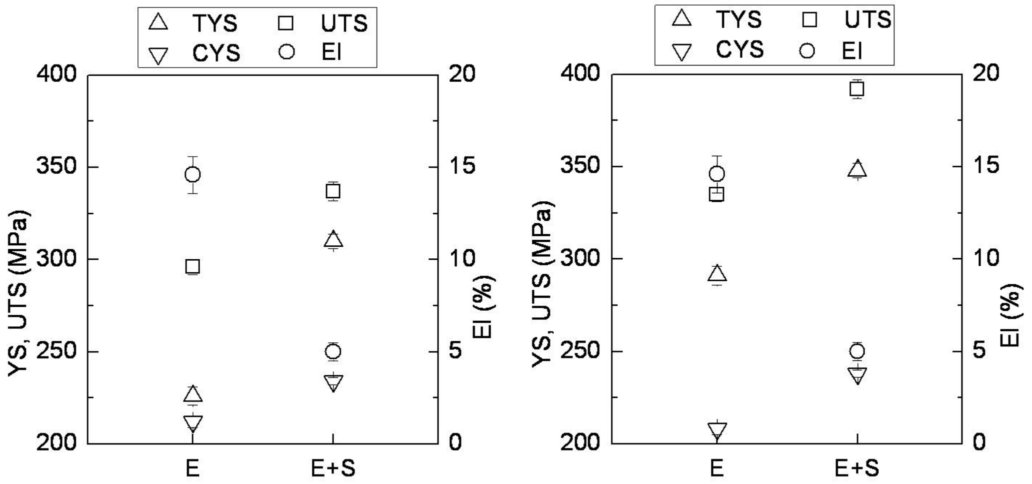

(a) AZ80 alloy (b) ZK60 alloy

Figure 5.30: Tensile and compressive properties of AZ80 alloy before and after post extrusion annealing treatment

5.4 Effect of extrusion parameters on tensile properties at elevated temperature

5.4.1 Tensile properties at elevated temperature in as-cast condition

The flow curves of AZ80 and ZK60 alloys in as-cast condition at various temperatures are presented in Fig. 5.31. The results show that the flow stress at 200 °C is comparable to that of at the room temperature in both alloys. At temperatures higher than 200 °C, the flow stress reduces in both AZ80 and ZK60 alloys, however, tenile elongation is not much affected. The flow stress at any strain is higher in ZK60 alloy at 200–250 °C. However, as the temperature increases, ZK60 alloy becomes easier to deform. This is due to the low melting point of the Mg-Zn eutectic ($\sim$ 350 °C), while, the Mg-Al eutectic $Mg_{17}Al_{12}$ has a higher melting point($\sim$ 435 °C). Therefore, at 350 °C, no deformation was possible in ZK60 alloy and the sample failed without any deformation due to the incipient melting of eutectic. On the other hand, due to the high melting point of Mg-Al eutectic ($Mg_{17}Al_{12}$), the AZ80 alloy shows maximum strain before fracture at 350 °C.

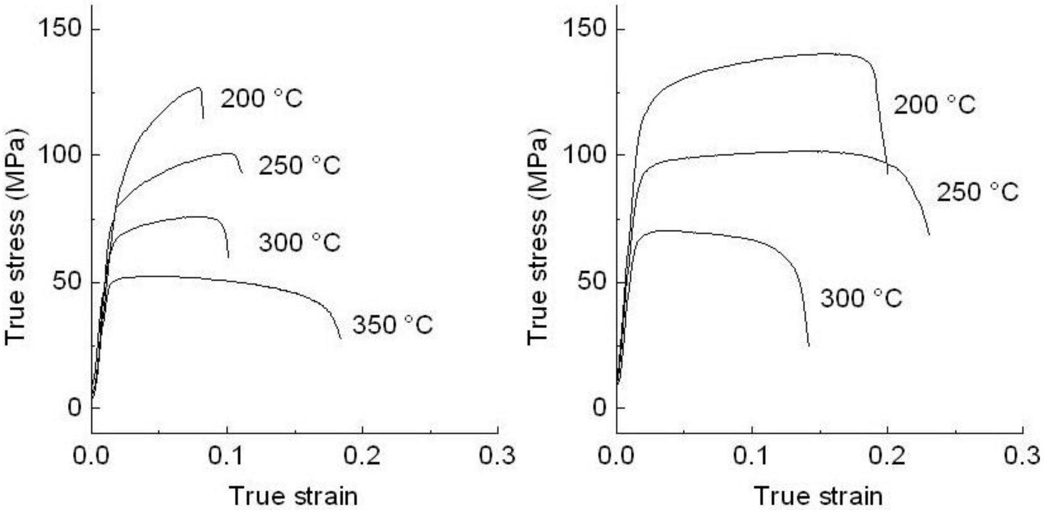

(a) AZ80 alloy (b) ZK60 alloy

Figure 5.31: Tensile flow curve of Mg alloys in as-cast condition

5.4.2 Effect of extrusion temperature on tensile properties at elevated temperature

The flow curves of AZ80 alloy extruded at 250 °C and 350 °C are presented in Fig. 5.32. The figure shows flow curves on a range of deformation temperatures 200-350 °C. The figure shows a superplastic deformation behavior at temperatures 250-350 °C.

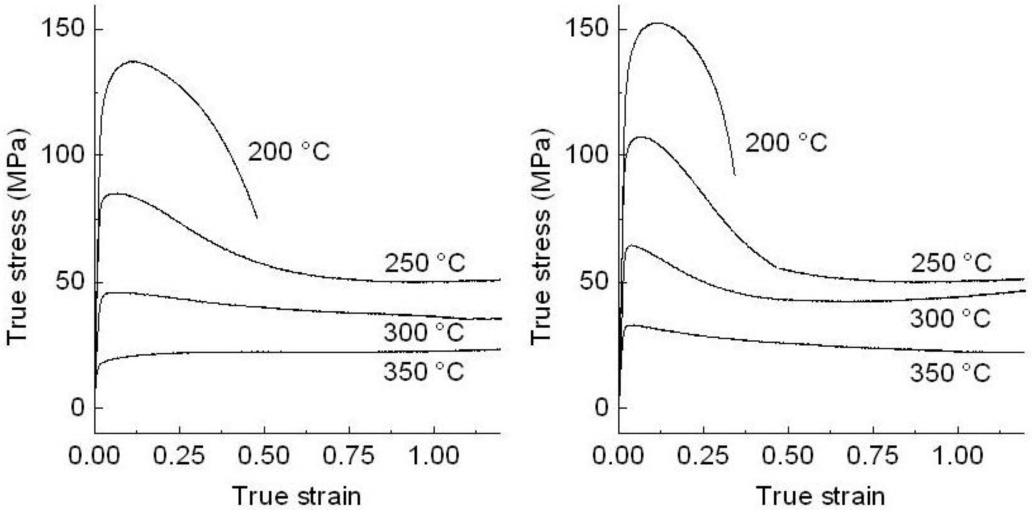

(a) Ex Temp. 250 °C (b) Ex Temp. 350 °C

Figure 5.32: Tensile flow curve of AZ80 alloy extruded at different temperatures

Both figures show a peak in flow stress after which it reduces sharply and subsequently remains fairly constant. The sharp decrease in flow stress is usually understood to be the onset of dynamic recrystallization [91]. A comparison of Fig. 5.32a and b shows that in case of higher extrusion temperature, the onset of DRX occurs at higher stress, indicating a higher degree of thermal stability of microstructure in case of the higher extrusion temperature. The figure also shows that the strain corresponding to the onset of DRX decreases with the increase in the temperature. Fig. 5.32b shows that at 300 °C, the flow stress increases slightly towards the end. This phenomenon has been reported in literature [92] and is observed at high strains and low temperatures.

The grain boundary sliding (GBS) mechanism is generally accredited as the main deformation mode responsible for the superplastic deformation behavior in fine grain Mg alloys. Since, not all the grain boundaries slide to same extent, therefore in order to maintain grains stability and avoid premature failure by extensive cavitation, it it is necessary that GBS is accompanied by another accommodating processes *e.g.* grain boundary migration, recrystallization, diffusional flow and dislocation creep [93]. In AZ61 alloy, it has been observed that the grain boundary sliding is accommodated by slip, which in turn is controlled by grain boundary diffusion at 523-573 K, and by lattice diffusion at 598-673 K.

The flow curves of ZK60 alloy extruded at 250 °C and 350 °C are presented in Fig. 5.33. The figure shows the flow curves in the range of 200-350 °C. Similar to earlier observation in AZ80 alloy, the figure shows a superplastic deformation behavior at temperatures 250-350 °C. Thus, regardless of other differences observed in microstructure development and consequent mechanical properties between AZ80 and ZK60 alloy, both alloys in as-extruded condition exhibit superplastic deformation behavior at same temperatures namely 250 °C (0.56 T_m). The flow curves in the ZK60 alloy show similar effects of extrusion temperature and testing temperature on the onset of DRX, as were observed in the AZ80 alloy (Fig. 5.32). Although, the yield stress at room temperature is higher in extruded ZK60 alloy than the one in extruded AZ80 alloy (compare Fig. 5.25 with Fig. 5.26), the flow stresses at elevated temperature, however, show opposite behavior. This is due to the difference in the main deformation mechanisms that operate at room temperature and at elevated temperatures. At low temperatures, the deformation is mainly slip controlled, whereas, at elevated temperatures, the grain boundary sliding is the main deformation mode.

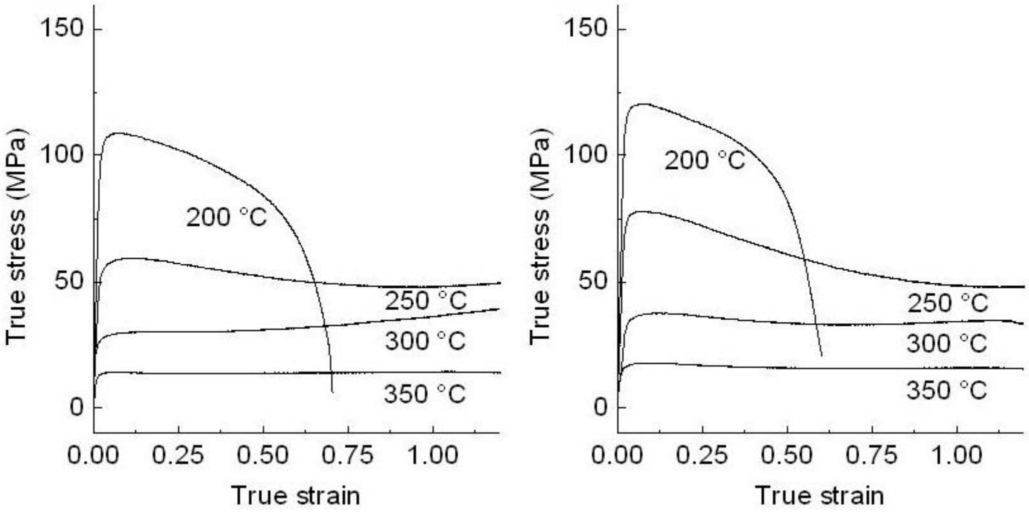

(a) Ex Temp. 250 °C (b) Ex Temp. 350 °C

Figure 5.33: Tensile flow curve of ZK60 alloy extruded at different temperatures

5.4.3 Effect of extrusion ratio on tensile properties at elevated temperatures

The flow stresses corresponding to strain of 0.1 and total tensile elongation before fracture at various testing temperatures in AZ80 and ZK60 alloys are shown in Fig. 5.34. The figure shows the behavior of alloys in as-cast, extruded at ER12 and extruded at ER44. The results show that both alloys in as-extruded conditions exhibit approximately the same flow stresses in as-cast and extruded conditions at testing temperatures higher than 200 °C, *i.e.* T> 0.5 T_m.

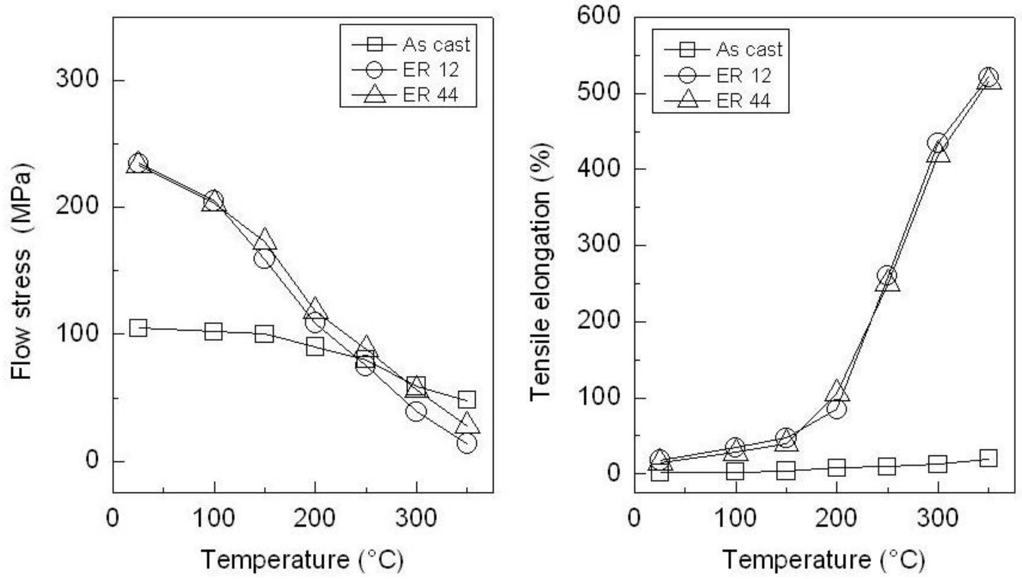

(a) AZ80 alloy (b) AZ80 alloy

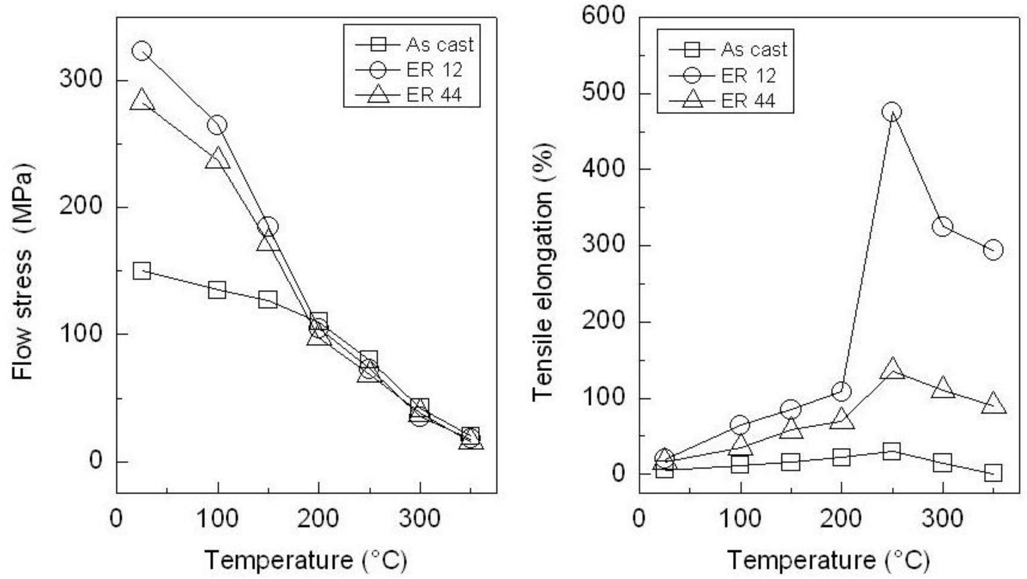

(c) ZK60 alloy (d) ZK60 alloy

Figure 5.34: Tensile flow curve of AZ80 alloy extruded at different temperatures

The extrusion ratio has no significant influence on tensile properties at elevated temperatures in AZ80 (Fig. 5.34a-b). In contrast, extrusion ratio affects the maximum tensile elongation before fracture (Fig. 5.34d), while, the flow stress is not affected (Fig. 5.34c). As discussed earlier, the superplastic behavior in as-extruded conditions is attributed to the grain boundary sliding, which in turn is result of fine grain size achieved after extrusion. In ZK60 alloy, the microstructure consists of large recrystallized grains and unrecrystallized regions (Fig. 5.8). The coarse grains, as in the as-cast condition, make the deformation inhomogeneous and cracks nucleate at grain boundaries leading to the early fracture. In contrast, AZ80 shows similar microstructure at both extrusion ratios (Fig. 5.7) and therefore similar tensile behavior at elevated temperatures is observed.

5.5 Effect of extrusion parameters on fatigue performance

5.5.1 Fatigue performance in as-cast condition

The results of rotating beam fatigue testing in as-cast condition are presented in Fig. 5.35a for both AZ80 and ZK60 alloys. The results show that cycles to failure reduce linearly with increasing stress amplitude in both alloys. Although, the cycles to failure at the same stress amplitude at higher in ZK60 alloy, both alloys show fatigue failure even at low stress amplitudes. The eutectic constituents at the grain boundaries ease the initiations of cracks which can grow to large sizes without being hindered due to the coarse grain sizes in as-cast condition (Fig. 5.1).

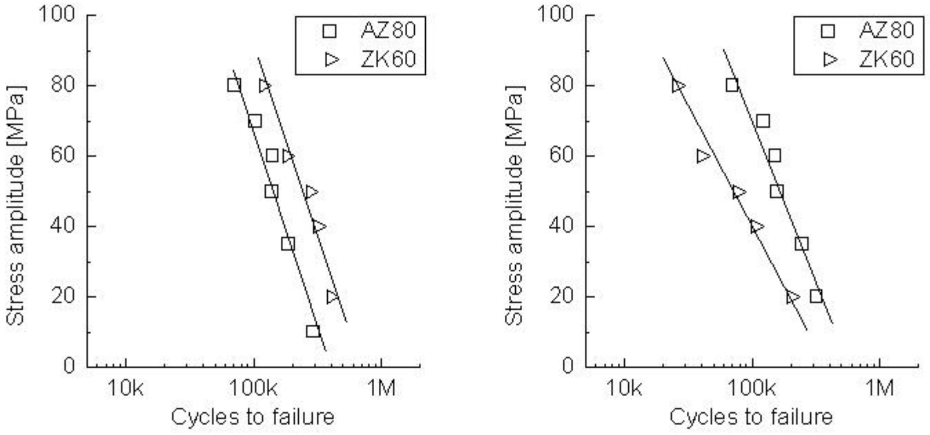

(a) As-cast condition (b) Homogenized condition (400 °C, 10 h)

Figure 5.35: Fatigue performance of as-cast Mg alloys before and after homogenization treatment

5.5.2 Effect of homogenization treatment on fatigue performance

The fatigue performance of as-cast AZ80 and ZK60 alloys after homogenization treatment at 400 C for 10 h is presented in Fig. 5.35b. The fatigue behavior after homogenization is not much different from that in the as-cast condition. The results show that cycles to failure reduce linearly with increasing stress amplitude in both alloys. At the same stress amplitude, the number of cycles before failure increase slightly in the AZ80 alloy, and decrease slightly in ZK60 alloy, because of the partial dissolution of eutectic constituents in the former case and complete dissolution of eutectic in the latter case.

5.5.3 Effect of extrusion temperature and ratio on fatigue performance

The fatigue performance of AZ80 and ZK60 alloys extruded at various temperatures is shown in Figs. 5.36 and 5.37, respectively. The SN curves were determined by rotating beam fatigue testing (R= -1) using hour glass fatigue specimens which were electropolished to remove a surface layer of 100 μm. In contrast to the fatigue behavior in as-cast condition (Fig. 5.35a), the SN curves of as-extruded alloys show quite high endurance limits (the stress amplitude corresponding to no failure after 10 million cycles) due to the significant grain refinement during extrusion and consequent high strength.

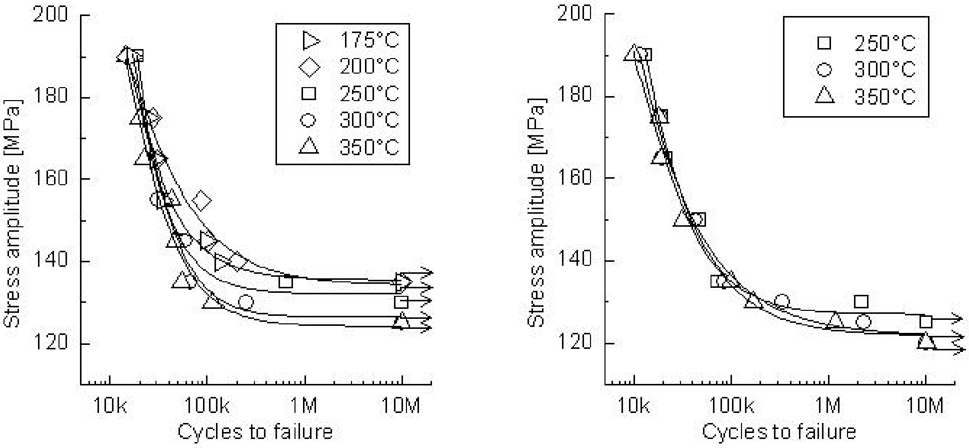

(a) ER12 (b) ER44

Figure 5.36: Fatigue performance of AZ80 alloy extruded at various temperatures

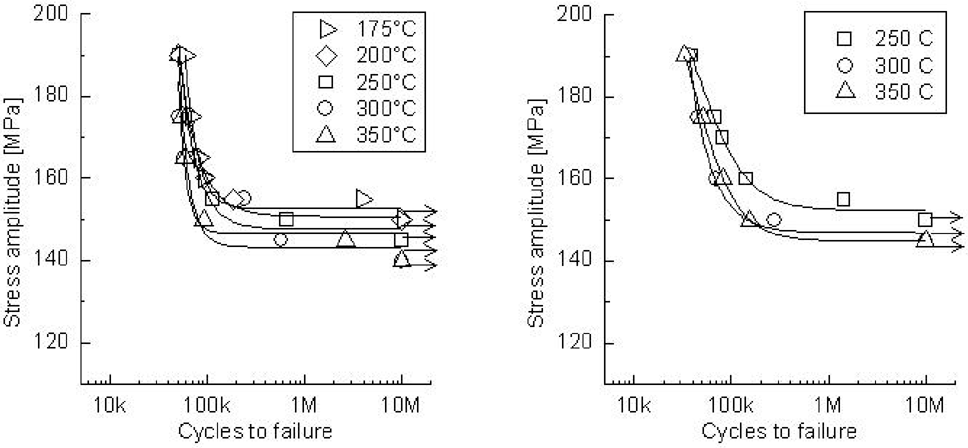

(a) ER12 (b) ER44

Figure 5.37: Fatigue performance of ZK60 alloy extruded at various temperatures

The results presented in Fig. 5.36 show that the endurance limit of AZ80 alloy is affected neither by extrusion temperature nor by extrusion ratio. The results of uni-axial testing AZ80 alloy (Fig. 5.25,page 47) show an improvement of 25 MPa and 50 MPa in TYS and CYS, respectively, while, the two extrusion ratios show similar values of YS. Accordingly, the fatigue performance is slightly improved with the lowering of extrusion temperature, especially at lower temperatures 175 – 200 °C. However, the high cycle fatigue performance at two extrusion ratios is similar. The SN curves of the ZK60 alloy extruded at various temperatures and two ratios are presented in Fig. 5.37. Similar to AZ80 alloy, the results show some improvement in endurance limit with the lowering of extrusion temperature at low temperatures, and similar fatigue response at both extrusion ratios. In general, the endurance limit of extruded ZK60 alloys is higher than that in the extruded AZ80 alloys, because of the higher strength (Fig. 5.25 with Fig. 5.26). However, despite the higher TYS at lower extrusion ratio (ER12), the fatigue behavior is not so different at both extrusion ratios. This result implies that the increase in TYS caused by the strain hardened unrecrystallized regions (Fig. 5.8) has no effect on fatigue behavior.

5.5.4 Effect of pre-extrusion homogenization treatment on fatigue performance

The fatigue behavior of the AZ80 and ZK60 alloys extruded with and without prior homogenization treatment is presented in Fig. 5.38. The pre-extrusion homogenization treatment was performed at 400 °C for 10 h. The results show that pre-extrusion homogenization leads to no change in the endurance limit of AZ80 alloy, while, the same lowers the endurance limit in ZK60 alloys. A partial dissolution of eutectic phase during the homogenization treatment (Fig. 5.4) (thus some solid solution strengthening) and similar grain sizes upon extrusion (Fig. 5.11) give a slightly higher strength in pre-extrusion homogenized AZ80 alloy (Fig. 5.28). The fatigue behavior is, therfore, not effected. In contrast, a complete dissolution of eutectic phase during homogenization treatment (Fig. 5.5 on page 33) and significant grain coarsening in extruded condition (Fig. 5.12 on page 39) results in a lowering of tensile strength (Fig. 5.28 on page 49) and fatigue endurance limit in pre-extrusion homogenized ZK60 alloy.

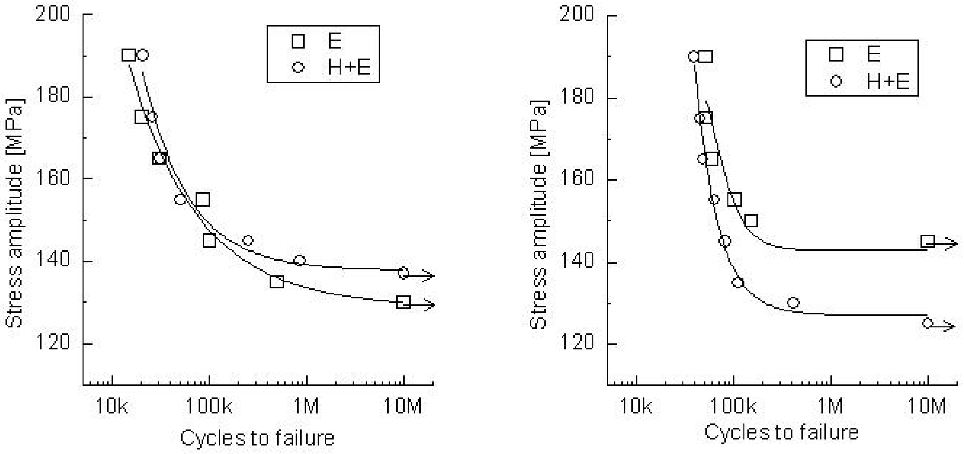

(a) ER12 (b) ER44

Figure 5.38: Fatigue performance of Mg alloys extruded with and without prior homogenization treatment

5.5.5 Effect of post-extrusion swaging treatment on fatigue performance

The SN curves of as-extruded and post-extrusion swaged alloys are shown in Fig. 5.39. The results show an improvement in the endurance life (equivalent to 10 million cycles) after post-extrusion swaging. In the as-extruded condition, the endurance limit in ZK60 alloy was higher than in AZ80 alloy (compare Fig.5.36 with Fig. 5.37), however, after post-extrusion swaging treatment, both alloys show similar endurance limit. Moreover, some other fatigue results, not presented here, showed that irrespective of the extrusion temperature, extrusion ratio and whether or not prior-homogenization treatment had been performed, the endurance limit remains the same after swaging. This confirms the fact that 170 MPa is the saturation endurance limit in both alloys. This results can be explained by the results of tensile test after rotary swaging treatment (Fig. 5.30), which show little difference between the values of yield stress and ultimate tensile stress i.e. not much of further work hardening is possible.

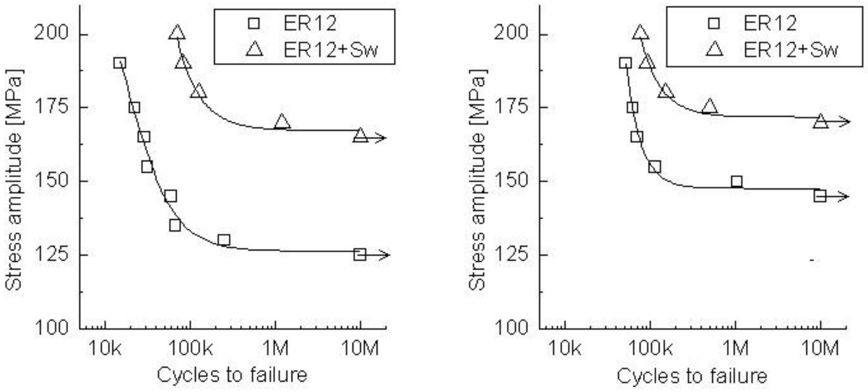

(a) AZ80 (b) ER44

Figure 5.39: Fatigue performance Mg alloys in as-extruded and post-extrusion swaged conditions

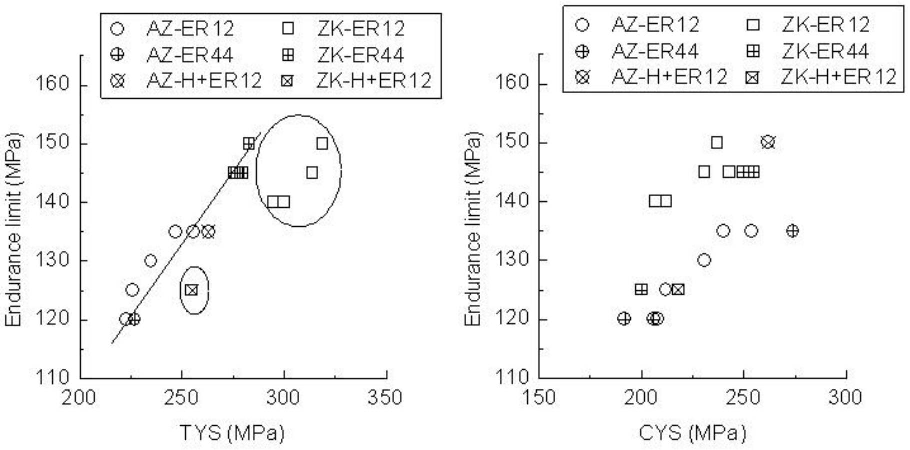

(a) TYS (b) CYS

Figure 5.40: Relationship between endurance limit and yield stress

5.5.6 correlation between the endurance limit and the yield stress

The fatigue results presented in Figs. 5.36, 5.37, 5.38 and 5.39, in general, show that the endurance limit increases with the increase in yield stress. Fig. 5.40 shows the endurance limit in all cases plotted against the tensile and compressive yield stress. The results show that except ZK60 alloy extruded at ER12 both with and without prior homogenization treatment (encircled data points on fig. 5.40a), the endurance limit increases linearly with the increase in tensile yield stress (TYS). Fig. 5.40b shows that no similar relationship exists between endurance limit and compressive yield stress (CYS). The ZK60 alloy shows higher endurance limit despite having same CYS as that of AZ80 alloy.

6 Discussion

6.1 Microstructural developments

6.1.1 The role of alloying elements

Several alloying elements are added to magnesium alloys for their specific benefits. In addition to solid solution strengthening, alloying addition also serves the purpose of grain refinement. Mg alloys can be broadly classified as Al bearing or Al free alloys. Al bearing Mg alloys are the most commonly used Mg alloys and are grain refined by super heating or inoculation [94]. On the other hand, Al free Mg alloys mainly refer to the alloys, which are based on the exceptional grain refining ability of Zr [60]. The microstructure of the Al bearing alloys can not be refined by Zr addition, because Zr and Al form stable intermetallic compounds with each other. Zn is another important alloying element in Mg alloys. The solid solution strengthening effect of Zn is much higher than that of Al at higher concentrations [90]. In general, the alloying addition of Zn increases the response of Mg alloys towards precipitation hardening and most of the precipitation hardenable Mg alloys contain Zn. Binary Mg-Zn alloys, however, suffer from grain coarsening and micro porosity [2]. These alloys are not susceptible to grain refinement by superheating and are generally grain refined by Zr additions [2]. The alloys selected in this study *i.e.* AZ80 and ZK60 are mainly Mg-Al and Mg-Zn alloys having relatively small additions (0.5%) of Zn and Zr, respectively. The microstructural analysis presented in section 4.1 shows that the two alloys exhibit different recrystallized microstructures after same thermo-mechanical treatment, such as large unrecrystallized regions and two populations of grain sizes after extrusion and poor poor DRX response during post-extrusion swaging treatment. In this section, the role of Zr addition in microstructure development during a thermo-mechanical treatment and explains the above stated microstructural features observed in ZK60 alloy is discussed.

Zr is an effective grain refiner for the magnesium alloys that do not contain Al, Mn, Si and Fe, because these elements form stable compounds with Zr. An addition of Zr can readily reduce the average grain size from a few millimeters to about 50 μm at normal cooling rates [95, 96]. In addition to the grain refinement, Zr addition gives a uniform microstructure because of the nearly round or nodular grains [97]. The refinement of grain size by Zr is generally attributed to the peritectic solidification, where Zr-rich magnesium solidifies first when nucleation starts at the primary Zr rich particles [2, 95, 98]. Not all the Zr rich particles, but only those which separate from the Zr master alloy near peritectic reaction temperature, give rise to such nucleation. Therefore Zr-rich cores are not seen around all Zr particles that are visible in the polished microstructure [2]. Similarly, the Zn-Zr intermetallic phase that precipitates from the saturated solid solution at low temperatures, also does not contribute to the grain refinement. A Zn-Zr intermetallic phase is present in the Zr bearing Mg alloys that have Zn concentration in excess of 4% [95]. As seen in Figs. 5.2 on page 31 and 5.8 on page 35, the contrast in the BSE image is based on Zn and Zr-rich cores are not visible as they were in the absence of Zn [98]. Therefore it is not possible to differentiate between the Zr-rich paticles associated with Zr-rich cores and other Zn-Zr particles on the BSE images. The WDX analysis performed on various Zn-Zr paticles shows Zn concentration in the range 15-50 wt% (Table 5.2 on page 31). An earlier study in Mg-4.5%Zn-0.7%Zr alloy has shown that the Zr-rich particles and intermetallic phases have smimilar compositions [2].

Magnesium alloys undergo dynamic recrystallization (DRX) during extrusion and the recrystallized grains are much finer than in the as-cast condition. The Zr-rich cores present in the alloy play an important role in the recrystallization behavior of the alloy. These cores give rise to the conditions that restrict grain growth after deformation [2], so when recrystallized, these cores result in pockets of very fine grains (Fig. 5.8 on page 35). The Zr-rich cores that do not recrystallize form "soft stringers" or striations, where the amount of Zr in solid solution is considerably higher than the immediate neighborhood [99]. It seems that the recrystallization of these cores is strongly affected by the mode of deformation. In the grains where slip dominates, new grains nucleate at the original grain boundaries and a thick necklace region recrystallizes leaving the center with only basal slip. On the other hand, the grains which undergo deformation twinning are likely to be replaced with new grains because of the nucleation at the twin boundaries [100].

In addition to fine and nodular grains, another advantage of Zr addition is a reduction in the amount of Mg-Zn compound at the grain boundaries, so that more Zn can go in the solid solution [2]. The WDX analysis (Table 5.2, page 31) suggests that the eutectic constituents present at the grain boundaries in the as-cast condition are Mg_7Zn_3, which is a primary metastable intermetallic phase and during post-casting heat treatment transforms to an equilibrium phase MgZn. This transformation, however, proceeds in a step and an intermediate phase Mg_4Zn_2 [101] or $MgZn_2$ [90, 2] is formed because of the thermodynamic preference. This transformation is affected by the alloying elements and their relative proportion [102]. In Mg-Zn alloys, this transformation starts after 2 h of isothermal aging at 200 °C. However, it takes long time before this decomposition completes [101]. Since the holding time (1 h) at the extrusion temperature (250 °C) before extrusion was relatively short, only some of the eutectic constituents could undergo the eutectoid decomposition (compare Table 5.2 on page 31 and Table 5.4 on page 35).

6.1.2 The role of extrusion ratio and temperature

Mg alloys undergo dynamic recrystallization (DRX) upon extrusion. It is believed that even at low temperatures, deformation induced internal energy raises the local temperature and the DRX is activated [103]. In general, the recrystallized grains are finer than the original grains. The size of the DRX grains is affected by the strain rate and the deformation temperature. This relationship is usually expressed in terms a temperature compensated strain rate parameter called ZenerHollomon parameter (Z) [4, 104, 72, 105]. Z is defined as Z = $\dot{\epsilon}e^{Q/RT}$, where $\dot{\epsilon}$ is strain rate, Q is activation energy similar to self diffusion, T is temperature and R is gas constant. Relation between Z and grain size is given by equation given below [72], where D is the grain size and m is a constant. Thus, a lower temperature results in higher Z and finer grain size. Thus, the grain size after thermo-mechanical treatment can be controlled by manipulating the strain rate and deformation temperature.

$$ZD^m = constant$$

. The temperature affects the grain size by influencing the modes of deformation and nucleation sites. At high temperatures, new grains nucleate at the original grain boundaries; while at low temperatures, there is an enhanced activity of deformation twinning and new grains also nucleate at the twin interfaces [4, 72, 89, 105]. The lowering of the extrusion temperature, therefore, provides additional nucleation sites and reduces the grain size. Similarly, higher strain and strain rate favor the activation of deformation twinning [106] and improve the recrystallization behavior. At low strains, a necklace of recrystallized grains is formed at the boundary regions leaving the deformed center unrecrystallized; while at high strain, the whole of the grains are recrystallized [107].

It is generally understood that a critical value of strain is required to cause the recrystallization and that the size of recrystallized grains decreases as the amount of strain is increased up to a second critical value of strain, beyond which the amount of strain has very little further effect on the grain size. Guo et al. [108] has reported that for the alloy AZ80, this second critical value of strain is 2 - 2.4. The amount of extrusion strain involved in the present study is over this critical value and varies between 2.5 and 3.8 for ER12 and ER44 respectively (Table 4.1. This is the reason why a finer grain size has not been observed for the higher extrusion ratio in AZ80 alloy. In contrast, the extrusion ratio plays an important role in the microstructure development in ZK60 alloy. The higher extrusion ratio (ER44) not only deforms the Zr-rich cores to fine bands (Fig. 5.7 on page 34) but also affects the mode of DRX. At lower strains, a conventional DRX involving bulging out of the part of serrated grain boundaries operates, while at higher strains a continuous DRX inside the grains becomes active [109]. This means that a thick layer of recrystallized grains is formed at ER44, and the "soft stringers" are reduced to a thin cross-section (Fig. 5.7 on page 34). Moreover a higher extrusion ratio also enhances the contribution of deformation twinning and thereby improves the recrystallization behavior by providing additional nucleation sites at the twin boundaries. Large "soft stringer" in the lower ER extrusions have significant effects on mechanical properties of the alloy [110].

It should be noted that due to the heat generation (during plastic deformation and due to friction) and the heat dissipation to surroundings, the actual extrusion temperature is not necessarily the same as the initial billet temperature. Keeping the extrusion ratio constant, it has been suggested that the net result is an increase in temperature, whose magnitude is a linear function of the logarithmic ram speed [111]. Probably, this is the reason that finer grain sizes have been observed at lower ram velocities in a AZ class of alloy[112, 113]. FEM simulations have shown an increases of surface temperature by $\sim$ 50 °C in AZ31 alloy, when the extrusion ratio is increased from 10 to 25 or from 25 to 50 while keeping the initial billet temperature constant at 250 °C [113]. The value of this temperature rise decreases as the billet temperature is raised and at 400°C billet temperature, an increase of $\sim$ 25 °C has been reported for similar increase of ER [113]. Therefore, it seems reasonable that though the billet temperatures were the same, the extrusion at higher ratio resulted in slightly higher die exit temperature [114]. This could be the reason for slightly larger grain sizes observed at ER44 in AZ80 alloy (Fig. 5.9, page 36). At lower temperatures (175-200 °C) for which ER44 was not possible and extrusions at an intermediate ratio (ER22) were done, the relative difference in extrusion velocities was small (Table 4.1 on page 23) and therefore the same average grain sizes have been observed for both extrusion ratios. This could also be the reason that with extrusion at 110°C, but at $\sim$ 8 times faster extrusion velocity, the attained grain size of 6 μm [80] is larger than 4 μm attained at 175 °C in the present study. These results are in agreement with Ding et al. [115] results, who also observed larger grain size at higher ER. Similarly Uematsu et al. [79] conducted the extrusion at comparable extrusion velocity of 1m/min and observed little variation of grain size with an increase in the extrusion ratio, but Ishihara et. al [78] conducted the extrusion at $\sim$ 5 times faster extrusion velocity (5 m min^{-1}) and observed a pronounced grain size enlargement. In ZK60 alloy, the additional heat generated during plastic deformation and friction at higher extrusion ratio could also be a contributing factor to the observed higher degree of DRX.

6.1.3 Microstructural changes during homogenization treatment

The backscattered electron micrographs of the alloy before and after the homogenization treatment and the line scans of Zn and Zr concentration are shown in Figs. 5.5 and 5.6. The micrograph before homogenization shows Mg-Zn eutectic phase and Zn-rich ring at the grain boundary. The elemental concentration of Zn 25-30 wt% determined by WDX analysis (Table 5.2 on page 31) suggests the eutectic phase to be Mg_7Zn_3. Because of their fine sizes and therefore a significant influence of the neighbourhood in WDX analysis, the Zn-Zr intermetallic particles show a large variation in the concentration 20-50 wt% Zr (Table 5.2 on page 31). Previous studies conducted in Mg-Zn-Zr alloys have characterized them as $ZnZr_2$ or Zn_2Z_r3. Both Mg_7Zn_3 eutectic and Zn-rich ring disappear after the homogenization treatment, however Zn-Zr intermetallic particles are not affected and their number remains the same. The profile of Zr concentration is not affected by the homogenization treatment and shows a peak value of approximately 1.2 wt% at the centre of the grain, in both cases (compare Fig. 5.3 on page 32 with Fig. 5.6 on page 33). The profile of Zn concentration however, shows a shift of the peak value, which moves from grain boundary region to Zr-rich region inside the grain after the homogenization treatment. The electron micrographs after extrusion in both pre-homogenized and with no prior homogenization are shown in Fig. 5.5 on page 33. After extrusion, the eutectic phase forms parallel bands in the extrusion direction, which are absent in the case of pre-homogenized extrusion. The elongated regions with different contrast, darker in the case of no prior homogenization and lighter in the case of prior homogenization, are Zr-rich regions having >1wt% Zr concentration. The concentration of Zn in these cores (2-2.5 wt%) is lower than matrix (4.5-5.5 wt%) in the case of no prior homogenization, but is higher (5.5-6 wt%) than the matrix (4-4.5 wt%) in the case of pre-homogenized extrusion. The optical micrographs of the extruded alloys are given in Fig. 2 (c,d). The microstructure in both cases consists of recrystallized grain, elongated bands of unrecrystallized Zr-rich cores and the recrystallized Zr-rich cores having very fine size (2-4 μm). In the case of pre-extrusion homogenization, the recrystallized grains are significantly coarser (>10 μm) than in the case of non-homogenized extrusion (<5 μm), and a higher proportion of the Zr-rich cores recrystallize.

The tendency to segregate at solidification front is mainly a thermodynamic property and depends on the concentration of the alloying element. The degree of segregation, however, is effected by the interactions among the solid solution constituents. The solute interactions among alloying elements and solvent affect the solubility of the solute atoms and thus their segregation, while high cooling rates allow little time for solutes to segregate. The DC-casting is a semi-continuous casting process and the cooling rates are higher than in the conventional casting processes such as sand casting or metal die casting. At such cooling rates, the typical dendrites are not formed; however, the solute atoms do segregate at the grain boundaries. The segregating Zn in case of ZK60 alloy forms Zn-rich ring and the Mg-Zn eutectic at the grain boundary. The alloying addition of Zr in Mg-Zn lowers the degree of segregation by increasing the Zn solubility in Mg and thus lowering the amount of eutectic at the grain boundaries. The maximum solubility of Zn in Mg at eutectic temperature is about 6.2 wt%, which is approximately equal to the maximum Zn concentration observed in Zn-rich rings. The excess of Zn forms the eutectic compound with Mg which contains more than 50 wt% Zn. In addition, Zn is also removed by the Zn-Zr intermetallic compound which is present in Mg-Zn-Zr alloys having Zn concentration in excess of 4%. The intermetallic compound has been characterised as

$ZnZr_2$ or Zn_2Zr_3 in earlier studies. Although these compounds do not belong to the ground state of Zn-Zr system, but are believed to be stabilized at high temperature because of the entropic effects. Thus, in as-received condition, Zn is so segregates that one third is dissolved in the solid solution, while the rest is consumed by the Zn-rich ring, Mg-Zn eutectic and Zn-Zr intermetallic compound.

Homogenization treatment involves the removal of micro segregation of alloying elements by the inter-atomic sold state diffusion. The driving force for the diffusion is the lowering of the free energy of the system. In general, the diffusion flux moves from a region of high concentration to a region of low concentration, which increases the entropy of the system, while, the free energy of the system decreases. The chemical interactions among alloying elements also influence the free energy of the system. In some cases, dissolution of one element may be thermodynamically more favorable than its diffusion. In such a case, the diffusion flux may move from lower concentration to higher concentration, a phenomenon usually called the up-hill diffusion. The homogenization temperature (400 °C) is well over the melting point of the Mg-Zn eutectic (340 °C) but is much lower than the reaction temperature of Zn-Zr intermetallic compound; therefore, all the eutectic phase is dissolved during the homogenization treatment while Zn-Zr intermetallic compound is not affected. During the homogenization treatment, Zn diffuses from grain boundary regions to grain interiors and removes the segregation that occurred during casting. At Zr-rich cores, high Zr concentration increases the affinity of Zn with Mg, and an up-hill diffusion occurs making the Zn concentration maximum there.

6.1.4 The roles of pre- and post- extrusion homogenization treatments

Mg alloys undergo dynamic recrystallization during deformation. The DRX mechanism varies with the deformation conditions (strain rate and temperatue) and is closely related to the mode of deformation. The deformation inhomogeneities , second phase particles [80] and twin activation at lower temperatures promote a discontinuous DRX at the interfaces; while at elevated and higher temperatures, a continuous DRX operates and is controlled by cross slip and dislocation climb [80]. A continuous DRX mode is generally observed in metals where dislocation motion is restricted by a lack of active slip systems or solute drag. The recrystallization process does not end with the deformation, and after DRX the alloy undergoes a combination of conventional static recrystallization and metadynamic recrystallization, generally refereed as the secondary recrystallization. These two mechanisms differ in the sense that former depends largely on the pre-strain and temperature but only little on strain rate, while the latter is insensitive to pre-strain and temperature but is affected by the strain rate. [80]. The DRX grains grow during the secondary recrystallization and their growth is controlled by the second phase particles, texture and surface effects.

Fig. 5.4 on page 32 shows that in AZ80 alloy, the pre-extrusion homogenization heat treatment significantly dissolves the β-phase, while Al-Mn particles are not affected. This observation is consistent with an earlier study conducted on AZ80 alloy [80]. During the extrusion, the β-phase is broken and thus does not give rise to the inhomogeneous deformation zones which can initiate nuclei for the recrystallization process, therefore, dissolution of β-phase does not affect the DRX mechanism and a continuous DRX occurs during both unhomogenized and homogenized extrusions. However a higher volume fraction of β-phase in unhomogeized extrusion effectively inhibits the grain growth during DRX and the secondary recrystallization that follows. Therefore, the recrystallized grains are restricted to fine sizes measuring 2-5 μm.

While in the case of pre-homogenized extrusion, localized grain growth occurs at regions free of β-phase. This gives rise to an abnormal grain growth and another population of grains measuring 5-10 μm appears (Fig. 5.13).

The post-extrusion annealing behavior in Mg alloys conforms to what is known for the recrystallization reaction. The grain coarsening is continuous and the stable grain size strongly depends on prior deformation conditions i.e. the Zener−Hollomon parameter (Z), which is a temperature compensated strain rate parameter [115]. The grain growth is selective and certain grains grow at the expense of other grains. In AZ31 alloy, the $(11\bar{2}0)$ component grows in the rolling direction at the expense of other grains; in AZ61 alloy, the growth of this component is accompanied by an abnormal grain growth. This difference is possibly due to the second phase particles, which are present in larger fraction in AZ61 than in AZ31 alloy, and therefore are more effective in preventing the grain growth around their neighborhood. The nature of grain growth is also related to the degree of DRX after deformation. It has been observed that a DRX level of 80-95% leads to an abnormal grain growth. The annealing temperature strongly affects the kinetics of grain growth. The rate of grain growth varies with annealing temperature [12]. It is very low during annealing at 300 °C, so the microstructure is not much affected. At 400 °C, however, the grain growth rate increases rapidly and significant grain coarsening occurs (Fig.

6.2 Texture development

6.2.1 The role of alloying elements

Extrusion of magnesium alloys involves the deformation and dynamic recrystallization of the original grains. The crystallographic texture after deformation contains components from both these processes. The deformation mode in closed packed hexagonal lattices is closely related to the axial ratio (c/a ratio) of the lattice. Any change in the c/a ratio may change the closest packed direction in the lattice and thereby the most active slip system. In closed packed hexagonal (CPH) lattice of Mg, the inter-atomic distance is shortest in $\langle a \rangle$ direction. Therefore, Mg alloys exhibit a fibrous basal texture after deformation in which the basal plane containing the $\langle a \rangle$ direction is aligned in the extrusion direction, i.e basal plane normal is perpendicular to the extrusion direction. Addition of alloying elements changes the c/a ratio or even the crystallographic lattice itself in Mg [116]. The lattice parameters are affected by both the atomic size and valency number. An addition of a larger atom generally expands the lattice and vice versa. The valency of the alloying element changes the electronic concentration in the unit cell and may cause an overlapping between Brillouin zones, thereby affecting the a and c parameters of the lattice differently . Both Al and Zn have smaller atomic sizes than Mg. Therefore, addition of Al or Zn causes contraction in lattice in both $\langle a \rangle$ and $\langle c \rangle$ directions. However, because Mg and Zn have same valency number, Zn addition has no effect on c/a ratio related to the valency number. On the other hand, Al has a higher valency number than Mg. An addition of Al causes an overlap between first Brillouin zone into the second Brillouin zone. Consequently, Al addition shows smaller contraction in c-parameter than the a-parameter, thereby expanding the c/a ratio.

The recrystallization process is also affected by the alloying additions. The intermetallic particles and other microstructural features, such as Zr-rich cores in the case of Zr addition, play an important role in the recrystallization process. The recrystallization texture in Mg alloys is not much different from the deformation texture, some of the grains rotate around c-axis by 30° during recrystallization; however, the orientation of c-axis with respect to deformation direction does not change [2, 89]. Thus, the degree of recrystallization affects the intensity of $\{10\bar{1}0\}$ component of texture, which lowers as the degree of recrystallization increases. Alloying elements such as Zr affect the texture development by affecting the recrystallization process. Zr addition leads to the formation of Zr-rich cores which show poor DRX response upon deformation and thus affect the texture intensity (Fig. 5.8 on page 35).

The texture results presented in Fig. 5.18 on page 43 and Fig. 5.19 on page 43 show that after same thermo-mechanical treatments, the crystallographic texture in both alloys is similar; however, the $\{10\bar{1}0\}$ pole intensity in ZK60 alloy is always higher than in the AZ80 alloy. Although, the higher valency number of Al introduces an effect on c/a ratio, which is not present in the case of Zn addition (because Mg and Zn have same valency number), the atomic radius of Al (1.25 Å) is smaller than the Zn (1.35 Å). Consequently, Al and Zn have fairly similar effect on the c/a ratio of the Mg lattice. A study conducted only to 3% of solute contents shows similar values of c/a ratio after Al and Zn additions. Therefore, the deformation process in both alloy is the same, with basal slip being the preferred mode of deformation. An as a result, a fibrous basal deformation texture is formed in both alloys. However, Zr-rich cores in ZK60 alloy show poor recrystallizatio behavior upon deformation. Therefore, the texture in ZK60 alloy shows a stronger $\{10\bar{1}0\}$ component, which is weakened by a higher degree of recrystallization in AZ80 alloy.

6.2.2 The roles of extrusion temperature and extrusion ratio

Like alloying addition, the deformation conditions affect the crystallographic texture by affecting the deformation and recrystallization process. Because of their closed packed hexagonal lattice, Mg alloys have a predominant basal texture after the deformation. Except for the deformation twinning and the slip with <c+a> burger vector, all other deformation modes impart deformation along $\langle a \rangle$ direction of the closed packed hexagonal lattice of the Mg alloys. This uni-directional deformation in Mg alloys results in a fibrous type deformation texture in the extrusion direction, in which plane normal is aligned parallel to the extrusion direction i.e. the basal plane normal is perpendicular to the deformation direction [89, 104]. Therefore, the basal plane (0001) shows maximum pole intensity at 90 ° in the pole figures (Figs. 5.16 and 5.17 on pgs. 41 and 42, respectively). Recrystallization texture in Mg alloys also follows the deformation texture [72]. During recrystallization some of the grains rotate around c-axis by 30° however the angle of c-axis with respect to deformation direction does not change [2]. The EBSD analysis has shown that all unrecrystallized grains have an $\langle 10\bar{1}0\rangle$ orientation; while in the recrystallized grains a strong $\langle 11\bar{2}0\rangle$ component is accompanied by a weak $\langle 10\bar{1}0\rangle$ component [89]. Thus a higher degree of recrystallization weakens the $\langle 10\bar{1}0\rangle$ component of the texture.

Earlier studies suggest that the texture development during recrystallization strongly depends on prior plastic deformation and is weakened after higher strains [9, 117]. The recrystallization mechanism does not end with the deformation and a DRX is followed by a combination of conventional static recrystallization and metadynamic recrystallization [118]. In extruded Mg alloys, the post-deformation secondary recrystallizaton reduces the maximum pole intensity of $\{10\bar{1}0\}$ plane, while the maximum pole intensity of $\{11\bar{2}0\}$ plane remains unaffected [104]. The results presented in Figs. 5.18 and 5.19 on pages 43 and 43 , respectively, show that at higher strain (the higher extrusion ratio), the maximum pole intensities of $\{10\bar{1}0\}$ plane are lower than the ones at lower extrusion ratio. This indicates a higher degree of recrystallization, which is confirmed by the microstructural results (Fig. 5.7 and 5.8 on pages 34 and 35, respectively).

The results are in agreement with an earlier observation in AZ80 alloy which was extruded under the same conditions [119]. The values of the maximum pole intensities in ZK60 alloy are much higher than the ones observed in AZ80 alloy, because of the relatively lower degree of recrystallization (Fig. 5.7 and Fig. 5.8).

Experimental evidences suggest that the texture development is literally insensitive to the annealing conditions and show a strong dependence on prior plastic deformation [119, 120]. Therefore, it appears that after a higher degree of deformation i.e. higher ER, a stronger post-extrusion secondary recrystallization response is shown and results in a lower intensity of $\langle 10\bar{1}0\rangle$ component; whereas, the intensity of $\langle 11\bar{2}0\rangle$ component remains unchanged. No variation in the texture intensity at different extrusion temperatures suggests that this secondary recrystallization is insensitive to the extrusion temperature.

6.2.3 The roles of pre- and post-extrusion heat treatments

The results presented in Figs. 5.20 and 5.21 show that both the pre- and post- extrusion homogenization treatments do not have any qualitative effect on the extruded texture. These treatments, in general, lower the maximum pole intensity of $\langle 10\bar{1}0\rangle$ plane, while the maximum pole intensities of (0001) and $\langle 11\bar{2}0\rangle$ planes are not much affected. These results indicate that both treatments have no effect on the DRX behavior of the alloys during extrusion. In both alloys, it proceeds with a continuous DRX mechanism, since the recrystallization textures in the case of discontinuous DRX are significantly different than the deformation texture [85]. A discontinuous DRX caused by particle stimulated nucleation (PSN) is generally attributed to give a nearly random texture in wrought Mg alloys [121]. The optical micrographs in the case of pre-extrusion homogenization (Fig. 5.11d) reveal extended recrystallization in some grains, resulting in two populations of grain sizes in AZ80 alloy. This extended recrystallization causing grain coarsening is responsible for the lowering of the maximum pole intensities,especially that of $\langle 10\bar{1}0\rangle$ plane. Similarly, the grain growth during post-extrusion annealing treatment also reduces the maximum pole intensity of $\langle 10\bar{1}0\rangle$ plane. A significant grain coarsening occurs during post extrusion annealing at 400 °C, and similar maximum pole intensities of the measured planes are observed. Earlier studies have shown that abnormal grain growth [122] and development of $(11\bar{2}0)$ texture component [11] weaken the texture in deformed AZ series of Mg alloys.

6.3 Tensile and compressive properties

6.3.1 The strength differential effect in as-extruded condition

The anisotropy in yield stress under tension and compressive loading (strength differential effect, SDE) is a typical phenomenon in the extruded magnesium alloys. It is caused by the textured microstructure after extrusion and is affected by the grain size. Out of several modes of plastic deformation reported for magnesium alloys, basal slip $(0001)\langle 11\bar{2}0\rangle$ is the dominant mode requiring much lower critical resolved shear stress (CRSS) for activation than other modes. At room temperature, the critical resolved shear stress for the prismatic slip $\{10\bar{1}0\}\langle 11\bar{2}0\rangle$ and the pyramidal slip $\{10\bar{1}1\}\langle 11\bar{2}0\rangle$ is 100 times higher than for the basal slip [18]. Twinning is another important mode of deformation and requires second lowest CRSS at room temperature [32]. Twins in HCP metals are usually classified as tensile or compressive twins, depending whether they cause tension or compression along c-axis respectively. The tensile twins are the most observed twins in Mg alloys [30, 123] and in HCP metals having c/a ratio lower than the ideal 1.633 i.e. magnesium, titanium and zirconium, it is the only twin system activated during c-axis tension [32]. On the other hand, the compressive twins frequently appear as complex doubly twinned structures that exhibit high local shear strains; the reluctance of Mg alloys to contraction twinning gives a higher value of uniform elongation [31]. In the as-extruded condition, most grains have their basal planes aligned parallel to the extrusion direction. When the extrusions are loaded along the longitudinal direction, the basal slip having slip direction within the basal plane is inhibited because of a low Schmidt factor. In the case of longitudinal tensile testing, other modes of slip and twinning require still higher stresses for activation. However, under longitudinal compression, the c-axis is perpendicular to the applied load and tensile twinning is favored and a relatively lower compressive YS is observed [30, 124, 125]. In-situ texture measurements have revealed that under tensile loading, the deformation proceeds primarily with the basal slip along with some twinning and non-basal slip, occurring at regions of stress concentration and in favorably aligned grains; while under compression, the deformation starts with twinning and contribution of the basal slip increases with deformation [123, 125].

6.3.2 The effect of extrusion temperature and the extrusion ratio

Grain boundary strengthening presented by the well-known Hall-Petch relation, is an established method of increasing the yield stress and is the main contributor in the improved (increased) strength. A comparison of the mechanical properties in as-cast (Fig. 5.23 on page 46) and as-extruded conditions (Figs. 5.25 and 5.26) shows the significant increase in strength and ductility due to profound refinement in grain size upon extrusion. Similarly due to a progressive grain refinement with the lowering of extrusion temperature in AZ80 alloy, the yield stress progressively increases with the lowering of extrusion temperature. In contrast, due to the low degree of recrystallization and inhomogeneous microstructure at all extrusion temperatures, the mechanical properties in ZK60 are not affected by the extrusion temperature.

The inhibition of the basal slip in the longitudinal direction is manifested in Fig. 5.27 which shows the variations in the compressive yield stress as the loading direction is changed from the longitudinal (0°) to the intermediate (45°) and the transverse (90°) direction. The longitudinal samples show significantly higher YS values compared to the other two directions, which show almost the same values. As discussed above when compressed in the longitudinal direction (0°), the basal slip is inhibited and the deformation starts with twinning, which requires the second lowest CRSS at room temperature. But as the angle is changed with respect to extrusion direction, the Schmidt factor for the basal slip increases [124]. This relative ease of the basal slip results in a lower compressive YS, for samples tested in directions other than the longitudinal. The results in Fig. 5.27b show that directional activation of the tensile twins causes a difference of $\sim$ 25 MPa in the observed CYS. This is equal to the difference between longitudinal TYS and CYS caused by the crystallographic texture at higher extrusion ratio. This result further reinforces the notion that four times larger difference between longitudinal TYS and longitudinal CYS observed in the case of lower extrusion ratio can not be due to the texture and thus is likely to be caused by the large unrecrystallized grains in ZK60 alloy.

The differences of YS values caused by the strength differential effect (SDE) in AZ80 alloy are relatively small (Fig. 5.25), because of the fine grain sizes (8-4 μm). On average, the compressive YS is 90% of the tensile YS, and the difference becomes even smaller with the lowering of extrusion temperature from $\sim$ 20 MPa at 350°C to $\sim$ 5MPa at 175°C. In comparison, for a coarse grain sized (30 μm) AZ31 extrusion [124], the compressive YS has been only 50%

of the tensile YS. By justifying and applying the CRSS criterion, a value of 65-75 MPa has been suggested for the activation of tensile twins in an extruded Mg-7.7 at% Al alloy [123]. Neglecting the effects of grain size and second phase particles, it has been argued that the alloy is likely to yield at a stress two times higher than under compression [124]. The observed higher compressive YS (200-245 MPa) shows the strengthening caused by fine grain size and second phase particles. The grain size affects the compressive YS by affecting the CRSS required for twin nucleation. For a twin to nucleate in a smaller grain, a higher surface to volume ratio increases the value of shear stress that is required for the twin initiation [126]. A transition from twinning to slip dominated flow has been observed with the reduction in grain size [7].

Results presented in Figs. 5.25 and 5.26 show relatively higher tensile elongation values at higher ER. Furthermore they also show an insensitivity of elongation values to the extrusion temperature. This is despite the fact that grain size reduces with the lowering of extrusion temperature. The ductility of magnesium alloys increases with grain refinement [1], activation of non basal slip [127] and the tensile twinning [128]. Out of these, the latter two are directly affected by the texture. A pronounced basal texture observed in the extruded Mg alloys can strongly lower the ductility; the deformation becomes inhomogeneous and is dominated by the formation of shear bands [129]. For this reason, the tensile elongation of the extruded AZ31 alloy was only 50% of the elongation of the same alloy, which was deformed by equal channel angular extrusion (ECAE) and then subsequently annealed to have a similar average grain size [130]. Therefore, it is suggested that a relatively strong basal texture observed at the lower extrusion ratio (Fig. 5.18 on page 43 and Fig. 5.19 on page 43) gives a relatively low tensile elongation value. Moreover, the elongation values show an insensitivity to the extrusion temperature as was observed in the case of texture intensity.

6.3.3 Effect of pre and post extrusion homogenization treatments

In AZ80 alloy, the homogenization treatment partially dissolves the β-phase ($Mg_{17}Al_{12}$) which contains 4 times more Al than in the matrix (Fig. 5.4). After dissolution, this Al goes into the solid solution and contributes in solid solution strengthening. An earlier study has shown that the YS of AZ80 alloy after complete β-phase dissolution is slightly higher than in the case of a partial β-phase dissolution [82]. The dissolution of β-phase also improves the recovery response of the alloy during deformation and results in a lower strain hardening rate. Thus, stress saturation arises after a higher degree of deformation than the non-homogenized condition [82]. Although the optical micrographs show similar microstructures (Fig. 5.11), a weaker basal texture in the cases of pre-exturusion homogenization (Fig. 5.20a) weakens the effects of crystallographic texture on anisotropy in mechanical properties (Section 6.3.1). Because, there are fewer grains having their basal planes oriented parallel to the loading direction, the strength differential effect (SDE) is eliminated and the directional anisotropy in yield stress is reduced to almost half in comparison to the extrusion without prior homogenization treatment. An earlier study conducted on $Mg_{93}Zn_6Ho$ alloy has also shown that SDE is eliminated for the weaker crystallographic texture [131]. Figs. 5.13 and 5.21 show that the post-extrusion annealing treatment at 300 °C has only little effect on microstructure and crystallographic texture. Accordingly, the mechanical properties are also only slightly changed. However, after the annealing treatment at 400 °C, the grains coarsen (Fig. 5.13) and the texture intensities of various planes become equal (Fig. 5.21). Therefore, the so called texture strengthening effect in the longitudinal direction vanishes and similar values CYS in longitudinal and transverse directions are observed. The strength differential effect is also removed and yield stress becomes isotropic at a value little lower than the previous CYS in transverse direction. This lowering of

YS could be due to the grain coarsening that occurs during secondary recrystallization.

The prior homogenization treatment at 400 °C dissolves all eutectic constituents in ZK60 alloy (Fig. 5.5), and the microstructure after subsequent extrusion consists of significantly coarser recrystallized grains (Fig. 5.12) having a relatively weaker basal texture (Fig. 5.20b). Therefore, the deformation starts at a lower stress and a lower yield stress is observed [83]. The pre-extrusion homogenization improves the recovery process of the alloy during deformation and results in a lower strain hardening rate [82] allowing a higher degree of strain hardening (60 MPa) before fracture in comparison to the extrusion without prior homogenization (25 MPa). In addition, this causes the stress saturation to occur after a certain degree of deformation and results in a higher tensile elongation. In as-extruded condition, the second phase particles hinder the recovery process during deformation and cracks nucleation occurs around these particles resulting in an early fracture. Another reason for higher tensile elongation in the case of pre-extrusion homogenization is the weaker basal texture. During deformation, the crystals (grains) with higher orientation factor (Schmidt factor) for basal slip deform first and align their basal planes parallel to the deformation direction. Further basal slip in these grains is not possible because of a very low Schmidt factor [124]. The basal slip is the predominant slip system in Mg lattice and except for <c+a> pyramidal slip, all other slip systems have their slip direction in the basal plane. Therefore, in case of a stronger basal texture, a higher fraction of grains are unfavorably oriented for crystallographic slip resulting in a lower value of tensile elongation.

6.4 Tensile properties at elevated temperature

6.4.1 The effect of grain size

The results presented in Figs. 5.31, 5.32 and 5.33 show the effects of grain size on tensile properties at elevated temperatures. The grain size in as-cast condition is about 100 μm (Fig. 5.1a), whereas, after extrusion the recrystallized grain size at various extrusion conditions is $<$ 10 μm. At low temperatures (T $\leq$ 200 °C), the deformation mode is not much different than at the room temperature, and crystallographic slip and deformation twinning are the most active deformation modes. Liu et al. observed that in the coarse grain alloy dislocation slip is the predominant deformation mode. Slip induced grain rotations are accommodated in coarse grains by multiple low angle grain boundaries which evolve into high angle grain boundaries during the DRX [132]. As the temperature increases, the activities of cross-slip and dislocation annihilation mechanisms increase and become more effective. At temperatures higher than 200 °C, the activity of non-basal slip systems increases and the strain hardening rate decreases with increasing temperatures. Thus, in the as-cast condition, the rate of strain hardening decreases steadily with the increase in temperature (Fig. 5.31) and at 300 °C in ZK60 alloy and at 350 °C in AZ80 alloy, the overall work hardening is almost zero. Thus, there exists a dynamic balance between storage of dislocations and their annihilation [133]. In case of fine grain sizes, i.e. in as-extruded condition, both alloys show superplasticity at a temperature $\geq$ 250 °C i.e. 0.56 T_m. In contrast to coarse grain sizes in as-cast condition, the fine recrystallized grains undergo grain boundary sliding (GBS) and result in extended plastic deformation at low stresses (Figs. 5.32 and 5.33). Since, not all grain boundaries slide to same extent. In order to maintain grains stability and avoid premature failure by extensive cavitation, it is, therefore, necessary that GBS is accompanied by another process such as grain boundary migration, recrystallization, diffusional flow and dislocation creep [93]. In AZ61 alloy, it has been reported that the grain boundary sliding (GBS) is accommodated by slip, which is controlled by grain boundary diffusion at 523-573 K, and by lattice diffusion at 598-673 K respectively [134].

6.4.2 The effect of extrusion temperature and extrusion ratio

The tensile behavior of the extruded alloys at elevated temperatures is mainly affected by grain size and microstructural homogeneity. The microstructural results presented in Figs. 5.9 and 5.10 show microstructural changes caused by the variations in extrusion temperature. In AZ80 alloy, the microstructure is relatively homogeneous and grain sizes are only slightly different at all extrusions. In ZK60 alloy, the microstructure is relatively inhomogeneous and the recrystallized grain sizes at various extrusion temperatures are not significantly different. Accordingly, the flow curves at various temperatures show similar behavior in Figs. 5.32 and 5.33, except that the flow stress peak is higher in the case of higher extrusion ratio. Thus, the microstructure is thermally more stable in the case of higher extrusion temperature, and the on set of dynamic recrystallization indicated by the peak in the flow stress appears at higher stress. The effect of extrusion ratio on microstructure development is not so significant in AZ80 alloy (Fig. 5.9). In comparison, however, extrusion ratio plays a significant role on microstructure development in ZK60 alloy (Fig. 5.10). A much less degree of recrystallization upon extrusion results in large uncrecrystallized regions comparable with the as-cast grain size, and coarse recrystallized grains. Both these microstructural features hider the grain boundary sliding mechanism [15] resulting in much lower elongation (~25%) in the case of lower extrusion ratio (Fig. 5.33).

6.5 Fatigue performance

6.5.1 The effect of extrusion on fatigue behavior

A comparison of the SN curves in as-cast (Fig. 5.35a) and as-extruded conditions (Fig. 5.36 and 5.36) shows that fatigue life is significantly improved after extrusion in both alloys. The as-extruded alloys show a run out stress (corresponding to 10^7 cycles without failure) of >120 MPa, whereas in as-cast condition, both alloys failed before 10^6 (one million) cycles even at a stress amplitude of 20 MPa. The pronounced improvement in YS caused by significant grain refinement upon extrusion is the main contributor in fatigue life improvement. Once nucleated, the cracks can propagate without being stopped to longer lengths in the case of coarse grain size. Another factor in fatigue life is the role of second phase particles. Since, intermetallic phases $Mg_{17}Al_{12}$ and Al_8Mn_5 in AZ80 alloy, and Mg_7Zn_3 and Zn_2Zr_3 in ZK60 alloy are harder than the Mg matrix, these phases contribute to strength by blocking the moving dislocations. However, under repeated cyclic loading, the regions of mismatch around these particles can lead to crack initiation. During extrusion, the eutectic constituents *i.e.* $Mg_{17}Al_{12}$ in AZ80 and Mg_7Zn_3 are broken down and form parallel bands in the extrusion direction (Figs. 5.7 and 5.8). However, the sizes of Al-Mn particles identified as Al_8Mn_5 and Zn-Zr particles identified as Zn_2Zr_3 are not affected. Thus, when the fatigue samples are machined along longitudinal direction, as is the case in present study, the propagating cracks had to pass through these bands of eutectic constituents by breaking them. The repeated arrest of propagating crack at these parallel bands lowers the rate of crack propagation and results in higher number of cycles before failure in as-extruded condition [135].

6.5.2 The effect of extrusion parameters on fatigue behavior

Fig. 5.40 presents a good overview of the effects of extrusion temperature, ratio and pre-extrusion homogenization treatment on fatigue behavior of both alloys. The figure 5.40a shows that observed endurance limit can be directly related to the tensile yield stress (TYS), except for ZK60 alloy extruded at lower extrusion ratio. Thus, increase in the TYS due to the presence of large strain hardened unrecrystallized regions does not improve the fatigue performance. Moreover, figure 5.40b shows that compressive yield stress (CYS) has no affect on the endurance limit of the extruded alloys. Thus, the fatigue lives are similar at lower and higher extrusion ratios in ZK60 alloy, although the CYS in the case of lower extrusion ratio is significantly low ($\sim$75-100 MPa depending upon extrusion temperature, see Fig. 5.26a). Figs. 5.25 and 5.26 show that the extrusion temperature and the extrusion ratio have only little effect on tensile yield stress of the alloys. Accordingly, Figs. 5.36 and 5.37 show very little variation in the fatigue behavior of both alloys extruded at various temperatures and ratios. In general, the endurance limit is 50% of the TYS in all cases, except in ZK60 alloy extruded at lower extrusion ratio, due to reasons discussed earlier.

In addition to influencing the tensile yield stress, pre-extrusion homogenization treatment affects the volume fraction of eutectic constituents and therefore, also the fatigue behavior. The SN curves presented in Fig. 5.35b show the fatigue behavior of AZ80 and ZK60 alloys after homogenization treatment at 400° C. The tensile yield stress in AZ80 alloy is slightly increased after partial dissolution of β phase, whereas, in ZK60 alloy, the tensile yield stress is reduced due to a complete dissolution of eutectic constituents. However, when normalized to tensile yield stress, the cycles to failure at the same normalized stress are higher in the case of homogenized condition. The similar behavior is observed after extrusion in ZK60 alloy. The high cycle fatigue behavior of the extruded ZK60 alloy extruded with and without prior homogenization treatment is presented in Fig. 5.38b. Although, the tensile yield stress in the case of pre-extrusion homogenization is lower by 70 MPa (Fig. 5.28), the run out stress for 10 million cycles is only lower by 20 MPa. When normalised to tensile yield stress, the run out stresses correspond to 45 % and 50% of the TYS for extrusion without prior homogenization and with prior homogenization, respectively. Thus, in terms of fatigue life normalised to yield stress, an improvement of 5 % is observed with prior homogenization heat treatment. This improvement is attributed to higher degrees of strain hardening and elongation observed in the case of pre-extrusion homogenization. In addition, pre-extrusion homogenization lowers the potential crack nucleation sites. Fatigue crack nucleation in Mg-Zn-Zr alloys reportedly occurs on unrecrystallzed banded region [136] and oxidised surface [137]. Pre-extrusion homogenization dissolves all the Mg-Zn eutectic and results in a higher degree of recrystallization on subsequent extrusion; while, dissolution of second phase particles, which act as local cathode during corrosion reaction, lowers the chemical potential of the alloy and lowers the possibility of localised oxidised surfaces.

7 Conclusions

1. The microstructure of a DC-cast Mg-8%Al-0.5%Zn alloy consists of divorced $Mg_{17}Al_{12}$ eutectic dispersed in the solid solution containing about 6% Al. In addition the alloy contains Al_8Mn_5 intermetallic compound. The microstructure of a DC-cast Mg-6%Zn-0.5%Zr alloy consists of Zr-rich cores associated with the Zr-rich particles, Zn-rich rings and Mg_7Zn_3 eutectic constituents at the grain boundaries, and ZnZr precipitates which are formed during cooling of the saturated solid solution.
2. The extrusion process breaks the eutectic constituents in AZ80 alloy, which form parallel bands in the extrusion direction. The recrystallized grain size is in general less than 10 μm. The characteristic Zr-rich cores formed during casting in ZK60 alloy play an important role in the DRX in ZK60 alloy. After extrusion, these cores are only partially recrystallized. The unrecrystallized cores form parallel bands which are elongated in the extrusion direction and curled around the extrusion axis. The high Zr concentration in the cores which recrystallize restricts the grain growth, so these cores form pockets of grains finer than the other recrystallized grains. Thus, two populations of grain sizes (1-3 μm and < 10 μm) are formed.
3. The extrusion temperature influences the activation of various modes of plastic deformation and the DRX response. At lower temperatures, twinning is more active, new grains nucleate at the twin interfaces and a fine grain size is achieved. At higher temperatures, there is predominant bulging of original grain boundaries, new grains nucleate at the original grain boundaries and a relatively coarse grain size is achieved. In AZ80 alloy, there is a progressive grain refinement with the lowering of extrusion temperature. While in ZK60 alloy which exhibits poor DRX response, the extrusion temperature only increases the volume fraction of recrystallized Zr-rich cores and the recrystallized grain size is not changed.
4. The extrusion ratio affects the grain size by affecting the degree of recrystallization and the die-exit temperature. An increased twinning contribution and a dynamic recrystallization within the grains reduce the recrystallized grain size at higher extrusion ratio. For the same value of ram velocity, a higher extrusion ratio corresponds to a higher extrusion velocity. This raises the die exit temperature and may result in relatively coarser grain size. In AZ80 alloy, the degree of recrystallization at all extrusion ratios is fairly similar, thus the effect of second factor is more pronounced and a slightly coarser grain size is observed at higher extrusion ratio (ER44). Whereas, in ZK60 alloy, the degree of recrystallization is significantly affected by the extrusion ratio. Therefore, ZK60 alloy exhibits a relatively finer and uniform microstructure at higher extrusion ratio.
5. The pre-extrusion homogenization treatment progressively dissolves the eutectic constituents and increases the formability of the Mg alloys. The eutectic constituents pin the grain boundaries and thus hinder their movements during recrystallization. Therefore, pre-extrusion homogenization treatment increases the degree of recrystallization. Similarly, the post-extrusion annealing treatment leads to meta-dynamic recrystallization and enhances the degree of recrystallization. Out of these two, the former is a better way of

increasing the degree of recrystallization, because it does not lead to the level of grain coarsening that is observed in the latter case.

6. The preferential slip along the shortest lattice direction $\langle 11\bar{2}0\rangle$ results in a basal texture after extrusion, where most of the grains have their prismatic $(1\bar{1}00)$ plane normal aligned parallel to the extrusion direction and thus the basal plane normal is at right angle. During recrystallization, some of the grains rotate by 30° about c-axis and align their $(1\bar{1}01)$ plane normal parallel to the extrusion direction, thereby weakening the $\langle 1\bar{1}00\rangle$ component of the texture.
7. A higher degree of deformation i.e. higher extrusion ratio, gives rise to a higher degrees of dynamic recrystallization and post-extrusion secondary recrystallization. Hence, the texture is weaker in the cases of higher extrusion ratio in both alloys. In comparison, the lowering of extrusion temperature within the studied range has little effect on the recrystallization behavior and therefore does not affect the texture intensities in both alloys.
8. Both pre-extrusion homogenization and post-extrusion annealing treatments enhance the degree of recrystallization and therefore weaken the crystallographic texture.
9. The basal texture after extrusion and the directional activation of the tensile twinning result in anisotropy in the yield stress. During longitudinal loading, the basal slip which requires the lowest critical resolved shear stress is inhibited because of a lower Schmidt factor. This gives a higher yield stress in longitudinal direction than in any other direction. The deformation mode that requires the second lowest critical resolved shear stress for activation $\{10\bar{1}2\}$ is favored when the c-axis of the lattice is under tension (as in longitudinal compression), Thus a CYS lower than the TYS is observed in the longitudinal direction.
10. Compared to the as-cast condition, the as-extruded alloys posses much finer grain size and consequently much higher YS, UTS and tensile elongation. The basal texture after extrusion gives higher YS in the longitudinal direction, whose value also depends on the sign of the applied stress, because of the strength differential effect (SDE). With the lowering of the extrusion temperature, grain size reduces and the impact of SDE weakens.
11. The tensile results show that in both AZ80 and ZK60 alloys, the variation of CYS in different directions caused by the texture is 25MPa. The difference between longitudinal TYS and longitudinal CYS at all extrusion ratios in AZ80 alloy and at the higher extrusion ratio (ER44) in ZK60 alloy is also ~ 25 MPa. Thus, a four times higher difference between longitudinal TYS and longitudinal CYS at lower extrusion ratio (ER12) in ZK60 can not be due to the texture and is likely due to the abundant coarse recrystallized grains, which consequently make the twinning activation easier.
12. The mechanical properties in the case of pre-extrusion homogenization treatment depend on whether a complete or a partial dissolution of the eutectic constituents take place. The yield stress is slightly lowered in the former case. While, it is not affected in the latter case. Similarly, the mechanical properties in the case of post-extrusion annealing depend on the annealing temperature. A too high temperature (400 °C for AZ alloy) leads to significant grain coarsening and thus lowers the yield stress.
13. The fine grain sizes achieved after extrusion in AZ80 and ZK60 alloys render the alloys to deform superplastically at elevated temperatures. The grain boundary sliding supported by dislocation slip lead to significant improvement in the tensile elongation before fracture at temperature $T \geq 250$ °C. The extrusion temperature affects the on set of dynamic recrystallization (DRX), exhibited by a peak in the flow curve, in both alloys. The

microstructure is more stable in the case of higher extrusion temperature and DRX starts at higher stress. A large number of coarse recrystallized grains and unrecrystallized regions in ZK60 alloy extruded at lower extrusion ratio (ER12) hinder the grain boundary sliding. Thus, a much lower tensile elongation is observed at lower extrusion ratio in ZK60. In comparison, extrusion ratio has no effect on the deformation behavior at elevated temperatures in AZ80 alloy due to similar degrees of recrystallization at both extrusion ratios.

14. The fatigue life of extruded alloys increases linearly with the increase in tensile yield stress. Therefore, lowering of extrusion temperature and pre-extrusion homogenization treatment increase the fatigue life of extruded alloys. Since, the crack propagation proceeds under tensile stress, the compressive yield stress does not affect the fatigue life of the alloys. Therefore, despite having a compressive yield stress lower by 75 MPa at lower extrusion ratio, ZK60 alloy exhibits same fatigue behavior at both extrusion ratios.

References

[1] K. Kubota, M. Mabuchi, and K. Higashi. Review processing and mechanical properties of fine-grained magnesium alloys. *Journal of Materials Science*, 34(10):2255–2262, 1999.

[2] EF. Emley. Principles of magnesium technology. 1966.

[3] R. Von Mises. Mechanik der Festen Korper im plastisch deformablen Zustand. *Nachr. Math. Phys.*, 1913.

[4] A. Galiyev, R. Kaibyshev, and G. Gottstein. Correlation of plastic deformation and dynamic recrystallization in magnesium alloy ZK60. *Acta materialia*, 49(7):1199–1207, 2001.

[5] X.S. Huang, K. Suzuki, A. Watazu, I. Shigematsu, and N. Saito. Effects of Homogenization Treatment on Mechanical Properties of Hot-Rolled AZ31 Magnesium Alloy. volume 561, page 255. Transtec Publications; 1999, 2007.

[6] MC Zhao, M. Liu, GL Song, and A. Atrens. Influence of homogenization annealing of AZ91 on mechanical properties and corrosion behavior. *Advanced Engineering Materials*, 10(1-2):93, 2008.

[7] MR Barnett, Z. Keshavarz, AG Beer, and D. Atwell. Influence of grain size on the compressive deformation of wrought Mg–3Al–1Zn. *Acta Materialia*, 52(17):5093–5103, 2004.

[8] EA Ball and PB Prangnell. Tensile-compressive yield asymmetries in high strength wrought magnesium alloys. *Scripta Metallurgica et Materialia*, 31(2):111–116, 1994.

[9] LWF Mackenzie, B. Davis, FJ Humphreys, and GW Lorimer. The deformation, recrystallisation and texture of three magnesium alloy extrusions. *Materials Science and Technology*, 23(10):1173–1180, 2007.

[10] M.R. Barnett. Quenched and annealed microstructures of hot worked magnesium AZ31. *Materials Transactions*, 44(4):571–577, 2003.

[11] MT Perez-Prado and OA Ruano. Texture evolution during annealing of magnesium AZ31 alloy. *Scripta materialia*, 46(2):149–155, 2002.

[12] X. Yang, H. Miura, and T. Sakai. Isochronal annealing behavior of magnesium alloy AZ 31 after hot deformation. *Materials transactions*, 46(12):2981–2987, 2005.

[13] S.H. Kim, B.S. You, C. Dong Yim, and Y.M. Seo. Texture and microstructure changes in asymmetrically hot rolled AZ31 magnesium alloy sheets. *Materials Letters*, 59(29-30):3876–3880, 2005.

[14] H.E. Friedrich and B.L. Mordike. Magnesium technology: metallurgy, design data, applications. 2006.

[15] M. Shahzad and L. Wagner. Thermo-Mechanical Methods for Improving Fatigue Performance of Wrought Magnesium Alloys. *Engineering Against Fracture: Proceedings of the 1st Conference*, page 249, 2009.

[16] J. Becker, B. Fischer, and K. Schemme. Light weight construction using extruded and forged semi-finished products made of magnesium alloys. *Magnesium Alloys and their Applications*, pages 15–28, 1998.

[17] A. Akhtar and E. Teghtsoonian. Substitutional solution hardening of magnesium single crystals. *Philosophical Magazine*, 25:897–916, 1972.

[18] EW Kelley and W. HOSFORD. The deformation characteristics of textured magnesium. *TRANS MET SOC AIME*, 242(4), 1968.

[19] J. Koike, T. Kobayashi, T. Mukai, H. Watanabe, M. Suzuki, K. Maruyama, and K. Higashi. The activity of non-basal slip systems and dynamic recovery at room temperature in fine-grained AZ31B magnesium alloys. *Acta materialia*, 51(7):2055–2065, 2003.

[20] J. Balik, M. Janecek, and P. Lukac. Dislocation glide and multiple slip. *Materials science & engineering. A, Structural materials: properties, microstructure and processing*, 159(2):143–149, 1992.

[21] C Escaravagge, P Bach, A. Champier, G, and E. Teghtsoonian. *in: Proc. 2nd Inter. Conference on the strength of Metals and Alloys, Pacific Grove*, page 299, 1979.

[22] C Escaravagge, P Bach, A. Champier, G, and E. Teghtsoonian. *in: Proc. 2nd Inter. Conference on the strength of Metals and Alloys, Pacific Grove*, page 272, 1970.

[23] A. Ahmadieh, J. Mitchell, and J.E. Dorn. *Trans. AIME*, 233:1130, 1965.

[24] A. Akhtar and E. Teghtsoonian. Solid solution strengthening of magnesium single crystals the effect of solute on the ease of prismatic slip. *Acta Metall.*, 17:1351–1356, 1969.

[25] H. Tonda and S. Ando. Effect of temperature and shear direction on yield stress by {1122} 1123 slip in HCP metalsslip in HCP metals. *Metallurgical and Materials Transactions A*, 33(13):831–836, 2002.

[26] M.H. Yoo, J.R. Morris, K.M. Ho, and S.R. Agnew. Nonbasal deformation modes of HCP metals and alloys: Role of dislocation source and mobility. *Metallurgical and Materials Transactions A*, 33(3):813–822, 2002.

[27] A. Serra, D.J. Bacon, and R.C. Pond. Twins as barriers to basal slip in hexagonal-close-packed metals. *Metallurgical and Materials Transactions A*, 33(3):809–812, 2002.

[28] P. Cizek and M.R. Barnett. The effect of double twinning on ductility of magnesium alloys. *ARC light metals workshop, Posters*, PS1–04, 2007.

[29] JW Christian and S. Mahajan. Deformation twinning. *Progress in Materials Science*, 39(1-2):1–157, 1995.

[30] YN Wang and JC Huang. The role of twinning and untwinning in yielding behavior in hot-extruded Mg–Al–Zn alloy. *Acta Materialia*, 55(3):897–905, 2007.

[31] MR Barnett. Twinning and the ductility of magnesium alloys Part II."Contraction" twins. *Materials Science & Engineering A*, 464(1-2):8–16, 2007.

[32] H. Li, E. Hsu, J. Szpunar, R. Verma, and J.T. Carter. Determination of Active Slip/Twinning Modes in AZ31 Mg Alloy Near Room Temperature. *Journal of Materials Engineering and Performance*, 16(3):321–326, 2007.

[33] RW Hertzberg. Deformation and fracture mechanics of engineering materials. 1983.

[34] S-B. Yi. Investigation on the deformation behavior and the texture evolution in magnesium wrougth alloy AZ31. *Ph.D Thesis at TU-Clausthal*, 2005.

[35] H.J Bünge. Texture analysis in materials science. *Cuvilier Verlag, Göttingen*, 1986.

[36] L.G Schulz. *Journal of Applied Physics*, 20:1030–1033, 1949.

[37] H.J Bunge and C. Esling. Experimental techniques. *Quantitative texture analysis*, 1986.

[38] S Matthies and G.W. Vinel. On the reproduction of the orientation distribution function of textured samples from reduced pole figures using the concept of conditional ghost correction. *Phys. Status. Solidi.*, B112, K111:388–392, 1982.

[39] UF Kocks, CN Tomé, and HR Wenk. Texture and anisotropy. *Cambridge University Press, POB 110, Cambridge, CB 2 3 RL, UK, 2000. 676*, 2000.

[40] MJ Philippe. Texture formation in hexagonal materials. *Materials Science Forum*, 157(162):1337–1350, 1994.

[41] C. Barrett and Massalskim T.B. Structure of metals, 3rd Ed. *Pergamon Press*, 1980.

[42] K.B. Müller and In: H.I. Kaplan (Ed.). Indirect extrusion of AZ31 and AZ61. *Magnesium Technology*, 2005.

[43] G. Wassermann and J. Grewen. Texturen Metallischer Werkstoff. *Springer Verlag - Berlin*, 1962.

[44] I.L. Dillamore and W.T. Roberts. Preferred orientation in wrought and annealed metals. *Metall. Review*, 10, 1965.

[45] E.W. Kelley and W.F. Hosford. The deformation characteristics of textured magnesium. *Trans. of the Metall. Soc. of AIME*, 242:654, 1968.

[46] F. Kaiser. Anisotropic properties of magnesium sheet AZ31. *Mater. Sci. Forum*, 419-422:315, 2003.

[47] T. Kaneko and M Suzuki. Automotive applications of magnesium alloys. *Mater. Sci. Forum*, 419-422:67, 2003.

[48] M.R. Barnett, M.D. Nave, and C.J. Beatles. Deformation microstructures and textures of some cold rolled Mg alloys. *Mater. Sci. Engg. A*, 386, 2004.

[49] M.T. Perez-Prado, J.A. del Valle, and O.A. Ruano. Effect of sheet thiickness on the microstructural evolution of an Mg AZ61 alloy during large strain hot rolling. *Script. Materialia*, 50, 2004.

[50] L Wagner, M. Hilpert, J. Wendt, and B Küster. On methods of improving the fatigue life of the wrought magnesium alloys AZ31 and AZ80. *Mater. Sci. Forum*, 419-422:93, 2003.

[51] S.R. Agnew and O. Duygulu. A mechanistic understanding of the formability of magnesium: examining the role of temperature on the deformation mechanism. *Mater. Sci. Forum*, 419-422:177, 2003.

[52] M.T. Perez-Prado, J.A. del Valle, J.M. Contreras, and O.A. Ruano. Microstructural evolution during large strain hot rolling of an AM60 Mg alloy. *Script. Materialia*, 50, 2004.

[53] I.L. Dillamore, P. Hadden, and D.J. Stratford. Texture control and the yield anisotropy of plane strain magnesium extrusions. *texture*, 1.

[54] S.R. Agnew, M.H. Yoo, and C.N. Tome. Application of texture simulation to understanding mechanical behavior of Mg and solid solution alloys containing Li or Y. *Acta Materialia*, 49, 2001.

[55] S.L. Courling, J.F. Pashak, and L. Sturkey. Unique deformation and aging characteristics of certain magnesium base alloys. *Trans. ASM*, 51, 1959.

[56] B.C. Wonsiewicz and W.A. Backofen. Plasticity of magnesium crystal. *Trans. of Metall. Soc. of AIME*, 239, 1966.

[57] S. Ertürk, D. Steglich, J. Bohlen, D. Letzig, and W. Brocks. Modelling and Simulation of Extrusion of Magnesium Alloys. *International Journal of Material Forming*, 1:419–422, 2008.

[58] M. Shahzad, D. Eliezer, W.M. Gan, S.B. Yi, and L. Wagner. Influence of Extrusion Temperature on Microstructure, Texture and Fatigue Performance of AZ80 and ZK60 Magnesium Alloys. *Materials Science Forum*, 561(1):187, 2007.

[59] M. Qian and A. Das. Grain refinement of magnesium alloys by zirconium: Formation of equiaxed grains. *Scripta materialia*, 54(5):881–886, 2006.

[60] D.H. StJohn, M. Qian, M.A. Easton, P. Cao, and Z. Hildebrand. Grain refinement of magnesium alloys. *Metallurgical and Materials Transactions A*, 36(7):1669–1679, 2005.

[61] W.F. Hosford. Mechanical behavior of materials. 2005.

[62] RJ Hellmig, TT Lamark, MV Popov, M. Janecek, Y. Estrin, and F. Chmelik. Influence of equal-channel angular pressing on the acoustic emission behaviour of magnesium alloy AZ31 under compression. *Materials Science & Engineering A*, 462(1-2):111–115, 2007.

[63] M. Janecek, M. Popov, MG Krieger, RJ Hellmig, and Y. Estrin. Mechanical properties and microstructure of a Mg alloy AZ31 prepared by equal-channel angular pressing. *Materials Science & Engineering A*, 462(1-2):116–120, 2007.

[64] M. Janecek, S-B. Yi, R. Kuzel, J Vratna, and KU. Kainer. Texture and Microstructure Evolution in ultrafine Grained AZ31 Processed By EX-ECAP. *TMS 2010*, 2010.

[65] J. Muller, M. Janecek, and L. Wagner. Influence of Post-ECAP TMT on Mechanical Properties of the Wrought Magnesium Alloy AZ80. *Materials Science Forum*, 584586:858–863, 2008.

[66] JA Del Valle, MT Pérez-Prado, and OA Ruano. Accumulative roll bonding of a Mg-based AZ61 alloy. *Materials Science & Engineering A*, 410:353–357, 2005.

[67] MT Perez-Prado, Valle, and OA Ruano. Grain refinement of Mg–Al–Zn alloys via accumulative roll bonding. *Scripta materialia*, 51(11):1093–1097, 2004.

[68] NV Ravi Kumar, J.J. Blandin, C. Desrayaud, F. Montheillet, and M. Su'ery. Grain refinement in AZ91 magnesium alloy during thermomechanical processing. *Materials Science & Engineering A*, 359(1-2):150–157, 2003.

[69] S. Spigarelli, M.E. Mehtedi, M. Cabibbo, E. Evangelista, J. Kaneko, A. Jäger, and V. Gartnerova. Analysis of high-temperature deformation and microstructure of an AZ31 magnesium alloy. *Materials Science & Engineering A*, 462(1-2):197–201, 2007.

[70] B. Hadzima, M. Janecek, P. Suchy, J. Muller, and L. Wagner. Microstructure and Corrosion Properties of Fine-Grained Mg-Based Alloys. *Materials Science Forum*, pages 584–586, 2008.

[71] C. Davies and M. Barnett. Expanding the extrusion limits of wrought magnesium alloys. *JOM Journal of the Minerals, Metals and Materials Society*, 56(5):22–24, 2004.

[72] B. Derby. The dependence of grain size on stress during dynamic recrystallisation. *ACTA METALL. MATER.*, 39(5):955–962, 1991.

[73] G.S. Cole. Issues that influence magnesium's use in the automotive industry. *Materials Science Forum*, 419(422):1, 2003.

[74] S. Schumann and H. Friedrich. Current and future use of magnesium in the automobile industry. *Materials Science Forum*, 419:51–56, 2003.

[75] P. Saha. Aluminum extrusion technology. 2000.

[76] ZP Luo, DY Song, and SQ Zhang. Strengthening effects of rare earths on wrought Mg–Zn–Zr–RE alloys. *Journal of alloys and compounds*, 230(2):109–114, 1995.

[77] Y. Chen, Q. Wang, J. Peng, C. Zhai, and W. Ding. Effects of extrusion ratio on the microstructure and mechanical properties of AZ31 Mg alloy. *Journal of Materials Processing Tech.*, 182(1-3):281–285, 2007.

[78] S. Ishihara, H Shibata, K. Komano, T. Goshima, and Z.Y. Nan. Effect of extrusion ratio on fatigue properties of hot-extruded magnesium alloys. *Key Engineering Materials*, 353-358(1):291–294, 2007.

[79] Y. Uematsu, K. Tokaji, M. Kamakura, K. Uchida, H. Shibata, and N. Bekku. Effect of extrusion conditions on grain refinement and fatigue behaviour in magnesium alloys. *Materials Science & Engineering A*, 434(1-2):131–140, 2006.

[80] J. Swiostek, J. Göken, D. Letzig, and K.U. Kainer. Hydrostatic extrusion of commercial magnesium alloys at 100° C and its influence on grain refinement and mechanical properties. *Materials Science & Engineering A*, 424(1-2):223–229, 2006.

[81] Image taken from Torrington-machinery website. `www.torrington-machinery.com/images/pic_rotary_swaging1.gif`. *Accessed on December 9, 2009.*

[82] IA Yakubtsov, BJ Diak, CA Sager, B. Bhattacharya, WD MacDonald, and M. Niewczas. Effects of heat treatment on microstructure and tensile deformation of Mg AZ80 alloy at room temperature. *Materials Science & Engineering A*, 496(1-2):247–255, 2008.

[83] M. Shahzad, M. Janecek, and L. Wagner. Effects of prior homogenization treatments on microstructure development and mechanical properties of the extruded wrought magnesium alloy ZK60. *International Journal of Materials Research*, 3:370–373, 2009.

[84] D.L. Atwell and M.R. Barnett. Extrusion Limits of Magnesium Alloys. *Metallurgical and Materials Transactions A*, 38(12):3032–3041, 2007.

[85] FJ Humphreys and M. Hatherly. Recrystallization and related annealing phenomena. *Elsevier Science Ltd, The Boulevard, Langford Lane, Kidlington, Oxford OX 5 1 GB, UK, 1995. 512*, 1995.

[86] F. Andreatta, I. Apachitei, AA Kodentsov, J. Dzwonczyk, and J. Duszczyk. Volta potential of second phase particles in extruded AZ80 magnesium alloy. *Electrochimica Acta*, 51(17):3551–3557, 2006.

[87] Y. Uematsu, K. Tokaji, and T. Ohashi. Corrosion fatigue behavior of extruded AZ80, AZ61, and AM60 magnesium alloys in distilled water. *Strength of Materials*, 40(1):130–133, 2008.

[88] R. Arroyave, A. van de Walle, and Z.K. Liu. First-principles calculations of the Zn–Zr system. *Acta Materialia*, 54(2):473–482, 2006.

[89] MM Myshlyaev, HJ McQueen, A. Mwembela, and E. Konopleva. Twinning, dynamic recovery and recrystallization in hot worked Mg–Al–Zn alloy. *Materials Science & Engineering A*, 337(1-2):121–133, 2002.

[90] CH Caceres and A. Blake. The strength of concentrated Mg-Zn solid solutions. *physica status solidi (a)*, 194(1), 2002.

[91] X. Zhao, K. Zhang, X. Li, Y. Li, Q. He, and J. Sun. Deformation behavior and dynamic recrystallization of Mg-Y-Nd-Gd-Zr alloy. *Journal of Rare Earths*, 26(6):846–850, 2008.

[92] F.A. Slooff, J. Zhou, J. Duszczyk, and L. Katgerman. Strain-dependent constitutive analysis of three wrought Mg–Al–Zn alloys. *Journal of Materials Science*, 43(22):7165–7170, 2008.

[93] TG Nieh, J. Wadsworth, and O.D. Sherby. Superplasticity in metals and ceramics. 1997.

[94] IJ Polmear. Light Alloys–Metallurgy of the Light Metals. *Edward Arnold, a division of Hodder and Stoughton, 41 Bedford Square, London WC 1 B 3 DQ, UK, 1989.*, 1989.

[95] Z Hildebrand, M Qian, DH St. John, and MT. Frost. Influence of zinc on the soluble zirconium content in magnesium and the subsequent grain refinement by zirconium. *Magnesium Technology 2004*, pages 241–245, 2004.

[96] H. Okamoto. Mg-Zr (Magnesium-Zirconium). *Journal of Phase Equilibria and Diffusion*, 23(2):198–199, 2002.

[97] M. M. Qian, D.H. St. John, and M.T. Frost. Mangesium Alloys and Their Applications. pages 706–712, 2003.

[98] M. Qian, DH StJohn, and MT Frost. Characteristic zirconium-rich coring structures in Mg–Zr alloys. *Scripta Materialia*, 46(9):649–654, 2002.

[99] M. Shahzad and L. Wagner. Microstructure development during extrusion in a wrought Mg–Zn–Zr alloy. *Scripta Materialia*, 60(7):536–538, 2009.

[100] HJ McQueen, MM Myshlyaev, and A. Mwembela. Microstructural Evolution and Strength In Hot Working Of Zk60 and Other Mg Alloys. *Canadian Metallurgical Quarterly*, 42(1):97–112, 2003.

[101] X. Gao and JF Nie. Structure and thermal stability of primary intermetallic particles in an Mg–Zn casting alloy. *Scripta materialia*, 57(7):655–658, 2007.

[102] Z Liu, X. Liu, H. Guo, B Liu, and P. Shen. Investigation on Microstructures and Properties of Mg-Zn-Y Alloys (H5.36). *International Materials Research Conference 2008, symposium H (Magneisum)*, Chongqing, China, 2008.

[103] M. Chandrasekaran and Y.M.S. John. Effect of materials and temperature on the forward extrusion of magnesium alloys. *Materials Science & Engineering A*, 381(1-2):308–319, 2004.

[104] CI Chang, CJ Lee, and JC Huang. Relationship between grain size and Zener–Holloman parameter during friction stir processing in AZ31 Mg alloys. *Scripta materialia*, 51(6):509–514, 2004.

[105] ZQ Sheng and R. Shivpuri. Modeling flow stress of magnesium alloys at elevated temperature. *Materials Science & Engineering A*, 419(1-2):202–208, 2006.

[106] T.C. Gray, G.T.: In Lowe, A.D. Rollett, P.S. Follansbee, and G.S. (Eds.) Daehn. Modelling the Deformation of Crystalline Solids. *TMS 1991*, pages 145–148, 1991.

[107] Y. Zhang, X. Zeng, C. Lu, and W. Ding. Deformation behavior and dynamic recrystallization of a Mg–Zn–Y–Zr alloy. *Materials Science & Engineering A*, 428(1-2):91–97, 2006.

[108] Q. Guo, HG Yan, ZH Chen, and H. Zhang. Grain refinement in as-cast AZ80 Mg alloy under large strain deformation. *Materials Characterization*, 58(2):162–167, 2007.

[109] Y. Zhang, X. Zeng, C. Lu, and W. Ding. Deformation behavior and dynamic recrystallization of a Mg–Zn–Y–Zr alloy. *Materials Science & Engineering A*, 428(1-2):91–97, 2006.

[110] M. Shahzad and L. Wagner. The role of Zr-rich cores in strength differential effect in an extruded Mg–Zn–Zr alloy. *Journal of Alloys and Compounds*, 486(1-2):103–108, 2009.

[111] G. Liu, J. Zhou, and J. Duszczyk. Finite Element Simulation of Magnesium Extrusion to Manufacture a Cross-Shaped Profile. *Journal of Manufacturing Science and Engineering*, 129:607, 2007.

[112] T. Murai, S. Matsuoka, S. Miyamoto, and Y. Oki. Effects of extrusion conditions on microstructure and mechanical properties of AZ31B magnesium alloy extrusions. *Journal of Materials Processing Tech.*, 141(2):207–212, 2003.

[113] SH Hsiang and YW Lin. Investigation of the influence of process parameters on hot extrusion of magnesium alloy tubes. *Journal of Materials Processing Tech.*, 192:292–299, 2007.

[114] M. Shahzad and L. Wagner. Influence of extrusion parameters on microstructure and texture developments, and their effects on mechanical properties of the magnesium alloy AZ80. *Materials Science & Engineering A*, 506(1-2):141–147, 2009.

[115] H. Ding, L. Liu, S. Kamado, W. Ding, and Y. Kojima. Study of the microstructure, texture and tensile properties of as-extruded AZ91 magnesium alloy. *Journal of Alloys and Compounds*, 456(1-2):400–406, 2008.

[116] F.M Elkin, V.G. Davydov, and In: K.U. Kainer (ed.). Russian Ultralight Constructional Mg-Li Alloys. Their Structure, Properties, Manufacturing, Applications. *Magnesium: proceedings of the 6th International Conference Magnesium Alloys and their Applications*, pages 94–98, 2004.

[117] SB Yi, H.G. Brokmeier, J. Bohlen, D. Letzig, and KU Kainer. Neutron diffraction study on the texture development during extrusion of magnesium alloy AZ31. *Physica B: Physics of Condensed Matter*, 350(1-3S):507–509, 2004.

[118] R. Cottam, J. Robson, G. Lorimer, and B. Davis. Dynamic recrystallization of Mg and Mg–Y alloys: Crystallographic texture development. *Materials Science & Engineering A*, 485(1-2):375–382, 2008.

[119] RD Doherty, DA Hughes, FJ Humphreys, JJ Jonas, DJ Jensen, ME Kassner, WE King, TR McNelley, HJ McQueen, and AD Rollett. Current issues in recrystallization: a review. *Materials science & engineering. A, Structural materials: properties, microstructure and processing*, 238(2):219–274, 1997.

[120] K. Luecke. *Proceedings of the 7th International Conference on Textures of Materials*, pages 195–210, 2000.

[121] EA Ball and PB Prangnell. Tensile-compressive yield asymmetries in high strength wrought magnesium alloys. *Scripta Metallurgica et Materialia*, 31(2):111–116, 1994.

[122] MT Perez-Prado and OA Ruano. Texture evolution during grain growth in annealed MG AZ61 alloy. *Scripta Materialia*, 48(1):59–64, 2003.

[123] MA Gharghouri, GC Weatherly, JD Embury, and J. Root. Study of the mechanical properties of Mg-7.7 at.% Al by in-situ neutron diffraction. *Philosophical Magazine A*, 79(7):1671–1695, 1999.

curriculum vitae

Muhammad Shahzad

Born	On December 11, 1978 at lahore, Pakistan.
Nationality	Pakistan
Contact	shahzad@live.de

Education

2000 – 2002	M.Sc. in Nuclear Engineering, PIEAS, Islamabad, Pakistan.
1996 – 2000	B.Sc. in Metallurgical & Materials Science, UET, Lahore, Pakistan.

Occupation

2002 – 2005	Research Assistant at PINSTECH, Islamabad, Pakistan.

Muhammad Shahzad,
Clausthal, May 2010